

REPORT DOCUMENTATION PAGE			Form Approved OMB NO. 0704-0188		
<p>The public reporting burden for this collection of information is estimated to average 1 hour per response, including the time for reviewing instructions, searching existing data sources, gathering and maintaining the data needed, and completing and reviewing the collection of information. Send comments regarding this burden estimate or any other aspect of this collection of information, including suggestions for reducing this burden, to Washington Headquarters Services, Directorate for Information Operations and Reports, 1215 Jefferson Davis Highway, Suite 1204, Arlington VA, 22202-4302. Respondents should be aware that notwithstanding any other provision of law, no person shall be subject to any penalty for failing to comply with a collection of information if it does not display a currently valid OMB control number.</p> <p>PLEASE DO NOT RETURN YOUR FORM TO THE ABOVE ADDRESS.</p>					
1. REPORT DATE (DD-MM-YYYY) 24-12-2013		2. REPORT TYPE Final Report		3. DATES COVERED (From - To) 1-Sep-2010 - 31-Aug-2013	
4. TITLE AND SUBTITLE Large-Eddy Simulation Analysis of Unsteady Separation Over a Pitching Airfoil at High Reynolds Number				5a. CONTRACT NUMBER W911NF-10-1-0348	
				5b. GRANT NUMBER	
				5c. PROGRAM ELEMENT NUMBER 611102	
6. AUTHORS Donghyun You, William Bromby, Adamandios Sifounakis				5d. PROJECT NUMBER	
				5e. TASK NUMBER	
				5f. WORK UNIT NUMBER	
7. PERFORMING ORGANIZATION NAMES AND ADDRESSES Carnegie Mellon University Office of Sponsored Programs 5000 Forbes Ave Pittsburgh, PA 15213 -3815				8. PERFORMING ORGANIZATION REPORT NUMBER	
9. SPONSORING/MONITORING AGENCY NAME(S) AND ADDRESS (ES) U.S. Army Research Office P.O. Box 12211 Research Triangle Park, NC 27709-2211				10. SPONSOR/MONITOR'S ACRONYM(S) ARO	
				11. SPONSOR/MONITOR'S REPORT NUMBER(S) 57386-EG.15	
12. DISTRIBUTION AVAILABILITY STATEMENT Approved for Public Release; Distribution Unlimited					
13. SUPPLEMENTARY NOTES The views, opinions and/or findings contained in this report are those of the author(s) and should not be construed as an official Department of the Army position, policy or decision, unless so designated by other documentation.					
14. ABSTRACT Unsteady flow separation during dynamic stall often leads to unacceptably large vibratory loads and acoustic noise, and limit forward flight speeds and maneuverability. To gain a quantitative understanding of the unsteady separation process, large-eddy simulation (LES) of turbulent flow over a pitching airfoil at realistic Reynolds and Mach numbers is performed. Numerical stability at high Reynolds number simulation is maintained using an unstructured-grid LES technology, which obeys higher-order conservation principles and employs a global-coefficient subgrid-scale turbulence model. A hybrid implicit-explicit time integration scheme is employed to					
15. SUBJECT TERMS Turbulent separation, large-eddy simulation					
16. SECURITY CLASSIFICATION OF:			17. LIMITATION OF ABSTRACT UU	18. NUMBER OF PAGES	19a. NAME OF RESPONSIBLE PERSON Donghyun You
a. REPORT UU	b. ABSTRACT UU	c. THIS PAGE UU			19b. TELEPHONE NUMBER 412-268-6808

Report Title

Large-Eddy Simulation Analysis of Unsteady Separation Over a Pitching Airfoil at High Reynolds Number

ABSTRACT

Unsteady flow separation during dynamic stall often leads to unacceptably large vibratory loads and acoustic noise, and limit forward flight speeds and maneuverability. To gain a quantitative understanding of the unsteady separation process, large-eddy simulation (LES) of turbulent flow over a pitching airfoil at realistic Reynolds and Mach numbers is performed. Numerical stability at high Reynolds number simulation is maintained using an unstructured-grid LES technology, which obeys higher-order conservation principles and employs a global-coefficient subgrid-scale turbulence model. A hybrid implicit-explicit time-integration scheme is employed to provide a highly efficient way to treat time-step size restriction in the separated flow region locally refined with dense mesh. The present simulations confirm the stability and effectiveness of the presented numerical schemes for dynamic stall simulations at realistic operating Reynolds and Mach numbers and show the characteristics of flow separation and reattachment processes which are qualitatively congruent with experimental observation.

To improve quantitative understanding of unsteady separation processes of turbulent boundary layers, direct numerical simulations are performed. The distinct characteristics of unsteady separating turbulent boundary layers are revealed by a systematic comparison with steady attached/separated turbulent boundary layers. For this purpose, four different flow configurations are simulated: (i) turbulent boundary layer flow with a zero-pressure gradient; (ii) turbulent boundary layer flow with an adverse-pressure gradient; (iii) steady separated turbulent boundary layer flow; and (iv) unsteady separating turbulent boundary layer flow. The present comparative study suggests physical phenomena during the unsteady separation process including unsteady boundary-layer detachment and reattachment, and production and dissipation of turbulent kinetic energy and vorticity.

Enter List of papers submitted or published that acknowledge ARO support from the start of the project to the date of this printing. List the papers, including journal references, in the following categories:

(a) Papers published in peer-reviewed journals (N/A for none)

Received

Paper

08/27/2012 12.00 Satbir Singh, Donghyun You, Sanjeeb T. Bose. Large-eddy simulation of turbulent channel flow using explicit filtering and dynamic mixed models, Physics of Fluids, (08 2012): 0. doi: 10.1063/1.4745007

12/24/2013 14.00 Satbir Singh, Donghyun You. A dynamic global-coefficient mixed subgrid-scale model for large-eddy simulation of turbulent flows, International Journal of Heat and Fluid Flow, (08 2013): 0. doi: 10.1016/j.ijheatfluidflow.2013.02.008

TOTAL: 2

Number of Papers published in peer-reviewed journals:

(b) Papers published in non-peer-reviewed journals (N/A for none)

Received

Paper

TOTAL:

Number of Papers published in non peer-reviewed journals:

(c) Presentations

Number of Presentations: 0.00

Non Peer-Reviewed Conference Proceeding publications (other than abstracts):

<u>Received</u>	<u>Paper</u>
-----------------	--------------

TOTAL:

Number of Non Peer-Reviewed Conference Proceeding publications (other than abstracts):

Peer-Reviewed Conference Proceeding publications (other than abstracts):

<u>Received</u>	<u>Paper</u>
-----------------	--------------

08/27/2012	1.00	Satbir Singh, Donghyun You, Sanjeeb T. Bose. Accuracy of subfilter-scale models for explicit-filter large-eddy simulation in turbulent channel flow, 7th International Symposium on Turbulence and Shear Flow Phenomena. 26-JUL-11, . : ,
08/27/2012	10.00	Donghyun You, William Bromby. Large-Eddy Simulation of Unsteady Separation Over a Pitching Airfoil at High Reynolds Number, Seventh International Conference on Computational Fluid Dynamics (ICCFD7). 08-JUL-12, . : ,

TOTAL: 2

Number of Peer-Reviewed Conference Proceeding publications (other than abstracts):

(d) Manuscripts

<u>Received</u>	<u>Paper</u>	
03/08/2012	6.00	Satbir Singh, Donghyun You. A dynamic global-coefficient mixed subgrid-scale model for large-eddy simulation of turbulent flows, Journal of Computational Physics (01 2012)
03/08/2012	7.00	Satbir Singh, Donghyun You. Large-eddy simulation of turbulent channel flow using explicit filtering and dynamic mixed models, Physics of Fluids (12 2011)
TOTAL:		2

Number of Manuscripts:

Books

<u>Received</u>	<u>Paper</u>
TOTAL:	

Patents Submitted

Patents Awarded

Awards

Graduate Students

<u>NAME</u>	<u>PERCENT SUPPORTED</u>	<u>Discipline</u>
Adamandios Sifounakis	1.00	
William Bromby	1.00	
FTE Equivalent:	2.00	
Total Number:	2	

Names of Post Doctorates

NAME

PERCENT SUPPORTED

FTE Equivalent:

Total Number:

Names of Faculty Supported

NAME

PERCENT SUPPORTED

National Academy Member

Donghyun You

0.20

FTE Equivalent:

0.20

Total Number:

1

Names of Under Graduate students supported

NAME

PERCENT SUPPORTED

FTE Equivalent:

Total Number:

Student Metrics

This section only applies to graduating undergraduates supported by this agreement in this reporting period

The number of undergraduates funded by this agreement who graduated during this period: 0.00

The number of undergraduates funded by this agreement who graduated during this period with a degree in science, mathematics, engineering, or technology fields:..... 0.00

The number of undergraduates funded by your agreement who graduated during this period and will continue to pursue a graduate or Ph.D. degree in science, mathematics, engineering, or technology fields:..... 0.00

Number of graduating undergraduates who achieved a 3.5 GPA to 4.0 (4.0 max scale):..... 0.00

Number of graduating undergraduates funded by a DoD funded Center of Excellence grant for Education, Research and Engineering:..... 0.00

The number of undergraduates funded by your agreement who graduated during this period and intend to work for the Department of Defense 0.00

The number of undergraduates funded by your agreement who graduated during this period and will receive scholarships or fellowships for further studies in science, mathematics, engineering or technology fields: 0.00

Names of Personnel receiving masters degrees

NAME

Adamandios Sifounakis

Total Number:

1

Names of personnel receiving PHDs

NAME

Total Number:

Names of other research staff

NAME

PERCENT SUPPORTED

FTE Equivalent:

Total Number:

Sub Contractors (DD882)

Inventions (DD882)

Scientific Progress

See Attachment

Technology Transfer

Large-Eddy Simulation Analysis of Unsteady Separation Over a Pitching Airfoil at High Reynolds Number

By

Donghyun You, William Bromby and Adamandios Sifounakis

Prepared with the support of the
Army Research Office
under Grant No. W911NF1010348

Report No. FPE-1

Computational Flow Physics and Engineering
Department of Mechanical Engineering
Carnegie Mellon University
Pittsburgh, Pennsylvania 15213

December 2013

Abstract

Unsteady flow separation during dynamic stall often leads to unacceptably large vibratory loads and acoustic noise, and limit forward flight speeds and maneuverability. To gain a quantitative understanding of the unsteady separation process, large-eddy simulation (LES) of turbulent flow over a pitching airfoil at realistic Reynolds and Mach numbers is performed. Numerical stability at high Reynolds number simulation is maintained using an unstructured-grid LES technology, which obeys higher-order conservation principles and employs a global-coefficient subgrid-scale turbulence model. A hybrid implicit-explicit time-integration scheme is employed to provide a highly efficient way to treat time-step size restriction in the separated flow region locally refined with dense mesh. The present simulations confirm the stability and effectiveness of the presented numerical schemes for dynamic stall simulations at realistic operating Reynolds and Mach numbers and show the characteristics of flow separation and reattachment processes which are qualitatively congruent with experimental observation.

To improve quantitative understanding of unsteady separation processes of turbulent boundary layers, direct numerical simulations are performed. The distinct characteristics of unsteady separating turbulent boundary layers are revealed by a systematic comparison with steady attached/separated turbulent boundary layers. For this purpose, four different flow configurations are simulated: (i) turbulent boundary layer flow with a zero-pressure gradient; (ii) turbulent boundary layer flow with an adverse-pressure gradient; (iii) steady separated turbulent boundary layer flow; and (iv) unsteady separating turbulent boundary layer flow. The present comparative study suggests physical phenomena during the unsteady separation process including unsteady boundary-layer detachment and reattachment, and production and dissipation of turbulent kinetic energy and vorticity.

Acknowledgements

The authors gratefully acknowledge the support of the Army Research Office under Grant No. W911NF1010348, with Dr. Frederick Ferguson as the program manager. Computing time was provided by the National Science Foundation TeraGrid under Grant No. ASC110028 through the Pittsburgh Supercomputing Center and by the U.S. Army Engineer Research and Development Center (ERDC).

Table of Contents

Abstract	iii
Acknowledgements	v
List of Tables	ix
List of Figures	x
Nomenclature	xv
1 Introduction	1
2 Literature survey	5
3 Computational methodology	9
3.1 Flow configuration	9
3.2 Numerical methods	10
4 Flow over a pitching airfoil	17
4.1 Effects of mesh resolution	17
4.2 Results and discussion	17
4.3 Summary	19
5 DNS of unsteady separation	27
5.1 Introduction	27
5.2 Computational methodology	29
5.2.1 Flow configuration	29
5.2.2 Numerical methods	31
5.3 Results and discussion	33
5.3.1 Steady boundary layers	33
5.3.2 Unsteady separating turbulent boundary layer	36
5.4 Summary	40

A	A fully conservative method on locally refined nested Cartesian grids .	57
A.1	Motivation and objectives	57
A.2	Computational method	59
A.2.1	Fractional step method	59
A.2.2	Conservation principles	60
A.2.3	Virtual-slanting nested Cartesian grid scheme	62
A.2.4	Virtual slanting limitation	66
A.2.5	Extension to three-dimensional configurations	67
A.3	Verification and validation	69
A.3.1	Unsteady convection-diffusion of a Gaussian pulse	69
A.3.2	2D Taylor-Green vortex	69
A.3.3	Flow in a lid-driven cavity	72
A.3.4	Flow over a square cylinder	77
A.3.5	3D Taylor-Green vortex	82
A.4	Summary	85
	References	86

List of Tables

A.1	Computational results for the Strouhal number (St), mean drag, and RMS lift at $Re = 100$ for the virtually-slanting scheme, as well as several results from the literature.	77
-----	------------------------------------------------------------------------------------------------------------------------------------------------------------------------------------------	----

List of Figures

3.1	Flow configuration for LES of flow over a pitching airfoil.	10
3.2	Contours of the instantaneous streamwise velocity around the leading-edge of an airfoil predicted by (a) LES based on a second-order centered finite-difference method on curvilinear coordinates and by (b) LES based on a second-order centered finite-volume method on Cartesian coordinates (the present scheme).	14
3.3	Schematic illustration of (a) a grid resolution topology and (b) separation of implicit and explicit time-integration zones.	15
4.1	Computational grid topology for LES of flow over a pitching airfoil.	20
4.2	Pressure distribution on the airfoil surface at the angle of attack 14 degrees. Solid line, the present LES solution on a 24 million-cell mesh; symbol, experimental data.	21
4.3	Contours of the spanwise vorticity predicted by the present LES over a half period of pitching motion at Mach number of 0.2.	22
4.4	Contours of the spanwise vorticity predicted by the present LES over a period of pitching motion at Mach number of 0.3.	23
4.5	Lift coefficient and pressure drag coefficient as a function of pitch angle at Mach number of 0.2.	24
4.6	Pitching moment coefficient and pressure coefficient at $x/c = 0.005$ as a function of pitch angle at Mach number of 0.2.	25
5.1	Schematic illustration of computational modeling of unsteady separating turbulent boundary layers.	30
5.2	Computational domain sizes in terms of the inlet-displacement thickness and corresponding number of grid points.	31
5.3	Vertical velocity profiles imposed on the top boundary of the computational domain. Velocity magnitudes are normalized with the freestream velocity.	32
5.4	DNS results in the ZPG case. Na & Moin's results shown with dotted lines.	34
5.5	Mean streamwise velocity profiles in the APG case at three streamwise locations in wall units.	35

5.6	RMS velocity fluctuations in the APG case in three streamwise locations. . .	41
5.7	Mean streamwise velocity profiles in the SBL case in streamwise locations in wall units.	42
5.8	RMS velocity fluctuations normalized with the freestream velocity in the SBL case.	44
5.9	Contours of the instantaneous skin-friction coefficient. Negative values are dashed.	45
5.10	Amplification factor used to convert $V_{top}(x)$ to $V_{top}(x, t)$. x-axis indicates the phase number.	45
5.11	Spanwise-averaged fraction of time ($\bar{\gamma}_u$) that flow moves downstream. . . .	46
5.12	Streamwise distributions of phase averaged skin-friction and pressure coefficients.	47
5.13	Streamwise distributions of total averaged skin-friction and pressure coefficients.	48
5.14	Streamwise velocity profiles in wall units. — USBL; — SBL.	49
5.15	Turbulence intensity profiles normalized with U_∞^2 . — USBL; — SBL. . . .	50
5.16	Comparisons of the turbulent kinetic energy and turbulent kinetic energy production and dissipation normalized with $\frac{U_\infty^3}{100\delta_{in}^*}$. — USBL; — SBL. . .	51
5.17	Contours of $\bar{u}/U_\infty = 0.4$; — SBL; — Phase 1; -- Phase 6.	52
5.18	Contours of $\bar{u}/U_\infty = 0.4$ and $\bar{u}/U_\infty = 0.0$; — Phase 1; -- Phase 6.	52
5.19	Mean streamwise velocity normalized with δ_{in}^*	53
5.20	Instantaneous vortex fields defined by $\lambda_2 = -0.1$, and corresponding wall shear stress distributions.	54
5.21	Instantaneous vorticity contours at $x/\delta_{in}^* = 260$ ((a) and (b)), and $x/\delta_{in}^* = 320$ ((c) and (d)).	55
5.22	Instantaneous vorticity distributions.	56
A.1	Three example grids: (a) a regular Cartesian grid, (b) a non-slanted nested Cartesian grid, and (c) a virtually-slanted nested Cartesian grid. It can be seen that virtually-slanting mesh (b) aligns the face-normal velocities, u_n , with the vectors connecting the coarse and fine cell-centers, thus reducing the inherent skewness in the hanging-node mesh.	63
A.2	Virtual-slanting in the case where $\Delta y/\Delta x = \sqrt{3}$	66

A.3	Isometric views of the fine cells at a refinement interface are shown above for the (a) fully-slanted and (b) approximated slanting configurations. A side view of each method is also shown in (c) and (d), respectfully, for clarity. The alternating shaded regions in (a) and (c) are used to show the new faces generated between edge cells when the fully-slanted approach is employed. These new faces expose the coarse cell to diagonal cells, requiring additional connectivity information and increasing the computational cost of the simulation. (c) and (d) clearly illustrate that no new faces are introduced in the approximated slanting approach.	68
A.4	Diagrams of (a) the computational mesh layout employing two levels of refinement and (b) the contours of the convected Gaussian pulse from left to right (at $t = 0$ and $t = 1.0$, respectively) for $Re = 2$. The thick black line along the centerline of (b) denotes the refinement interface.	70
A.5	The above plot shows the L_2 -norm errors as a function of grid spacing for (a) $Re = 2$ and (b) $Re = 200$. Both plots show that the virtually-slanting scheme is globally second-order accurate.	71
A.6	Diagrams of (a) the computation mesh layout used to simulate two-dimensional Taylor-Green vortices and (b) the pressure contours of the initial field. The thick black lines in (b) illustrate the refinement interfaces.	73
A.7	The above plots show that the virtually-slanted scheme is globally second-order accurate for both (a) velocity and (b) pressure at $Re = 100$	74
A.8	The kinetic energy time-history shows that the virtually-slanting scheme conserves energy better than the standard non-slanted hanging node scheme.	75
A.9	The above plots illustrate the (a) computational grid employed and (b) the u -velocity contours for the steady-state solution at $Re = 1000$	76
A.10	Good agreement can be seen between the virtually-slanting scheme and the uniform mesh results for the centerline velocities of both (a) u and (b) v . The uniform mesh resolution was set according to the finest resolution in the locally refined case, $\Delta x = \Delta x_f = 6.25 \times 10^{-3}$	78
A.11	The overall computational configuration is shown above in (a), with a closer look at the refinement interfaces around the square-cylinder shown in (b). Five distinct levels of refinement are shown, with the highest resolution of $\Delta x_f = 7.8125 \times 10^{-3}$ located at the cylinder wall.	79

A.12	Contours for the instantaneous z -vorticity are shown in (a), with a closer look at the contours around the square-cylinder presented in (b).	80
A.13	The above plot shows the smooth variation in the coefficient of lift (C_L) as a function of time.	81
A.14	The above diagrams depict (a) the computation mesh used to simulate three-dimensional Taylor-Green vortices and (b) contours of the initial pressure field.	83
A.15	The above plot shows the time-history of the kinetic energy for three-dimensional Taylor-Green vortices. The virtually-slanted (- - - red line) scheme shows good agreement with the uniform results (— black line), while the kinetic energy cascade begins much sooner for the interpolated scheme (- · - blue line).	84

Nomenclature

Roman Symbols

C	Chord length
C_D	Drag coefficient
C_L	Lift coefficient
C_p	Pressure coefficient
f	Generic function; frequency
f_i	x_i component of body force
F	Flux vector
G	Flux vector
J	Jacobian of the coordinate transformation
k	Turbulent kinetic energy; wavenumber
L	Length scale; domain size
n	Time-step index; number of processors
N	Number of mesh points
p	Pressure
Re	Reynolds number
Re _C	Chord-based Reynolds number
St	Strouhal number
S_{ij}	Strain rate tensor
t	Time
\mathbf{u}	u_1, u_2, u_3

u	Streamwise velocity
u_i	x_i component of velocity
u_τ	Wall-shear velocity, $(\tau_w/\rho)^{1/2}$
U_{ref}	Reference velocity
U_∞	Free-stream velocity
v	Wall-normal velocity
w	Cross-stream velocity
x	Streamwise coordinate
x_i	Cartesian coordinates
y	Wall-normal coordinate
z	Cross-stream coordinate

Greek Symbols

α	Angle of attack
δ	Dirac delta function; boundary layer thickness
δ_{ij}	Kronecker delta
Δ	Filter width; grid spacing
Δt	Time step
$\Delta x, \Delta y, \Delta z$	Grid spacing in x , y , and z directions respectively
ϵ	Turbulent kinetic energy dissipation
θ	Angle; momentum thickness
λ	Generic eigenvalue
λ_2	Eigenvalue representing vortex

μ	Molecular viscosity, $\mu = \rho\nu$
μ_t	Turbulent viscosity, $\mu_t = \rho\nu_t$
ν	Kinematic viscosity
ν_t	Eddy viscosity
π	3.14159...
ρ	Density
τ_{ij}	Subgrid-scale stress tensor
τ_w	Wall-shear stress
ϕ	Generic scalar variable
ω	Angular frequency; vorticity
$\omega_x, \omega_y, \omega_z$	Vorticity components in x , y , and z directions respectively

Other Symbols

$\hat{()}$	Test-filtered quantity; intermediate step in fractional-step method
$\overline{()}$	Filtered quantity
$()'$	Fluctuation component
$()^+$	Quantity in wall-unit
$\mathcal{O}()$	Order of magnitude
∇	Gradient operator

Abbreviations

ARL	Army Research Laboratory
ASC	Aeronautical Systems Center

CFD	Computational Fluid Dynamics; Common Flow Down
CFL	Courant-Friedrichs-Lewy
CFU	Common Flow Up
DNS	Direct Numerical Simulation
DoD	Department of Defense
FFT	Fast Fourier Transform
GB	Gigabyte
HPCMP	High Performance Computing Modernization Program
LES	Large Eddy Simulation
MPI	Message Passing Interface
MSRC	Major Shared Resource Center
NUMA	Nonuniform Memory Access
RANS	Reynolds-Averaged Navier-Stokes
<i>rms</i>	Root Mean Square
SGS	Subgrid Scale

Chapter 1

Introduction

Dynamic stall is a nonlinear and unsteady aerodynamic phenomenon resulting in stall delay during a time-dependent motion of an airfoil at angles of attack higher than its static stall angle. Dynamic stall of high Army relevance occurs on the retreating blade of a helicopter rotor experiencing a pitching motion which leads to unsteady flow separation followed by load and pitching-moment overshoots. The unsteady flow separation can in turn lead to unacceptably large vibratory loads and acoustic noise, and limit forward flight speeds, load, and maneuverability (Lorber & Carta 1994). The unsteady separation is reported to be influenced by the Reynolds and Mach numbers, blade geometry, pitch rate, and freestream turbulence level (McCroskey 1982).

Numerous investigations of unsteady separation associated with dynamic stall have been conducted at chord-based Reynolds numbers (Re_C) in the range of $10^3 - 10^7$, at Mach numbers for incompressible to transonic flow, and for a wide variety of blade geometries. Most experimental studies have concentrated on measurements of aerodynamic forces such as the surface pressure and overall loads (*e.g.*, Lorber & Carta (1987); Jumper *et al.* (1987)), or on the flow field visualization (*e.g.*, McCroskey *et al.* (1976)). Quantitative measurements of the separated flow field and wake around a pitching airfoil have been difficult using experimental techniques, and therefore, have rarely been reported in the literature.

Computational fluid dynamics has become increasingly useful in studying dynamic stall (see Ekaterinaris & Platzer (1997) for a review). Computational works have often been performed, especially at practical Reynolds numbers, using the Reynolds-averaged Navier-Stokes (RANS) equations or its unsteady counterpart (URANS) (*e.g.*, Visbal (1988); Spentzos *et al.* (2005)). However, it is known to be very challenging for (U)RANS to accurately predict highly unsteady flow involving incipient flow separation, formation and evolution of stall vortices, and reattachment. So far, none of the available turbulence models has shown a satisfactory predictive performance for all of these flow phenomena. In a review article, Carr & McCroskey (1992) concluded that “Turbulence modeling becomes of crucial importance when dynamic stall is considered. This is particularly true when the question of incipient separation and dynamic-stall-vortex development is to be represented by a single

turbulence model; under this condition, the use of a turbulence model based on equilibrium attached boundary layers in steady flow (*e.g.*, eddy viscosity, Baldwin-Lomax) is open to question. The task of predicting separation by definition deals with boundary layers that have experienced very strong pressure gradients, often both positive and negative; the flow approaching unsteady separation contains high levels of vorticity induced by these pressure gradients, and is strongly unsteady. Recent study has shown that modification of the turbulence model can completely change the resulting flow results; at the same time, very little has been experimentally documented about the character of turbulence under these conditions.”

The detached-eddy simulation (DES) and kinetic-energy simulation (KES, Fang & Menon 2006) have also been explored in dynamic stall applications. Although encouraging results were obtained using DES over a wide range of flow configurations, flow separation is often difficult to predict due to the existence of the gray zone in which the model is improperly converted from attached boundary layer to massive separation (Spalart *et al.* 1997). KES, which was designed to predict flow at length scales between the computational grid scale and the integral scale, is in the evaluation stage as discussed by its developers (Fang & Menon 2006).

The intrinsic capability of large-eddy simulation (LES) for predicting sufficient details of unsteady separating flows has recently been explored by a certain number of researchers. Nagarajan *et al.* (2006) and Ghias *et al.* (2005) performed LES of dynamic stall over a pitching airfoil and tip-flow of a rotor in hover using structured-grid finite-difference methods on curvilinear coordinates. The Reynolds numbers considered in these simulations were around 10^5 , which are substantially below that of a typical helicopter rotor during low-speed maneuvers ($O(10^6)$). LES at higher Reynolds numbers has been difficult mainly due to the numerical instability issue and high computational costs associated with the spatial and temporal resolution requirements. Simulations and experiments performed at $Re_C < 5 \times 10^5$ indicate that stall frequently occurs when laminar flow separates near the leading edge. This process leads to large steady-state stall hysteresis. However, turbulent separation is more common at high Reynolds number and this makes the unsteady stall characteristics quite dissimilar from the features observed at low Reynolds number.

Most CFD works so far have focused on the validation of CFD codes and *qualitative* features of dynamic stall rather than the understanding of the flow physics under realistic flight conditions. Detailed quantitative characterization of velocity and pressure are needed

in the separating flow region for the fundamental understanding of the unsteady separation process. In this work, we perform wall-resolved LES of unsteady separation over a pitching airfoil at realistic Mach and Reynolds numbers. The research focus is on a quantitative understanding of the unsteady separation process rather than validation and qualitative characterization of the flow field. For this purpose, we will employ an unstructured-grid LES technology, which maintains numerical stability by obeying higher-order conservation principles – *i.e.*, kinetic-energy conservation in the inviscid limit in addition to mass and momentum conservation. The unstructured grid topology as well as a hybrid implicit/explicit time-integration method provides highly enhanced efficiency in treating spatial and temporal resolution requirements in the dynamically important separated flow region.

The specific objectives of the proposed work are (i) to develop and provide guidelines for an accurate LES of dynamic stall at *realistic* Reynolds and Mach numbers ($Re_C = 2 - 4 \times 10^6$, $Ma = 0.2 - 0.4$); (ii) to gain a deeper understanding of *quantitative* aspects of unsteady separation during dynamic stall, such as turbulent kinetic energy and vorticity budgets, velocity and pressure fluctuations, and spatiotemporal correlations of primitive variables; (iii) to quantify the effects of the important parameters on dynamic stall such as compressibility, type of pitching motion, and pitch rate; (iv) to provide insights for advancing turbulence models by analyzing the simulation databases; and (v) to develop strategies for unsteady separation control.

CHAPTER 1. INTRODUCTION

Chapter 2

Literature survey

Flow-field visualization has been a dominant method to characterize or categorize the dynamic stall phenomenon. For example, using an oil-smoke visualization technique, McCroskey *et al.* (1976) described three different types of boundary-layer separation: (i) trailing-edge stall; (ii) leading-edge stall following a progression of flow reversal from the trailing edge; and (iii) leading-edge stall due to abrupt bursting of a leading-edge separation bubble. Carr *et al.* (1991) employed a real-time point-diffraction interferometry technique to obtain interferograms which visualize the effect of unsteadiness on the leading-edge flow over a pitching airfoil.

Lorber & Carta (1987) was probably the first to provide an experimental database of constant-pitch-rate aerodynamic information, such as the surface pressure and overall loads, *at realistic combinations of Reynolds and Mach numbers*. They considered an airfoil oscillating at pitch rates, between 0.001 and 0.020, Mach numbers between 0.2 and 0.4, and Reynolds numbers between $2 - 4 \times 10^6$. The results demonstrated the influence of the leading-edge vorticity on the unsteady aerodynamic response during and after stall. The leading-edge vortex was found to be strengthened by increasing the pitch rate while the vortex strength was found to be weakened by increasing the Mach number and by starting the motion close to the steady-state stall angle. In the experiment, they observed a periodic pressure oscillation after stall at a high pitch angle and moderate Reynolds number. A small supersonic zone near the leading edge at $Ma = 0.4$ was found to reduce significantly the peak suction pressures and the unsteady increments to the airloads. Most recently, Sahoo *et al.* (2009) conducted particle image velocimetry (PIV) measurements of the velocity and pressure during the initiation of dynamic stall processes for a pitching airfoil at realistic helicopter flight conditions. Unlike other previous experimental work, this research aimed at gaining a *quantitative* understanding of the vorticity and turbulent flow characteristics in the separated flow region.

Among physical processes during dynamic stall, the onset of flow separation has been studied relatively extensively. Smith (1988) examined several important issues including the instability of a leading-edge separation bubble and finite-time breakup of a boundary layer.

Later, Currier & Fung (1992) performed a detailed analysis of experimental data provided by McCroskey *et al.* (1982) and Lorber & Carta (1987) to characterize the onset of stall for airfoils undergoing oscillatory and ramp-type motions about static stall angles. They found that, although the dependence of stall onset on the Mach number is the same for different airfoils, the dependence on the frequency can be very different for different airfoils, or for airfoils with differently shaped leading edges. Currier & Fung’s analysis showed that dynamic stall cases considered by McCroskey *et al.* (1982) and Lorber & Carta (1987) belong to the range of Reynolds number for which stall onset is ascribed to bursting of a separation bubble, arising from failure of the separated boundary layer to reattach. It was also suggested that completion of the separation process requires a finite time comparable to other flow time scales and that, although increased unsteadiness delays the occurrence of the onset to a higher angle, it actually promotes the process of boundary-layer separation.

Much research has also been conducted to identify the effects of key parameters such as the Mach number, Reynolds number, and pitch rate on the dynamic stall phenomenon. In wind-tunnel experiments, Jumper *et al.* (1987) reported that the magnitude of the maximum lift coefficient of a pitching airfoil is highly dependent on the pitch rate. McCroskey *et al.* (1976) investigated the influence of various airfoil profiles and leading edge geometries. The effects of Mach number on the dynamic stall of an oscillating airfoil have been discussed by Chandrashekhara & Carr (1989).

Although these and other previous studies have provided insights into *qualitative* aspects of the breakdown of a boundary layer and onset of dynamic stall, and some effects of key operation parameters, *quantitative* aspects of unsteady separation during dynamic stall, such as turbulent kinetic energy and vorticity budgets, velocity and pressure fluctuations, and spatiotemporal correlations of primitive variables, are yet not well understood. Such an understanding is crucial especially for advancing theoretical and computational methods and models for predicting dynamic stall and for developing new concepts for stall control.

Although computational fluid dynamics has received increasing attention as a means to develop an understanding of detailed spatiotemporal characteristics of dynamic stall events, most computational studies so far have focused on the validation of numerical methods and *qualitative* features of dynamic stall. Visbal (1988) performed RANS simulations of dynamic stall of an airfoil which was pitched at a constant rate from zero incidence to a high angle of attack. The computed dynamic stall events, as well as the complicated effects of pitch rate and axis location were found in qualitative agreement with experimental

observations. He also investigated compressibility effects on dynamic stall and found that the shock/boundary-layer interaction at high Mach numbers significantly alters the dynamic stall process (Visbal 1990). Later, Visbal (1991) presented a computational assessment of various techniques for dynamic stall control using RANS. Choudhuri *et al.* (1994) conducted a low Reynolds number ($Re_C = 10^4$) simulation of initial stages of two-dimensional unsteady leading-edge boundary-layer separation of laminar subsonic flow over a pitching NACA-0012 airfoil using the compressible laminar Navier-Stokes equations.

Large-eddy simulation (LES) has emerged as a tool for studying detailed physics of unsteady separating flows. Ghias *et al.* (2004, 2005) performed LES of dynamic stall over a pitching airfoil and tip-flow of a rotor in hover using structured-grid finite-difference methods on curvilinear coordinates at relatively low Reynolds numbers ($Re_C = 10^4$ and 4.5×10^4). They could successfully compare their computational results with the experimental data of Walker *et al.* (1985). They could also utilize the LES database to develop control strategies for dynamic stall. Nagarajan *et al.* (2006) demonstrated advantages of LES for dynamic stall applications by conducting comparative RANS and LES of dynamic stall over a pitching NACA 0012 airfoil at a transitional Reynolds number ($Re_C = 1.3 \times 10^5$). They also suggested that the predictive capability of RANS not only for the flow-field but also for the radiated noise can be significantly improved with refined turbulence models whose construction can be deduced from an analysis of an LES database.

The Reynolds numbers considered in the previous LES were substantially below that of a typical helicopter rotor during low-speed maneuvers ($O(10^6)$). This was mainly because LES at higher Reynolds numbers has been difficult mainly due to the numerical instability issue and high computational costs associated with the spatial and temporal resolution requirements. While the issue of high computational costs may be relieved by alternative LES-related methods such as hybrid LES-RANS methods, detached-eddy simulation (DES), and kinetic-eddy simulation (KES) (Fang & Menon 2006), numerical instability remains a major obstacle for an accurate simulation of dynamic stall at high Reynolds number.

CHAPTER 2. LITERATURE SURVEY

Chapter 3

Computational methodology

3.1 Flow configuration

The flow configuration is shown in figure 3.1 and corresponds to the experimental setup of Lorber & Carta (1987), which was developed to study dynamic stall penetration at constant pitch rate and realistic combinations of Reynolds and Mach numbers. The flow configuration models conditions occurring during aircraft post-stall maneuvers and during helicopter high speed forward flight. A Sikorsky SSC-A09 airfoil with a chord length of 43.9 cm was installed in the UTRC Wind Tunnel. The surface pressure was measured using miniature transducers, and the locations of transition and separation were determined using surface hot film gages.

There are four basic parameters that characterize the experimental conditions: Mach number, Reynolds number, pitch rate, and pitch range. While the majority of the data was taken at Mach number of 0.2, some data at Mach numbers of 0.3 and 0.4 were also recorded. These Mach numbers cover the range expected both for aircraft maneuvers at high angle of attack and helicopter blades on the retreating side of the rotor at high advance ratio. The corresponding Reynolds numbers based on the airfoil chord were 2, 3, and 4×10^6 , respectively. The pitch angle was controlled by hydraulic actuators attached to each end of the airfoil. Unsteady oscillating configurations with 9 different sinusoidal and 36 different constant pitch rate ramping motions were considered at angles of attack in a range between -5° and 30° . Both positive and negative pitch rate ramps were studied at nondimensional pitch rates, $A = \dot{\alpha}c/2U_\infty = 0.001 - 0.02$, where $\dot{\alpha}$, c , and U_∞ are the pitch rate, chord, and freestream velocity, respectively. For the sinusoidal oscillations, data were taken at reduced frequencies, $k = \omega c/2U_\infty = 0.025, 0.050$, and 0.100 , where ω is the angular frequency.

Pressure time histories, aerodynamic forces and moment, surface pressure distributions, and transition and separation locations are available as a function of pitch rate, type of pitching motion (ramp and sinusoidal), Mach number, and Reynolds number.

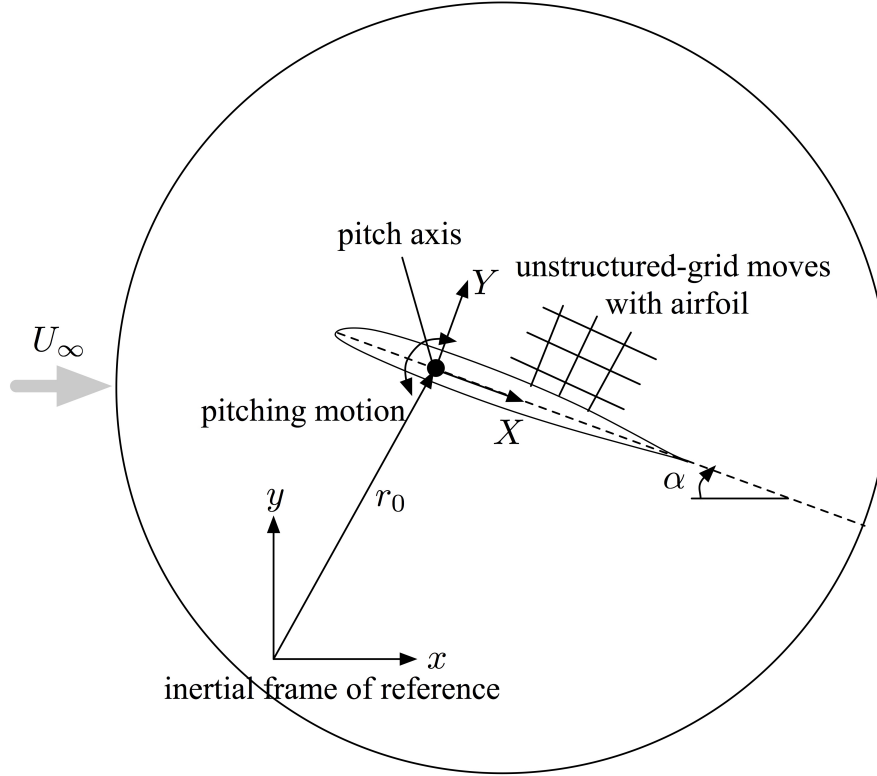


FIGURE 3.1. Flow configuration for LES of flow over a pitching airfoil.

3.2 Numerical methods

We employ an unstructured-grid LES solver which was developed at the Center for Turbulence Research (You *et al.* 2008a; Shoeybi *et al.* 2007) and has recently been further developed by the PI to include a new subgrid-scale LES model (You & Moin 2007). The numerical method is based on unstructured-grid finite-volume discretization of the Favre-filtered compressible Navier-Stokes equations with subgrid-scale stress and heat flux models. The present numerical method overcomes two major difficulties encountered in the previous rotor applications using structured-curvilinear-grid LES approaches such as employed by the teams at the Center for Turbulence Research (Nagarajan *et al.* 2006) and at George Washington University (Ghias *et al.* 2005).

Firstly, it is known that non- or low-dissipative finite-difference schemes on curvilinear coordinates do not strictly conserve kinetic energy (Nagarajan *et al.* 2004), and therefore, are

more prone to be numerically unstable (see figure 3.2(a)). Due to the numerical instability, the Reynolds numbers in the previous LES (Nagarajan *et al.* 2006; Ghias *et al.* 2005) were lower by an order of magnitude ($O(10^5)$) than the practical Reynolds number in rotor applications ($> O(10^6)$). The present Cartesian-coordinate-based finite-volume method maintains the numerical stability as well as the numerical accuracy at high Reynolds number by employing an unstructured-grid spatial-discretization algorithm that minimizes the non-conservation of kinetic energy (figure 3.2(b)).

The Favre-filtered compressible Navier-Stokes equations can be written as

$$\frac{\partial U}{\partial t} + \frac{\partial F_j}{\partial x_j} = \frac{\partial G_j}{\partial x_j}, \quad (3.1)$$

where

$$U = \begin{pmatrix} \bar{\rho} \\ \bar{\rho} \tilde{u}_1 \\ \bar{\rho} \tilde{u}_2 \\ \bar{\rho} \tilde{u}_3 \\ \bar{E} \end{pmatrix}, \quad F_j = \begin{pmatrix} \bar{\rho} \tilde{u}_j \\ \bar{\rho} \tilde{u}_1 \tilde{u}_j + \bar{p} \delta_{1j} \\ \bar{\rho} \tilde{u}_2 \tilde{u}_j + \bar{p} \delta_{2j} \\ \bar{\rho} \tilde{u}_3 \tilde{u}_j + \bar{p} \delta_{3j} \\ (\bar{E} + \bar{p}) \tilde{u}_j + \bar{q}_j \end{pmatrix}, \quad G_j = \begin{pmatrix} 0 \\ \bar{\sigma}_{1j} - \tau_{1j}^{sgs} \\ \bar{\sigma}_{2j} - \tau_{2j}^{sgs} \\ \bar{\sigma}_{3j} - \tau_{3j}^{sgs} \\ \tilde{u}_k \bar{\sigma}_{jk} - q_j^{sgs} \end{pmatrix}.$$

U is the vector of the Favre-filtered conserved variables and F_j and G_j are the flux vectors in the j -direction. ρ , p , u_i , and E denote density, pressure, velocity component, and energy, respectively. $\bar{\sigma}_{ij}$ and \bar{q}_j are the filtered stress tensor and heat flux, respectively. τ_{ij}^{sgs} and q_j^{sgs} are the subgrid-scale stress tensor and heat flux, respectively.

Finite-volume discretization of the governing equation (3.1) leads to

$$\frac{\partial U_k}{\partial t} + \frac{1}{V_{\Omega_k}} \sum_f \sum_{j=1}^3 (F_j^f - G_j^f) n_j^f = 0, \quad (3.2)$$

where V_{Ω_k} is the volume measure of a volume-element Ω_k , and U_k is the state variable vector at grid point k . F_j^f and G_j^f are the flux vectors at the element-boundary faces $\partial\Omega_k^f$. n_j^f denotes the face-normal unit vector.

In the present study, the convective and diffusive fluxes are obtained using the *Summation-By-Parts* operators (*e.g.*, skew-symmetric averaging for the convective flux; see also Strand (1994)) which guarantee non-growing positive norms of primary variables, thereby maintaining numerical stability. The present method is proven to be particularly well suited for

predicting subtle separation effects in turbulent boundary layers at high Reynolds number where boundary layer energetics play a crucial role (You *et al.* 2008a).

In addition, the proposed LES will employ the dynamic *global-coefficient* subgrid-scale (SGS) model which has recently been developed by the PI (You & Moin 2007). In the dynamic Smagorinsky model (Germano *et al.* 1991; Moin *et al.* 1991), which has widely been used in LES, the model coefficient is dynamically determined as a function of space and time using the scale-invariance concept and the *local-equilibrium* hypothesis (*i.e.*, an equilibrium between the subgrid-scale dissipation and the viscous dissipation at the same physical location). Although the dynamic model coefficient vanishes where the flow is laminar or fully resolved, it can cause numerical instability since its value often becomes negative and/or highly fluctuates in space and time.

To overcome the deficiency of the dynamic Smagorinsky model, the PI developed a dynamic procedure for determining the model coefficient utilizing a *global equilibrium* between the subgrid-scale dissipation and the viscous dissipation (You & Moin 2007). In this approach, the model coefficient is globally constant in space but varies in time, and it still guarantees zero eddy viscosity in the laminar-flow regions. The model does not require any *ad hoc* numerical stabilization or clipping operation which is usually necessary in the local-equilibrium based dynamic models.

Secondly, it has been difficult to selectively resolve dynamically important separated flow regions using H- and O-type curvilinear mesh topologies, which are most commonly used in rotor applications. Previous experience with wall-resolved LES of turbulent flows indicates that streamwise and spanwise spacings of about 50–100 and 30–50 wall-units, respectively, are required in the separated flow region and wake. Although local-refinement or overset type grids may be used, it is known that numerical errors associated with the spatial interpolation adversely affect the simulation results. In the present method, the issue is overcome by an unstructured-grid topology, which provides higher flexibility and efficiency in distributing mesh resolution (figure 3.3(a)).

Furthermore, the high CFL number restriction in the local dense mesh region is alleviated with the use of a hybrid implicit/explicit time-advancement scheme. The discretized governing equation (3.1) is recast as

$$\frac{\partial U}{\partial t} = H(U), \quad (3.3)$$

where $U = (U_1^T, U_1^T, U_1^T, \dots, U_N^T)^T$ is the solution vector and N is the number of grid points. Similarly, the right-hand side $H = (H_1^T, H_1^T, H_1^T, \dots, H_N^T)^T$ is the flux vector defined as

$$H_k = -\frac{1}{V_{\Omega_k}} \sum_f \sum_{j=1}^3 (F_j^f - G_j^f) n_j^f. \quad (3.4)$$

The right-hand side of equation (3.3) is decomposed as $H = H^e + H^i$, where H^e and H^i are the explicit and implicit parts of H . The stiffness of H is estimated from eigenvalues of the flux Jacobian matrix J as follows

$$J = \frac{\partial H}{\partial U} = [\mathcal{J}^{ij}], \quad \mathcal{J}^{ij} = \frac{\partial H_i}{\partial U_j}, \quad i = 1, 2, 3, \dots, N, \quad j = 1, 2, 3, \dots, N.$$

Since the computation of eigenvalues is very costly for large-scale simulations, we utilize the Gerschgorin theorem which gives a radius of a disc including all the eigenvalues of the Jacobian matrix, thereby providing maximum allowable time step size for stable zone of an explicit scheme. The decomposed equation is advanced in time using a semi-implicit Runge-Kutta method proposed by Le & Moin (1991).

This feature allows to adaptively divide the mesh into explicit and implicit zones (figure 3.3(b)) and leads to significantly reduced memory requirements while maintaining the advantage of an implicit integration scheme. This method is especially advantageous for long-time integration of low-pitch-rate unsteady separating flow.

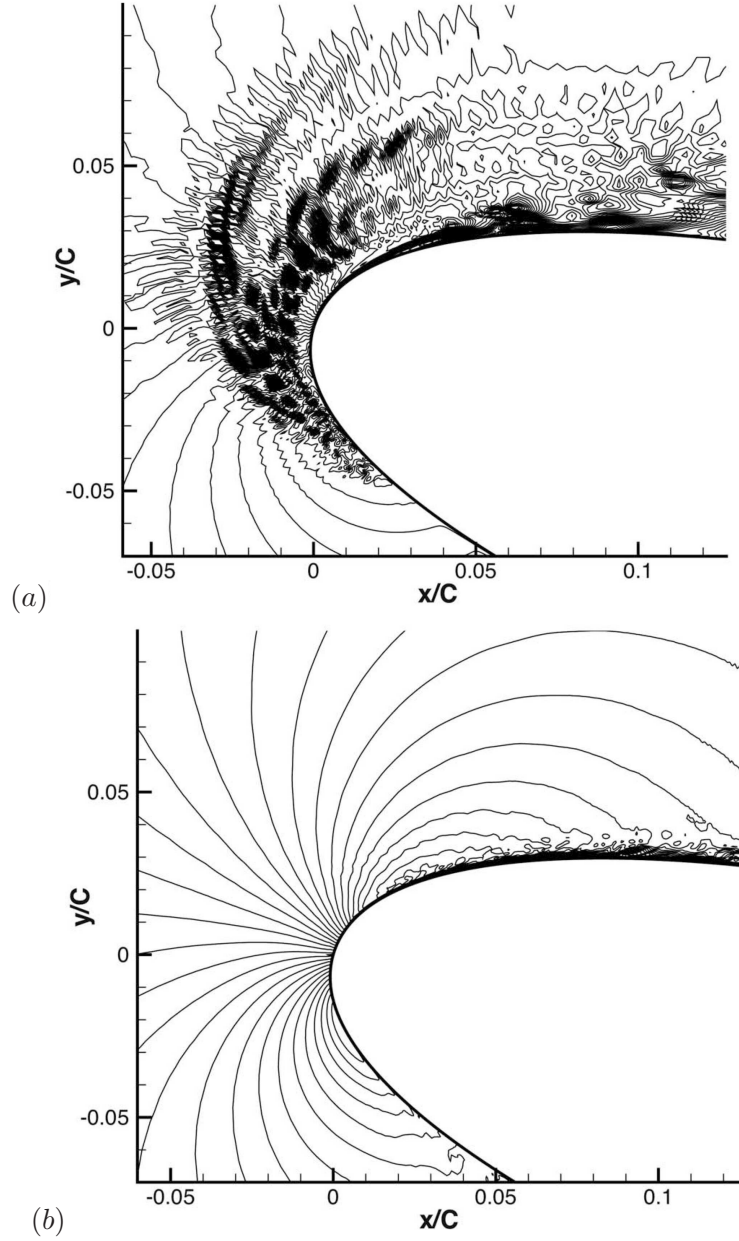


FIGURE 3.2. Contours of the instantaneous streamwise velocity around the leading-edge of an airfoil predicted by (a) LES based on a second-order centered finite-difference method on curvilinear coordinates and by (b) LES based on a second-order centered finite-volume method on Cartesian coordinates (the present scheme).

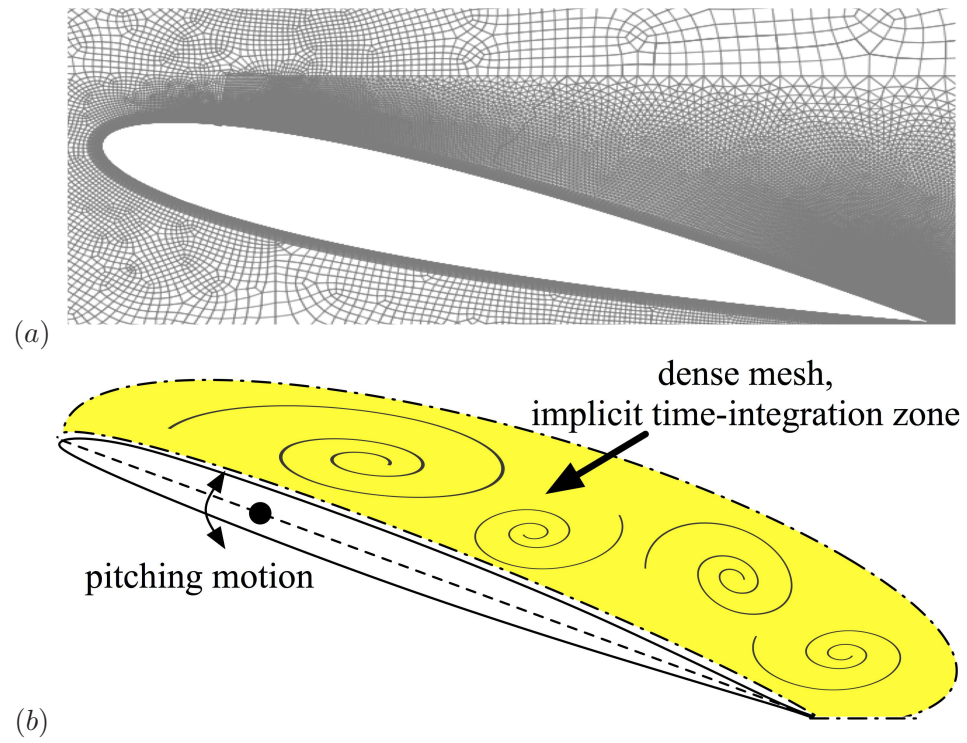


FIGURE 3.3. Schematic illustration of (a) a grid resolution topology and (b) separation of implicit and explicit time-integration zones.

CHAPTER 3. COMPUTATIONAL METHODOLOGY

Chapter 4

Flow over a pitching airfoil

4.1 Effects of mesh resolution

A series of computational grids were employed to investigate the effects of mesh resolution on the prediction of flow over a steady and pitching airfoils. As discussed in section 3.2, the present method utilizes advantages of using unstructured grid and adaptive implicit-explicit time-integration scheme. Each grid consists of multiple zones with different grid resolution. Grid lines are clustered around the suction surface of the airfoil and in the wake region so that the separated shear layer, recirculating flow, and turbulent wake are well resolved.

Most of the computational domain is discretized using hexahedral-shape elements. Especially near the airfoil surface, an elliptic-type mesh generator is employed to align grid lines to be parallel and orthogonal to the airfoil surface in the streamwise and wall-normal directions, respectively. As illustrated in figure 4.1, there are numbers of interfaces where mesh resolution is transitioned from fine to coarse. These interfaces are patched with prism-shape elements to maintain the quality of arrangement of primitive variables.

A mesh with about 6 million cells was designed first and employed for a coarse-resolution LES of flow over a steady airfoil at a fixed angle of attack in order to assess the resolution requirement. Subsequently, a 24 million cell mesh is designed.

Figure 4.2 shows pressure distributions on the surface of the Sikorsky SSC-A09 airfoil at a fixed angle of attack of 14 degrees. The Reynolds number and Mach number are 2×10^6 and 0.2, respectively. The pressure distribution predicted by the present LES on a 24 million-cell mesh is found to agree well with the experimental measurement in Lorber & Carta (1987). The near wall resolution in wall units on the 24 million-cell mesh is found to be $\Delta x^+ = 50 - 450$, $\Delta y^+ = 1 - 2$, and $\Delta z^+ = 60 - 130$.

4.2 Results and discussion

The 24 million cell mesh, which was demonstrated to be reasonably capable of predicting flow over the Sikorsky SSC-A09 airfoil at the operating Reynolds and Mach numbers, is also

employed for large-eddy simulations of flow during a pitching motion of the airfoil. To avoid mesh rotation or re-meshing during the pitching motion, the Favre-filtered compressible Navier-Stokes equations are recast into forms in a non-inertial reference frame. Therefore, large-eddy simulations are performed for variables in a non-inertial reference frame along with the effects of the Coriolis, centrifugal, and rotational acceleration forces.

Simulations are ongoing for two different cases. The first case corresponding to an experimental case conducted at Mach number of 0.2 and a sinusoidal pitching motion of which angle of attack varies in time as follows:

$$\alpha(t) = 20^\circ - 10^\circ \cos(\omega t),$$

where α is the angle of attack as defined in figure 3.1 and ω is the reduced frequency and is $0.10 \times 2U_\infty/c$. The second case also corresponds to an experimental case conducted at Mach number of 0.3 and a sinusoidal pitching motion as follows:

$$\alpha(t) = 12^\circ - 8^\circ \cos(\omega t),$$

where the reduced frequency is identical to the first case.

These two simulations are ongoing while the present simulations confirm the stability and effectiveness of the presented numerical schemes for dynamic stall simulations at realistic operating Reynolds and Mach numbers.

Large-eddy simulations are being conducted with the acoustic Courant-Friedrichs-Lewy (CFL) numbers of 25 and 20 for Mach number of 0.2 and 0.3 cases, respectively. The acoustic CFL numbers correspond to the time-step sizes of 0.27×10^{-3} and 0.23×10^{-3} normalized by the airfoil chord length and the speed of sound for Mach 0.2 and 0.3 cases, respectively. Using 512 cores of SGI Altix ICE 8200LX computer, about 12 - 16 days are required for large-eddy simulation over a pitching period when a 24 million-cell mesh is employed.

Figures 4.3 and 4.4 show gross features of flow over pitching airfoils at two different conditions. The characteristics of flow separation and reattachment processes are qualitatively congruent with experimental observation by Lorber & Carta (1987).

In figure 4.5, the lift coefficient and the pressure drag coefficient over the pitching airfoil are compared against the experimental data of Lorber & Carta (1987) as a function of pitch angle during a pitching cycle at Mach number of 0.2. Overall, the lift coefficient is in good

agreement with the experimental data. However, in the early stage of downward pitching motion ($30^\circ \rightarrow 23^\circ$), a noticeable deviation of the pressure drag is predicted by the present LES when compared to the experimental data.

The pitching moment coefficient over a pitching cycle is plotted in figure 4.6 (top) and is found to well agree with the experimental measurement. The variation of the pressure coefficient near the leading edge of the pitching airfoil ($x/c = 0.005$) is also found to be in good agreement with the experimental data as shown in figure 4.6 (bottom).

4.3 Summary

To gain a quantitative understanding of the unsteady separation process over a pitching airfoil, large-eddy simulations (LES) of turbulent flow over a pitching airfoil at realistic Reynolds and Mach numbers have been conducted. A novel combination of discretization schemes and time-integration schemes was employed to achieve numerical stability at high Reynolds number simulations through higher-order conservation and to be equipped with a highly efficient way to treat time-step size restriction in the separated flow region locally refined with dense mesh. The present simulations confirm the stability and effectiveness of the presented numerical schemes for dynamic stall simulations at realistic operating Reynolds and Mach numbers and show the characteristics of flow separation and reattachment processes which are qualitatively congruent with experimental observation.

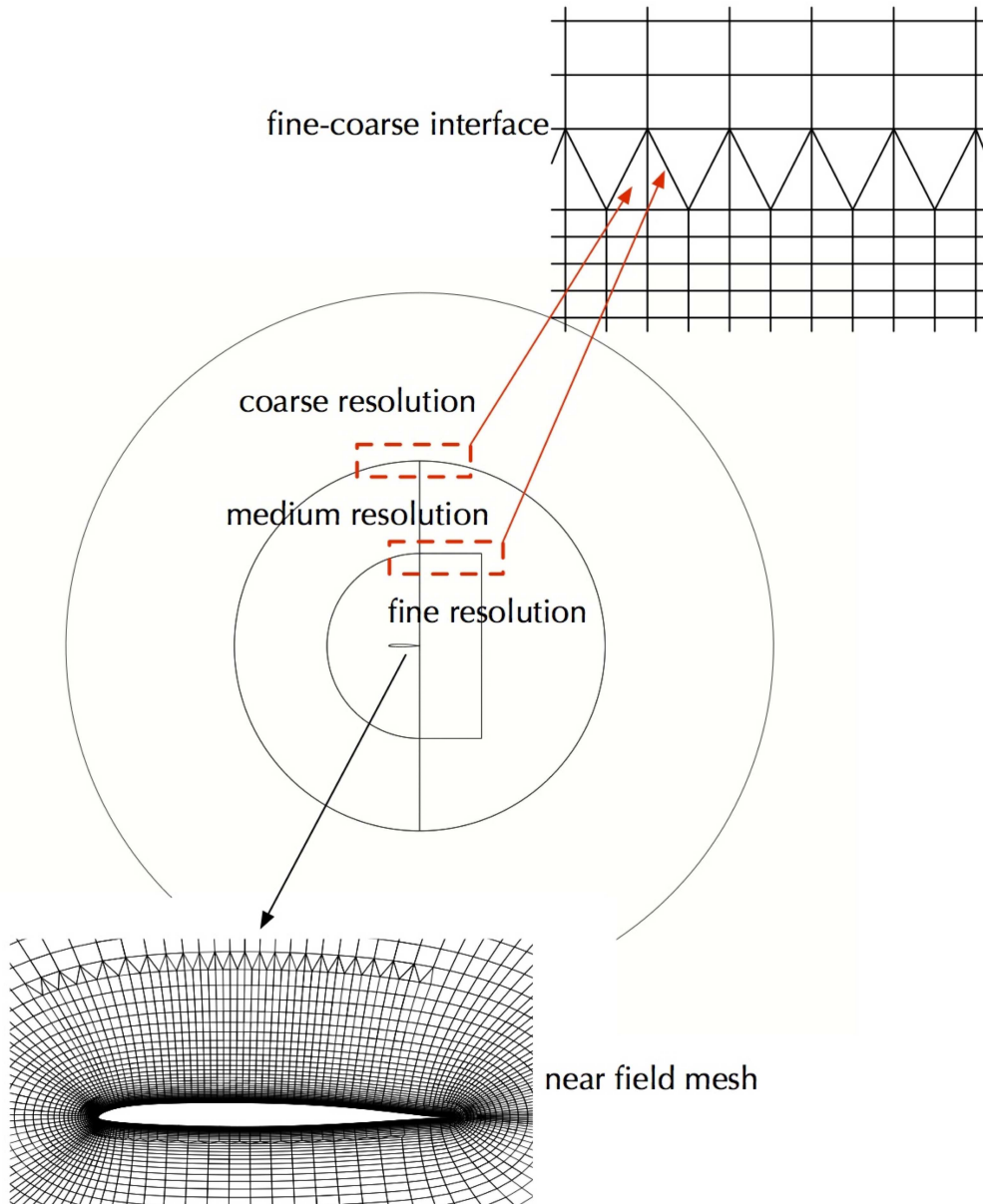


FIGURE 4.1. Computational grid topology for LES of flow over a pitching airfoil.

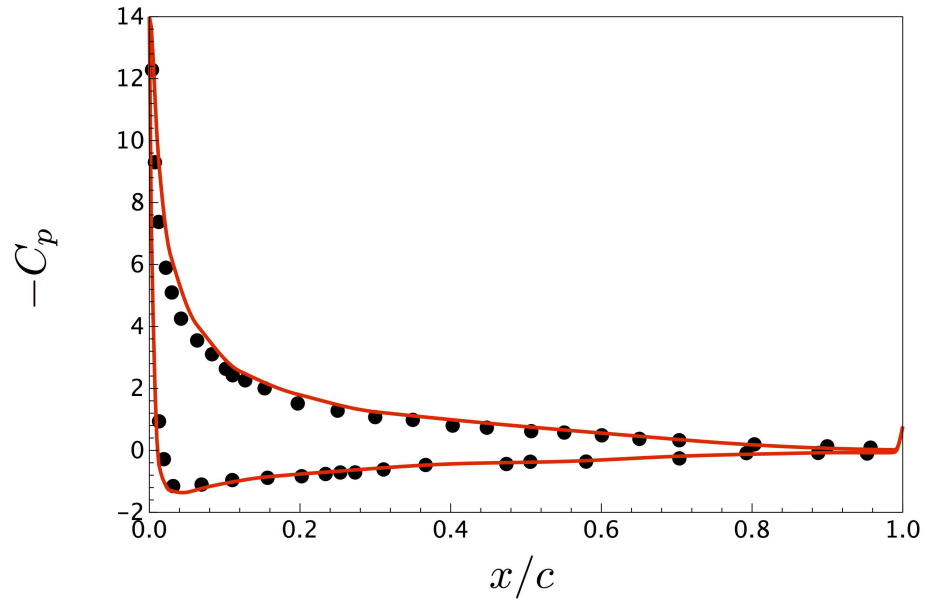


FIGURE 4.2. Pressure distribution on the airfoil surface at the angle of attack 14 degrees. Solid line, the present LES solution on a 24 million-cell mesh; symbol, experimental data.

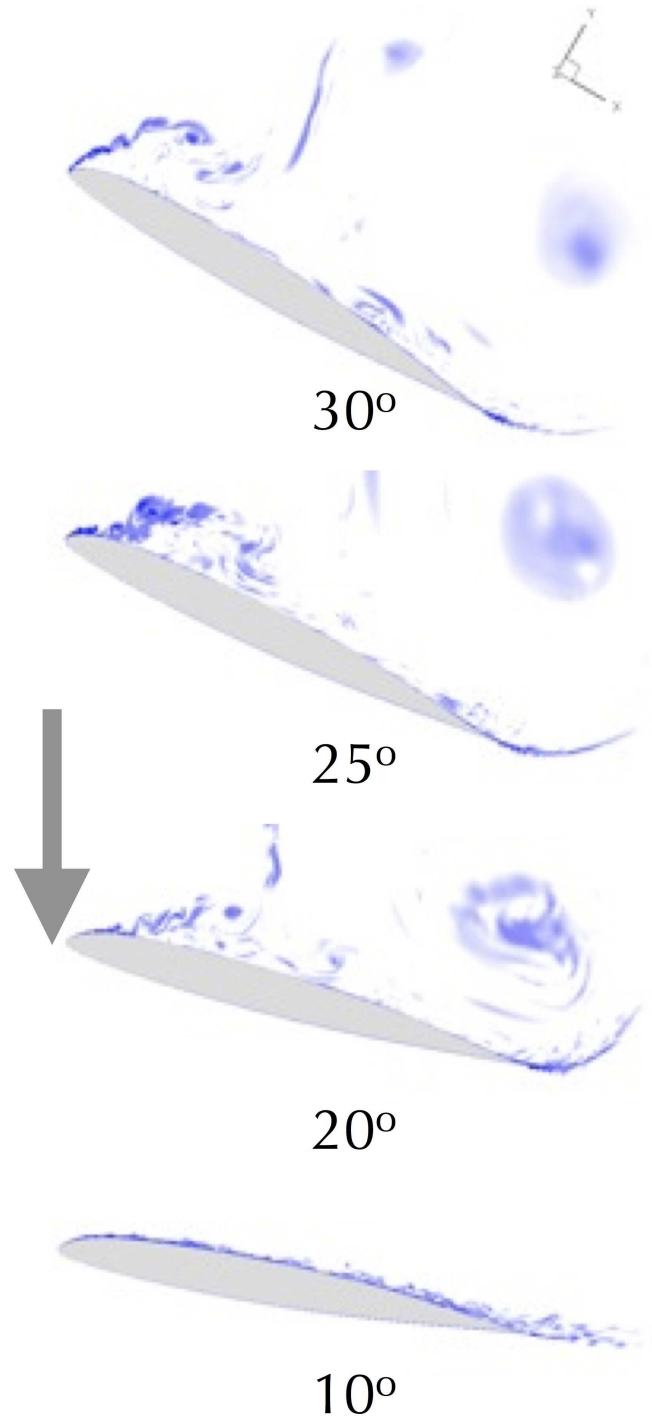


FIGURE 4.3. Contours of the spanwise vorticity predicted by the present LES over a half period of pitching motion at Mach number of 0.2.

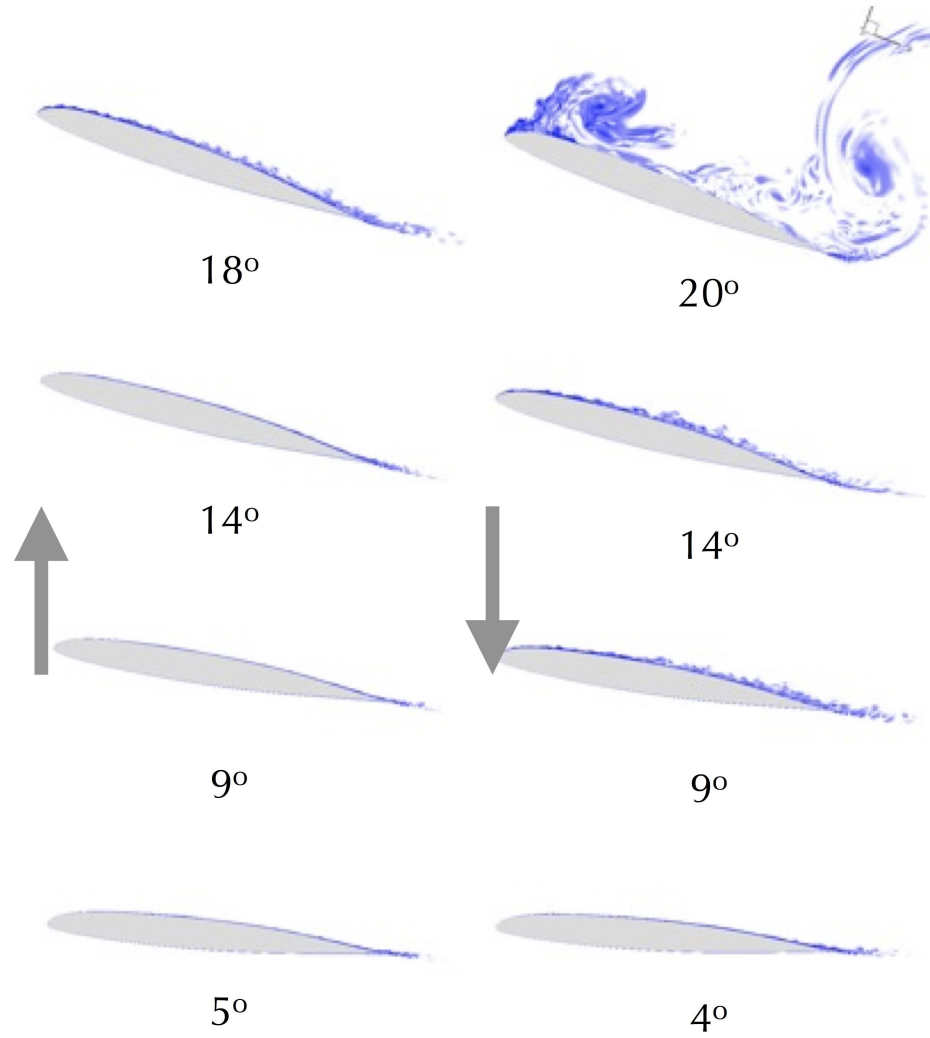


FIGURE 4.4. Contours of the spanwise vorticity predicted by the present LES over a period of pitching motion at Mach number of 0.3.

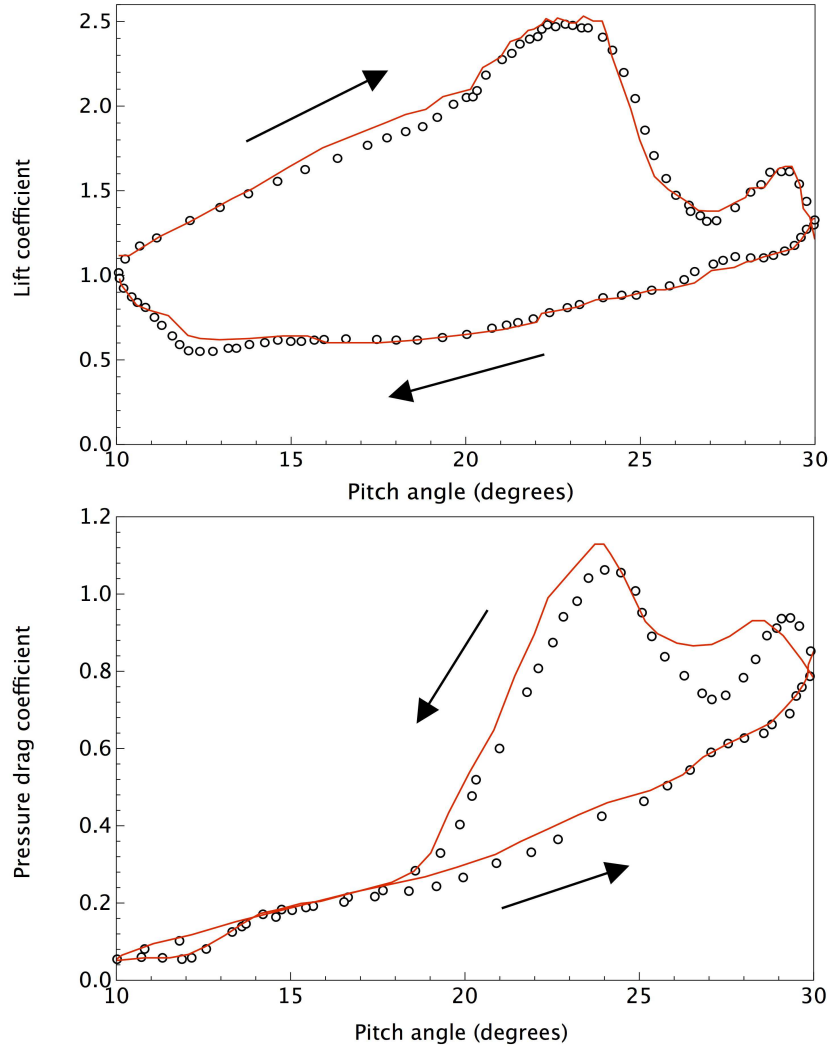


FIGURE 4.5. Lift coefficient and pressure drag coefficient as a function of pitch angle at Mach number of 0.2.

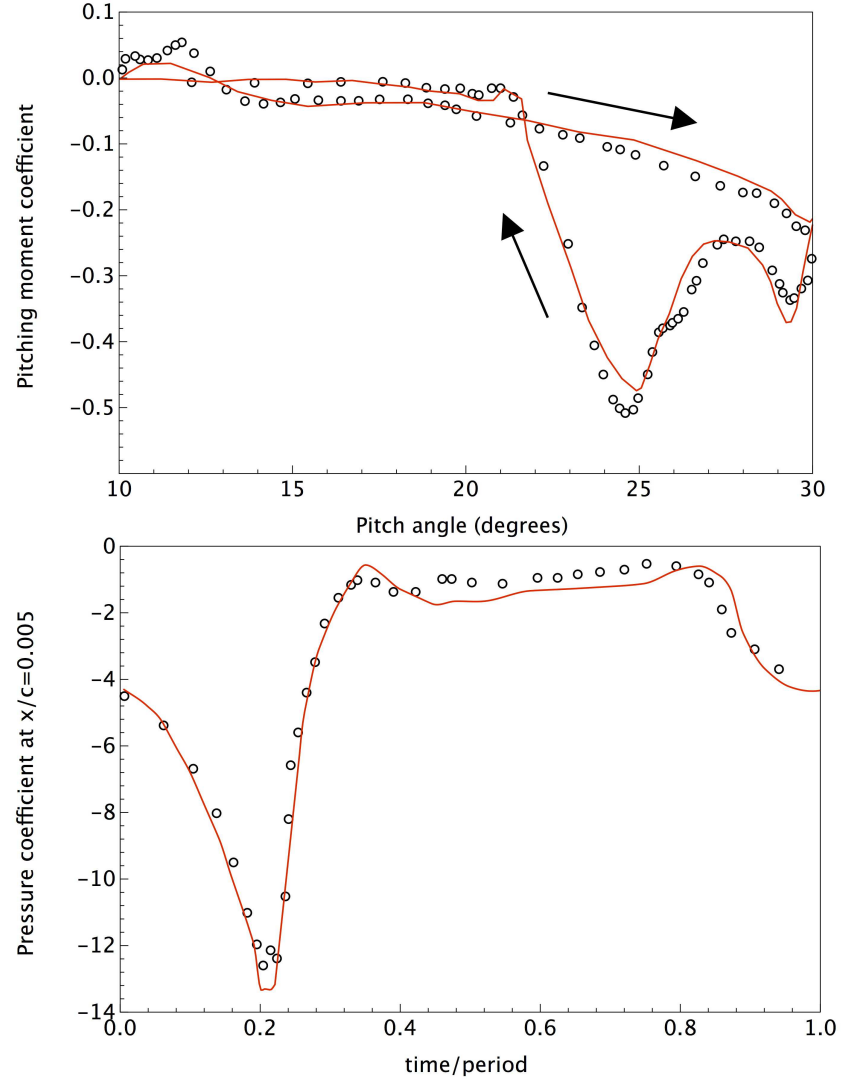


FIGURE 4.6. Pitching moment coefficient and pressure coefficient at $x/c = 0.005$ as a function of pitch angle at Mach number of 0.2.

CHAPTER 4. FLOW OVER A PITCHING AIRFOIL

Chapter 5

Direct numerical simulation of unsteady separation of turbulent boundary layers

5.1 Introduction

The term, turbulent flow separation, describes a process of detachment of turbulent boundary-layer flow from the wall. In contrast to a steady separating turbulent boundary layer, where the detachment location is statistically fixed, in an unsteady separating turbulent boundary layer, the flow detachment location varies in time due to an organized time-dependent flow condition and/or a time-varying wall motion (Simpson, 1989; McCroskey, 1982). Understanding unsteady separation of turbulent boundary layers has considerable practical significance because unsteady separation often characterizes the performance and efficiency of many aerodynamic applications such as helicopter rotor blades, wind turbine blades, pitching and flapping airfoils and wings, and rotating turbomachinery blades.

For instance, helicopter rotor blades experience a pitching motion which leads to unsteady flow separation followed by load and pitching-moment overshoots. The unsteady flow separation can in turn lead to unacceptably large vibratory loads and acoustic noise, and limit forward flight speeds and maneuverability. Steady separation of a turbulent boundary layer over an airfoil is often converted to unsteady separation when the separation is controlled by oscillatory blowing-suction actuations such as synthetic jets (Gilaranz *et al.*, 2005). The separation point over a composite-material propeller blade becomes time-dependent as the blade is deformed during the operation.

In spite of past experimental and numerical studies on separating flows in both modeled and realistic configurations, quantitative aspects of unsteady separating turbulent boundary layers, such as Reynolds stress and vorticity budgets, velocity and pressure fluctuations, and spatiotemporal correlations of primitive variables, are not well understood. Agarwal & Simpson measured phase-averaged velocity profiles in an unsteady separating turbulent boundary layer over a flat plate where the unsteady adverse pressure gradient was imposed

by time-varying upper-wall suction (Agarwal & Simpson, 1990). They suggested that quantitative measurements of Reynolds stresses and turbulence structures near the wall in the separated flow region are necessary to improve our understanding of the unsteady separation process. However, most experimental studies have concentrated on measurements of aerodynamic forces such as the surface pressure and overall loads, or on the flow-field visualization. Quantitative measurements of the unsteady separated flow field have been difficult using experimental techniques, and therefore, have rarely been reported in the literature.

Computational works, especially at practical Reynolds numbers, have mostly been performed using the Reynolds-averaged Navier-Stokes (RANS) equations or its unsteady counterpart (URANS) (*e.g.*, Visbal (1988); Spentzos *et al.* (2005)). However, it is known to be very challenging for (U)RANS to accurately predict highly unsteady flow involving incipient flow separation, formation and evolution of stall vortices, and reattachment. So far, none of the available turbulence models have shown a satisfactory predictive performance for all of these flow phenomena. A comprehensive database, especially Reynolds stress equation budgets, would be highly valuable for progress in this area. In a review article, Carr & McCroskey (1992); McCroskey (1982) concluded that under this condition (unsteady separation), the use of a turbulence model based on equilibrium attached boundary layers in steady flow (*e.g.*, eddy viscosity, Baldwin-Lomax) is open to question. The task of predicting separation by definition deals with boundary layers that have experienced strong pressure gradients, often both positive and negative; the flow approaching unsteady separation contains high levels of vorticity induced by these pressure gradients, and is strongly unsteady. Recent study has shown that modification of the turbulence model can completely change the resultant flow; at the same time, very little has been experimentally documented about the character of turbulence under these conditions.

The unsteady separation process is known to be highly dependent on the unsteady characteristics and strength of the adverse-pressure gradient while the dependence on the Reynolds number is virtually unknown (McCroskey, 1982). Although, in many cases, the surface curvature also influences the separation of turbulent boundary layers, it would be instructive to isolate the effects of the unsteady adverse pressure gradient by considering a flat plate surface with imposed adverse pressure gradients. Coleman & Spalart (1993) and Na & Moin (1998) performed direct numerical simulations (DNS) of steady separated turbulent boundary layers on a flat plate with an imposed steady adverse pressure gradient.

They were able to provide insight into the characteristics of steady separated flows and flow-field databases containing complete budgets of Reynolds stresses. However, for unsteady separating turbulent boundary layers, such detailed characterization of flow physics and comprehensive flow-field databases are not available so far.

In this study, we will employ a computational setup consisting of a turbulent boundary layer over a flat plate with a deliberate unsteady adverse pressure gradient imposed by time-varying blowing-suction on the upper boundary. The setup will allow us to focus on a quantitative physical understanding of the unsteady separation process including boundary-layer detachment and reattachment, and production and dissipation of turbulent kinetic energy and vorticity. An understanding of the characteristics of pressure fluctuations in unsteady separating turbulent boundary layers is also anticipated. Since the Reynolds shear stress and its gradient are largest away from the wall in separated flows, it has been suggested that the largest pressure fluctuations are not at the wall but away from it (Gilarranz *et al.*, 2005). Identifying the structure of pressure fluctuations away from the wall is critical to the prediction and understanding of turbulent boundary layer acoustics. DNS is ideal for the analysis of pressure fluctuations because static pressure within the flow cannot be measured experimentally.

5.2 Computational methodology

5.2.1 Flow configuration

The present DNS configuration is motivated by the experimental configuration of Agarwal & Simpson (1990) and is schematically shown in figure 5.1. In the present DNS, the inflow is a fully-developed zero-pressure-gradient turbulent boundary layer and is generated using a recycling technique developed by Lund *et al.* (1998). No-slip boundary conditions are used along the lower boundary of the computational domain while periodic boundary conditions are applied in the spanwise direction. At the exit, convective outflow conditions are employed to allow turbulence structures to smoothly leave the computational domain.

A novel feature of the present computational setup is that deliberate unsteady adverse pressure gradients (*e.g.*, replicating the oscillatory adverse pressure gradient in Agarwal & Simpson (1990)’s experiment) can be imposed by $V_{top}(x, t)$ which represents time-varying blowing and suction at the upper boundary. One way of obtaining approximate but reasonable $V_{top}(x, t)$ is to use a potential flow solution (from the panel method, for example).

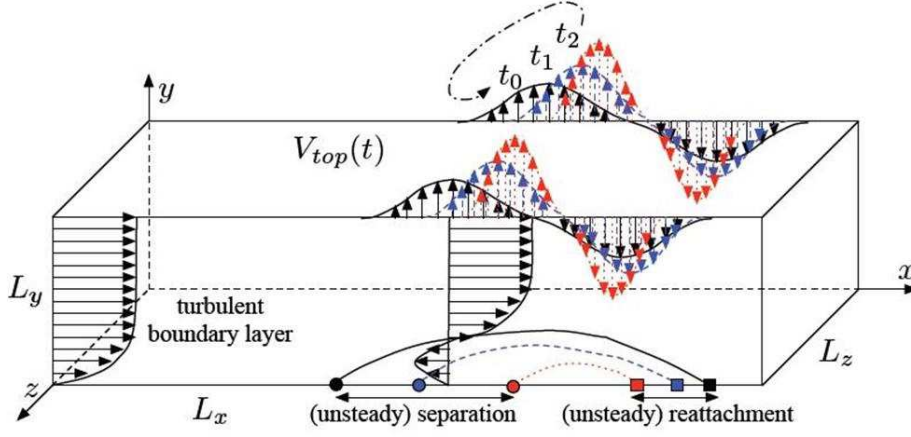


FIGURE 5.1. Schematic illustration of computational modeling of unsteady separating turbulent boundary layers.

Several iterations of viscous-inviscid calculations can be performed to improve the approximation. At the upper boundary, the streamwise velocity $U_{top}(x, t)$ is adjusted from a zero-vorticity condition prescribed by the equations (5.1, 5.2, 5.3):

$$v(x, L_y, z, t) = V_{top}(x), \quad (5.1)$$

$$\left. \frac{\partial u}{\partial y} \right|_{x, L_y, z, t} = \frac{dV_{top}(x)}{dx}, \quad (5.2)$$

$$\left. \frac{\partial w}{\partial y} \right|_{x, L_y, z, t} = 0, \quad (5.3)$$

where L_y is the height of the domain. This boundary condition assures zero vorticity in the spanwise and streamwise directions.

The distinct characteristics of unsteady separating turbulent boundary layers are revealed by a systematic comparison with steady attached/separated turbulent boundary layers. For this purpose, four different flow configurations are simulated: (i) turbulent boundary layer flow with a zero-pressure gradient (ZPG); (ii) turbulent boundary layer flow with an adverse-pressure gradient (APG); (iii) steady separated turbulent boundary layer flow (SBL); and (iv) unsteady separating turbulent boundary layer flow (USBL).

For all configurations grid spacings in the streamwise and spanwise directions are uniform. In the wall-normal direction, the grid is stretched based on a one-parameter hyperbolic tangent function described by Na & Moin (1998). All simulations are performed in a

configuration similar to that employed by Na & Moin (1998). The extent on the domain in the streamwise direction is equivalent to $350\delta_{in}^*$, where δ_{in}^* is the displacement thickness at the inlet of the computational domain. The inlet location is defined as where $x = 0.0$, and is marked by the dotted line in figure 5.2. The spanwise and wall-normal domain sizes are 50 and $64\delta_{in}^*$, respectively, as shown schematically in figure 5.2. The Reynolds number is fixed to 300, based on the momentum thickness and freestream velocity at the inlet in all four flow configurations.

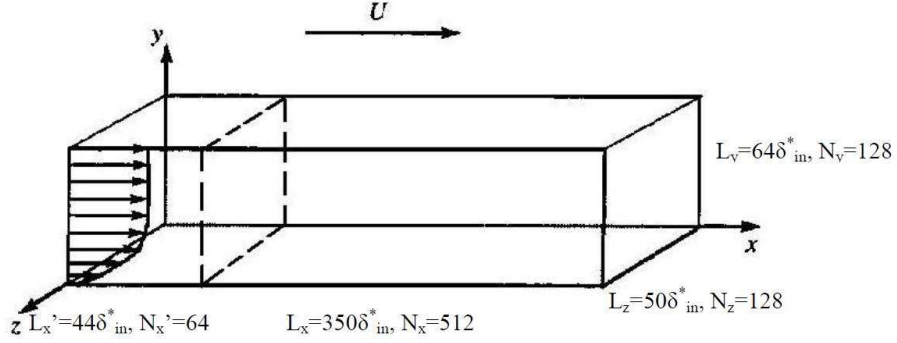
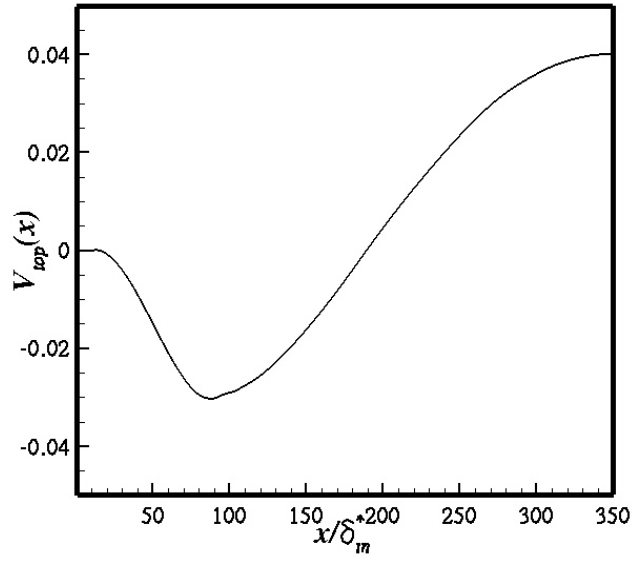


FIGURE 5.2. Computational domain sizes in terms of the inlet-displacement thickness and corresponding number of grid points.

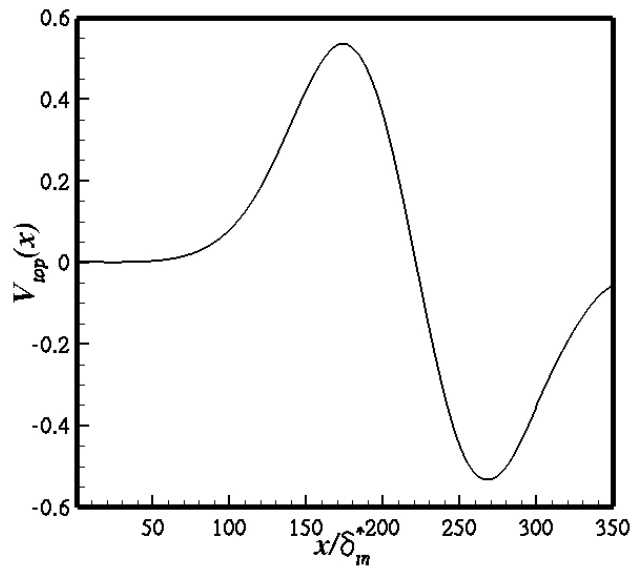
The $V_{top}(x)$ prescribed for the APG and SBL cases are shown in figures 3 (a) and (b), respectively, and correspond to the boundary conditions developed by Na & Moin (1998). The inflow zero-pressure gradient turbulent boundary layer is generated by a recycling technique developed by Lund *et al.* (1998) in the upstream region which extends the domain by $44\delta_{in}^*$, (L'_x in figure 5.2). In the USBL case a time-varying $V_{top}(x, t)$, which is similar in shape to that of SBL but oscillates in amplitude, is employed as illustrated in figure 5.1.

5.2.2 Numerical methods

The incompressible Navier-Stokes equations are discretized in space using a second-order central-difference scheme on a staggered grid. The discretized governing equations are integrated in time using a semi-implicit scheme. A low-storage third-order Runge-Kutta scheme is employed for treating convective terms explicitly and a second-order Crank-Nicolson scheme is employed for treating viscous terms implicitly. The hybrid Runge-Kutta/Crank-Nicolson scheme is combined with a modified fractional-step procedure, where



(a) APG



(b) SBL

FIGURE 5.3. Vertical velocity profiles imposed on the top boundary of the computational domain. Velocity magnitudes are normalized with the freestream velocity.

the divergence-free velocity field is obtained by solving the pressure Poisson equation only at the last substep. The Poisson equation is solved using multi-grid with Fast Fourier Transform in the spanwise direction. The numerical algorithm and solution methods are described in detail in You *et al.* (2007). The code has been modified for simulations of unsteady separating turbulent boundary layers. The present solver has been extensively validated in several cases of internal and external turbulent flows (*e.g.*, You *et al.* (2007)).

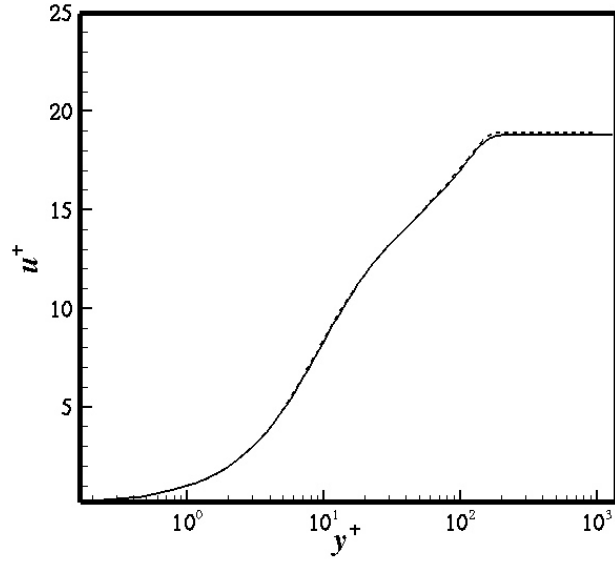
5.3 Results and discussion

5.3.1 Steady boundary layers

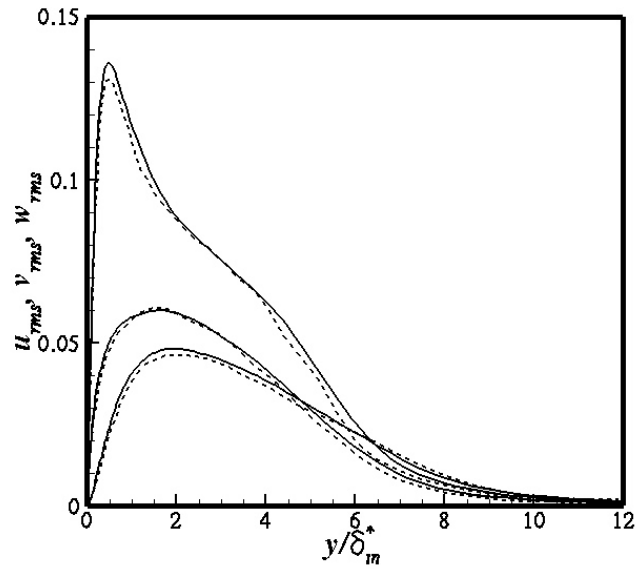
The present DNS results in the steady attached (ZPG and APG) and separated turbulent boundary layer (SBL) configurations are extensively validated against other available DNS data. Data collected from the ZPG configuration agrees very well with Na & Moin's results (Na & Moin, 1998). Some results of ZPG are shown in figure 5.4(b) and compared against results by Na & Moin (1998). Both the mean velocity and root-mean-squared fluctuating velocity profiles are recorded at $92\delta_{in}^*$ downstream from inlet.

Data collected from APG are shown in figures 5.5 and 5.6. Velocity profiles in wall-coordinates and root-mean-squared profiles are shown for three downstream distances. In the upstream location, the mean velocity and rms velocity fluctuation profiles are found to be nearly identical to those in the ZPG case. The change in the shape of the wall-coordinate velocity, shown in figure 5.5, is a result of the imposed adverse pressure gradient. The increase of the magnitude near the top boundary is a result of mass being inserted into the domain in the suction region of $V_{top}(x)$. The effect of an adverse pressure gradient on the distributions of the root-mean-squared profiles is shown in figure 5.6 in three streamwise locations. With the increasing streamwise distance, the peak of the streamwise velocity fluctuation profile gradually decreases in magnitude while the peak of the cross-stream velocity fluctuation profiles increases slightly, illustrating a slight increase in isotropy.

Figure 5.7 shows the mean velocity profiles in the SBL case in several upstream and downstream locations from the separation bubble. The time-averaged location of the separation bubble spans approximately from 150 to 260 inlet-displacement thicknesses (δ_{in}^*) downstream of the inlet. The increase in the streamwise velocity is due to the decrease in wall shear stress as the flow approaches the separation bubble (figure 5.7(a)). Unlike in the APG configuration, the blowing region precedes the suction. As a result, the mass flux



(a) Mean streamwise velocity in wall units



(b) RMS velocity fluctuations normalized with the freestream velocity

FIGURE 5.4. DNS results in the ZPG case. Na & Moin's results shown with dotted lines.

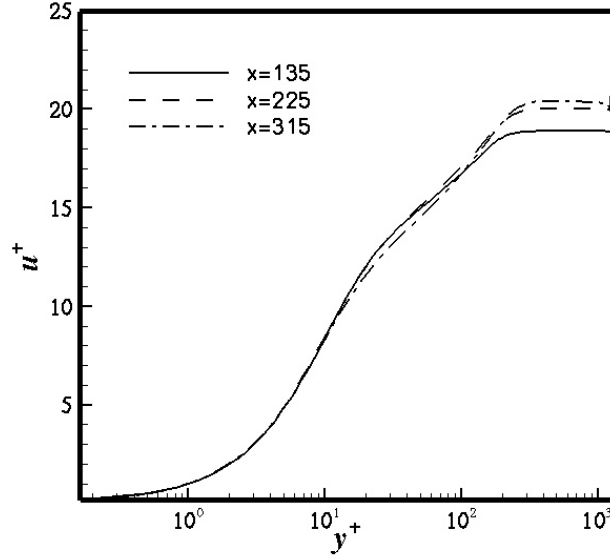


FIGURE 5.5. Mean streamwise velocity profiles in the APG case at three streamwise locations in wall units.

through the domain is minimized at the inflection point of $V_{top}(x)$, approximately $220\delta_{in}^*$ downstream of the inlet. Thus, unlike APG results (figure 5.5), where the mean velocity near the upper boundary increases through the adverse pressure gradient, it actually decreases in the SBL configuration (figure 5.7(b)). Downstream of the separation bubble, the shear stress begins to recover its original magnitude. This recovery does not require a considerable distance.

Profiles of the root-mean-squared velocity fluctuations in the SBL case are shown in figure 5.8. Profiles in figures 5.8(a)-(c) are computed inside the separation bubble, and profiles in figure 5.8(d) are computed well after reattachment. Figure 5.8(b) shows that the maximum turbulent kinetic energy is found away from the wall where the separation bubble height is maximized. This is because the energy-containing turbulent structures are lifted around the separation bubble. Downstream the near-wall peak of turbulent kinetic energy reappears, however the overall profiles are significantly altered from those in zero-pressure-gradient flow. Figure 5.9 illustrates the skin-friction coefficient throughout the computational domain. The change in the average spanwise spacing of the streaks from upstream to downstream of the separation bubble is clearly identified.

5.3.2 Unsteady separating turbulent boundary layer

Flow configuration

As mentioned in section 5.2.1 the time varying adverse pressure gradient is imposed by $V_{top}(x, t)$ in the USBL case. The $V_{top}(x)$ used in the SBL case, is multiplied by an amplification factor which is a function of time to create $V_{top}(x, t)$. The $V_{top}(x, t)$ used for the present USBL case employs a compound trigonometric function which produces a synco-pated amplification factor ranging between 1.0 and 0.6:

$$V_{top}(x, t) = V_{top}(x) * [\cos(\omega t - \sin(\omega t)) + 4.0]/5.0 \quad (5.4)$$

The period, $\frac{1}{\omega}$, is equivalent to 1.5 flow through times based on the freestream velocity and the potential separation bubble length, *i.e.* the maximum distance between detachment and reattachment locations. One cycle of the amplification factor as a function of the phase number is shown in figure 5.10.

Unsteady flow-reversal

The time-dependent boundary condition results in a separation bubble which intermittently stops circulating, and subsequently becoming what will be referred to as a hump. Figure 5.11 shows the spanwise-averaged fraction of time ($\bar{\gamma}_u$) that the flow moves downstream for a series of phases. The stalling of the circulation, and full attachment, is a direct result of the changes in streamwise pressure gradient. It should be noted that the pressure field at a given time, τ , is not only a function of the magnitude of $V_{top}(x, \tau)$, but also depends on

its time rate, $\frac{\partial V_{top}(x,t)}{\partial t}|_{\tau}$. The phase of the pressure field, and circulation response, lead the phase of the amplification factor.

The skin-friction coefficient, C_f , depicts the region in which flow is reversed. Figure 5.12 illustrates the streamwise distribution of C_f and pressure coefficient, C_p , evaluated at the wall. Time-averaged $V_{top,max}(x,t)$ closely resembles that in the SBL case. However, the phase-averaged pressure distribution in each phase deviates significantly from the time-averaged pressure distribution. The pressure field is shifted such that a point near the top boundary in the far upstream remains zero throughout the simulation. The variation in wall C_p , $\frac{\partial p}{\partial x}|_{wall}$, leads the changes in C_f by approximately one phase. In the SBL case, the plateaus in both curves correspond closely in the streamwise location. In this USBL case, C_p varies considerably, while C_f exhibits little shifting in location. $\frac{\partial C_p}{\partial x}$ shows little variation in the boundary layer recovery region, $x/\delta_{in}^* > 300$.

Mean velocity field

As shown in figure 5.13, the averaged skin-friction and pressure coefficients in the USBL case are found to be nearly identical to those in the SBL case. This suggests that strong similarities would exist in other mean flow statistics between the USBL and SBL cases.

Upstream of the bubble the mean streamwise velocity profiles agree well each other (figure 5.14(a)). Inside the separation bubble in the SBL case, much stronger backflow is observed (figure 5.14(b)). This would be expected because during the USBL case the circulation is completely seized for at least ten percent of the cycle period. As a result of the decrease in average backflow the USBL case recovers more rapidly (figure 5.14(c)). And, downstream of the bubble, the similarity reappears (figure 5.14(d)), where both exhibit a depression below the log-law region, as observed by Na & Moin (1998).

Figures 5.15(a)-(d) illustrate differences in turbulence intensities between the USBL and SBL cases. While both SBL and USBL cases agree in the upstream location (figure 5.15(a)), the maxima in the SBL are shifted more away from the wall than those in the mean USBL case (figures 5.15(b) and (c)). In following sections, the changes in the separation bubble height (section 5.3.2) as well as the stability of the upstream boundary of the bubble which supplies the wall-normal momentum needed to push up incoming vortical structures (section 5.3.2) are discussed. Figure 5.15(d) shows the turbulence intensities after the reattachment. The SBL case displays a higher degree of isotropy, and also has more exaggerated near wall peaks in the streamwise and spanwise curves.

Figure 5.16 shows the turbulent kinetic energy and turbulent kinetic energy production and dissipation. The turbulent kinetic energy is a compilation of the rms velocity fluctuations and follows the similar trend of the turbulence intensities (figures 5.15(a)-(d)). As the detachment point is approached the peaks of the turbulent kinetic energy and turbulent kinetic energy production and dissipation move away from the wall. Both the production and dissipation decrease in magnitude, while the turbulent kinetic energy increases (figure 5.16(b)). Inside the bubble, the turbulent kinetic energy and turbulent kinetic energy production and dissipation become smaller, and toward the reattachment point, the vertical shifts between the two cases become negligible (figure 5.16(c)).

The time-averaged flow field is similar to that of the SBL case. There exists a hump in the streamlines throughout the boundary condition cycle, which remains slightly smaller than the separation bubble in the SBL case (figure 5.17). The contour lines shown in figure 5.17 illustrate the maximum and minimum heights that occur during the boundary condition cycle. The mean streamwise velocity contours above $\bar{u}/U_\infty = 0.4$ show little variation throughout the simulation. Likewise the wall-normal velocity contours in this upper region maintain a symmetric half-circle shape which heaves in phase with the syncopated $V_{top}(x, t)$. Within the boundary layer the mean streamwise velocity contours experience a much wider variation particularly during the brief $V_{top,min}(x, t)$ when the $\bar{u}/U_\infty = 0$ collapses onto the wall. The vertical displacement between $\bar{u}/U_\infty = 0.0$ and 0.4 maxima and minima is significantly different (figure 5.18). This suggests that the incipient mechanism of full reattachment is a thickening of the shear-layer which blankets the separation bubble. Streamwise velocity profiles in wall-coordinates are depicted in figure 5.19. In order to scale using shear stress velocity, u_τ , during separation, Skote & Henningson (2002)'s definition is employed:

$$u_\tau = \sqrt{-\nu \frac{\partial u}{\partial y} \Big|_{y=0}}. \quad (5.5)$$

Phases 5 and 9 are chosen because they represent phases in which the maximum and minimum backflow velocities occur, respectively. Interestingly, while the minimum backflow velocity occurs at the phase 9 (approximately $-0.07 * U_\infty$), the minimum shear stress occurs during phase 8 (figure 5.12(e)). While the phase in which flow is fully attached is easily identifiable using $\bar{\gamma}_u = 1.0$ and $C_{f,max}$, the phase in which the separation bubble is fully formed is much harder to define. In fact, the maximum $\frac{\partial p}{\partial x}$, minimum skin-friction

coefficient, minimum backflow velocity, and maximum bubble height all occur in consecutive phases, in the order listed.

Vortex identification and vorticity

Vortex identification is performed using the λ_2 definition of Jeong & Hussain (1995). The large scale structures present are consistently elongated in the streamwise direction (figures 5.20(a) and (b)). Their distribution before and after the separation bubble, or hump, have a direct influence on the streaks seen in wall shear stress contours (figures 5.20(c) and (d)). As the circulation reestablishes in the hump following full reattachment, the vortices in the detachment region begin to bunch up like a rug. This stall in motion results in a gap in structures on the leeward side of the bubble 5.20(b). Once development of the bubble is complete, the vortices advect over the bubble just as they do during the SBL case. When the circulation seizes and the flow reattaches the height of the structures is not greatly affected. However, downstream of the hump the spanwise spacing of large structures increases, and subsequently, λ_z , the average spanwise spacing of wall shear stress contour streaks (figure 5.20(c)). Throughout the simulation there is a void of vortices with the bubble and hump, despite full reattachment.

The orientation and inclination of the vortices indicates that the magnitude of the streamwise vorticity dominates the vorticity vector. This is true in all but the detachment region. During bubble development the bunching of the vortices described above also affects their orientation, and thus the wall-normal vorticity is actually fed by the structures that were oriented streamwise when they developed. Instantaneous contours of streamwise vorticity at two different streamwise stations are shown in figure 5.21. Contrary to the variation of bubble height observed based on mean velocity fields, the vorticity field in the leeward side of the hump actually grows in height upon full reattachment (figures 5.21(a) and (b)). However, downstream of the bubble, this relationship is inverted (figures 5.21(c) and (d)). This is best explained using Taylor's Hypothesis (Taylor, 1938). The heightening of the vorticity distribution seen during the attached phase(s) advects and appears downstream during subsequent phases. This also indicates that the region of decreased momentum which defines the hump, begins to advect during full attachment. It is a slow process, and begins weakly, so this motion is not readily apparent from mean velocity contours or large scale structures.

The lifting of the vortices seen in figure 5.20 can also be seen in sideviews of the vorticity

distributions (figure 5.22). Na & Moin describe the separation bubble in the SBL case as acting as a streamlined obstacle, not allowing the separation zone to be penetrated by the higher momentum flow. In figure 5.22(b) one can see that the seizure of circulation immediately allows the hump to be penetrated, near $x/\delta_{in}^* = 210$. Again, only weak vortical structures are allowed to pass, so this phenomenon is not readily apparent when viewing the mean contours or large scale structure motion.

5.4 Summary

Direct numerical simulations of turbulent boundary layers with steady and unsteady pressure gradients were performed to improve the understanding of unsteady separation processes of turbulent boundary layers. A time varying blowing-suction velocity distribution along the upper boundary induces an unsteady adverse pressure gradient to the turbulent boundary layer. This produces a separation bubble in which the backflow cycles between full separation and complete seizure of circulation. The distinct characteristics of unsteady separating turbulent boundary layers were revealed by a systematic comparison with steady attached/separated turbulent boundary layers.

In the USBL case, the process of creating and annihilating circulation is observed to be hysteretic. As the adverse pressure gradient subsides the shear layer which blankets the separation bubble begins to thicken. This continues until the flow is fully attached. As the circulation reappears the shear layer compresses at a slower rate. As a result the backflow exists in a flatter region and relatively high negative shear stresses are observed. Throughout the simulation the displacement thickness in the region of the bubble remains large. When circulation stops the bubble does not appear to advect downstream. The hump does however lose some of its strength, and allows vortical structures to penetrate its upstream face.

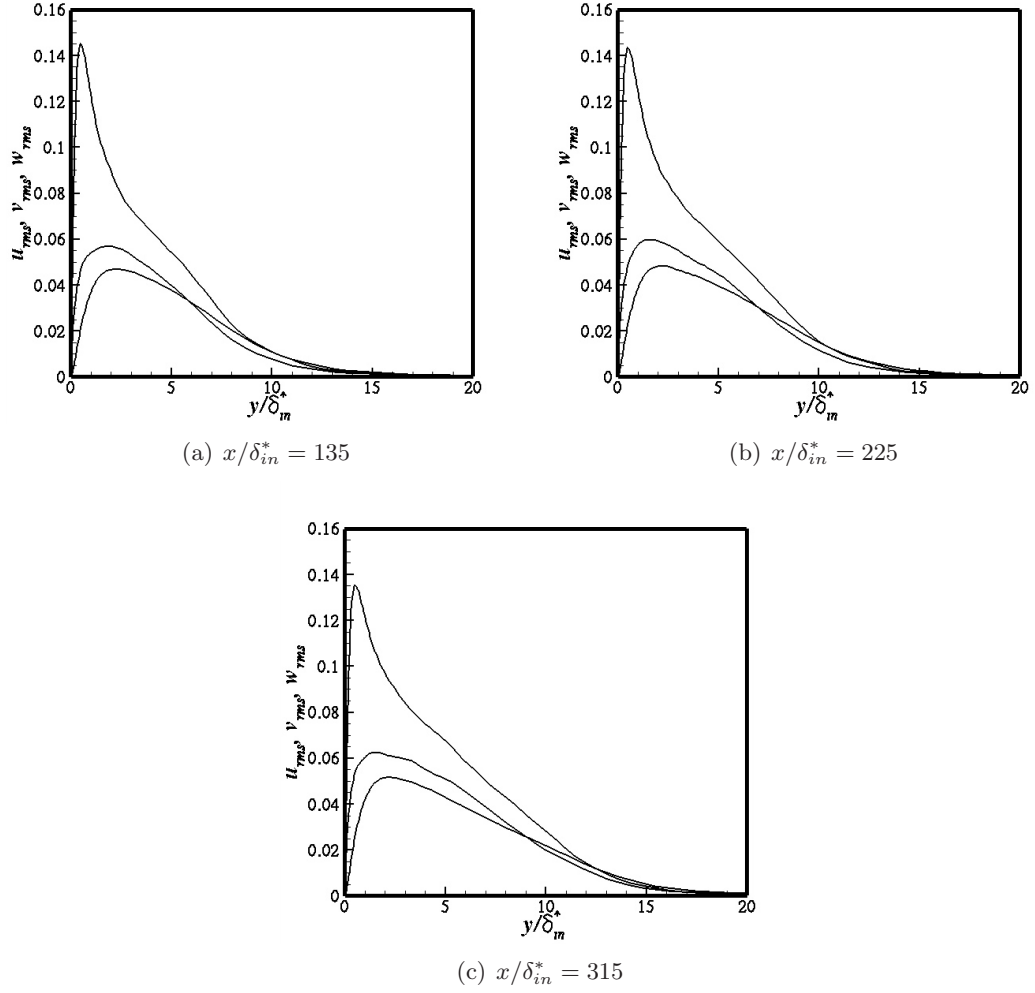
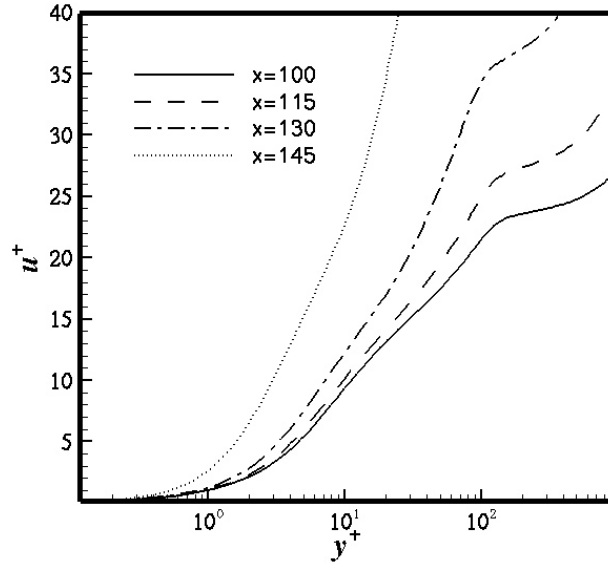
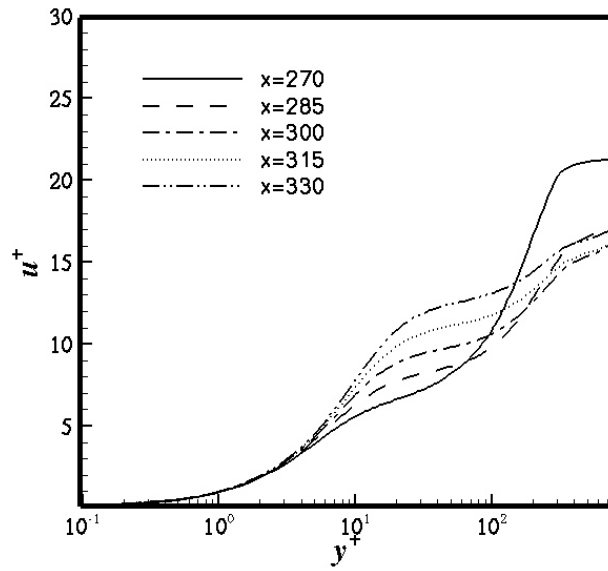


FIGURE 5.6. RMS velocity fluctuations in the APG case in three streamwise locations.

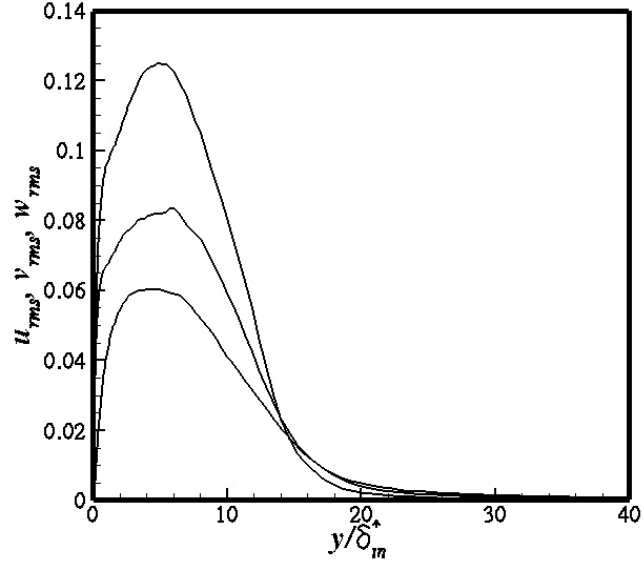


(a) Velocity profiles upstream of the separation

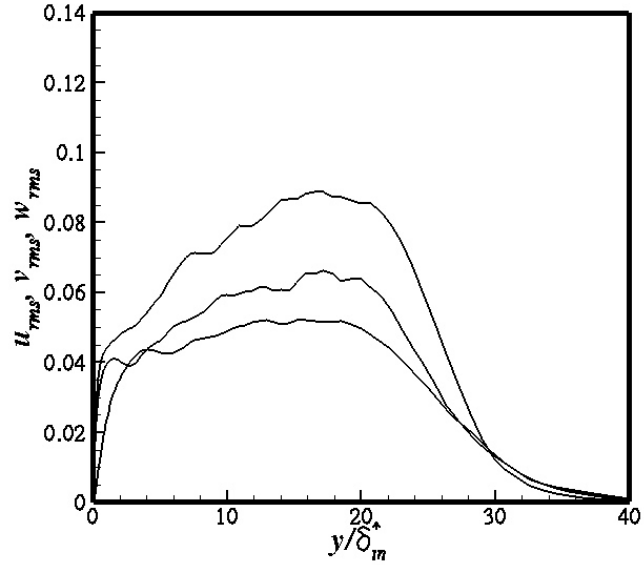


(b) velocity profiles downstream of the reattachment

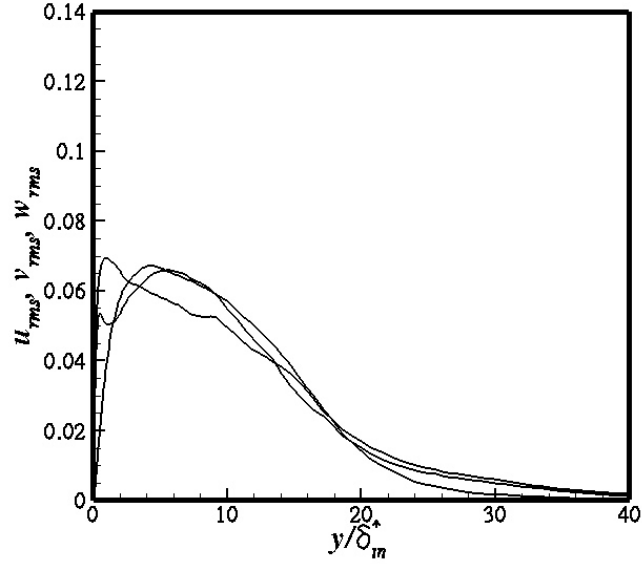
FIGURE 5.7. Mean streamwise velocity profiles in the SBL case in streamwise locations in wall units.



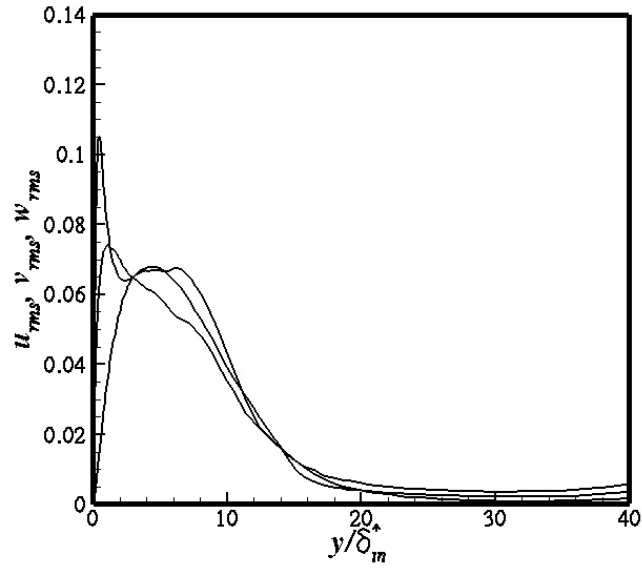
(a) $x/\delta_{in}^* = 160$



(b) $x/\delta_{in}^* = 220$



(c) $x/\delta_{in}^* = 270$



(d) $x/\delta_{in}^* = 330$

FIGURE 5.8. RMS velocity fluctuations normalized with the freestream velocity in the SBL case.

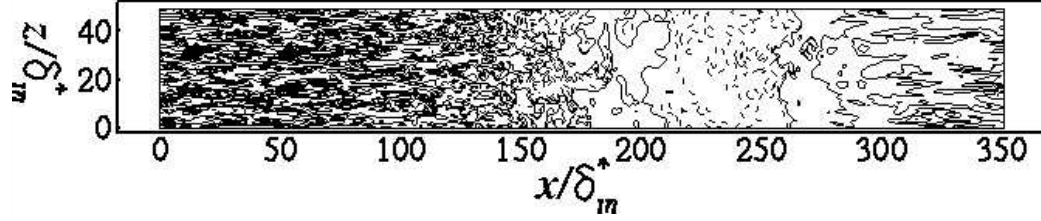


FIGURE 5.9. Contours of the instantaneous skin-friction coefficient. Negative values are dashed.

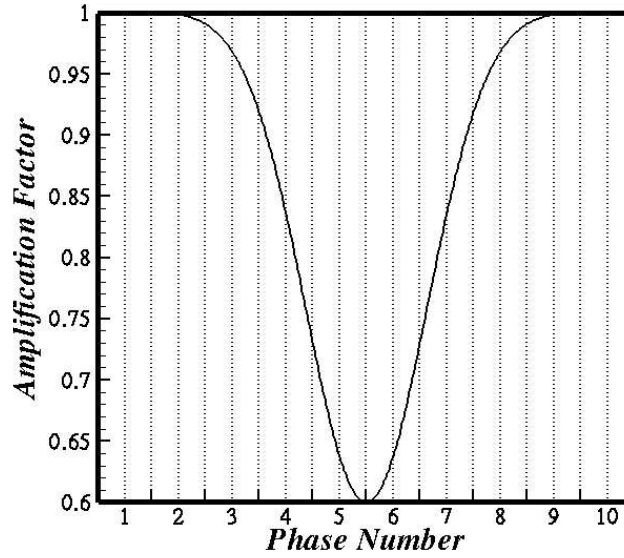
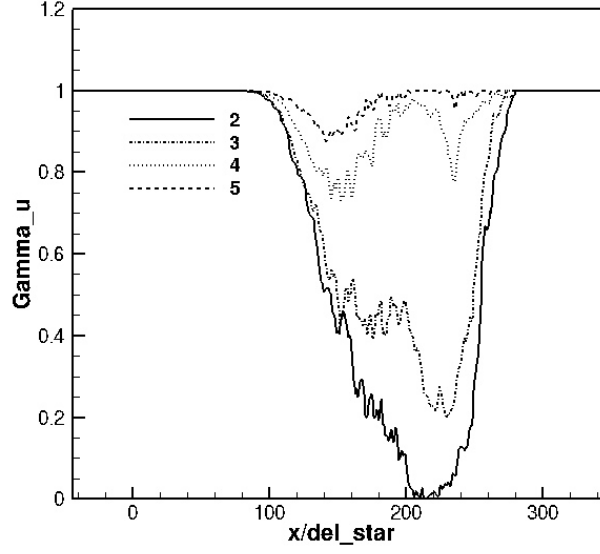
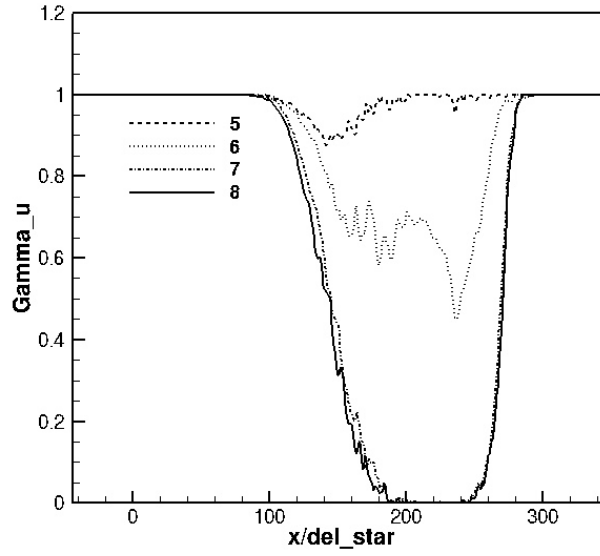


FIGURE 5.10. Amplification factor used to convert $V_{top}(x)$ to $V_{top}(x, t)$. x-axis indicates the phase number.



(a) $\bar{\gamma}_u$ distributions in phases 2-5.



(b) $\bar{\gamma}_u$ distributions in phases 5-8.

FIGURE 5.11. Spanwise-averaged fraction of time ($\bar{\gamma}_u$) that flow moves downstream.

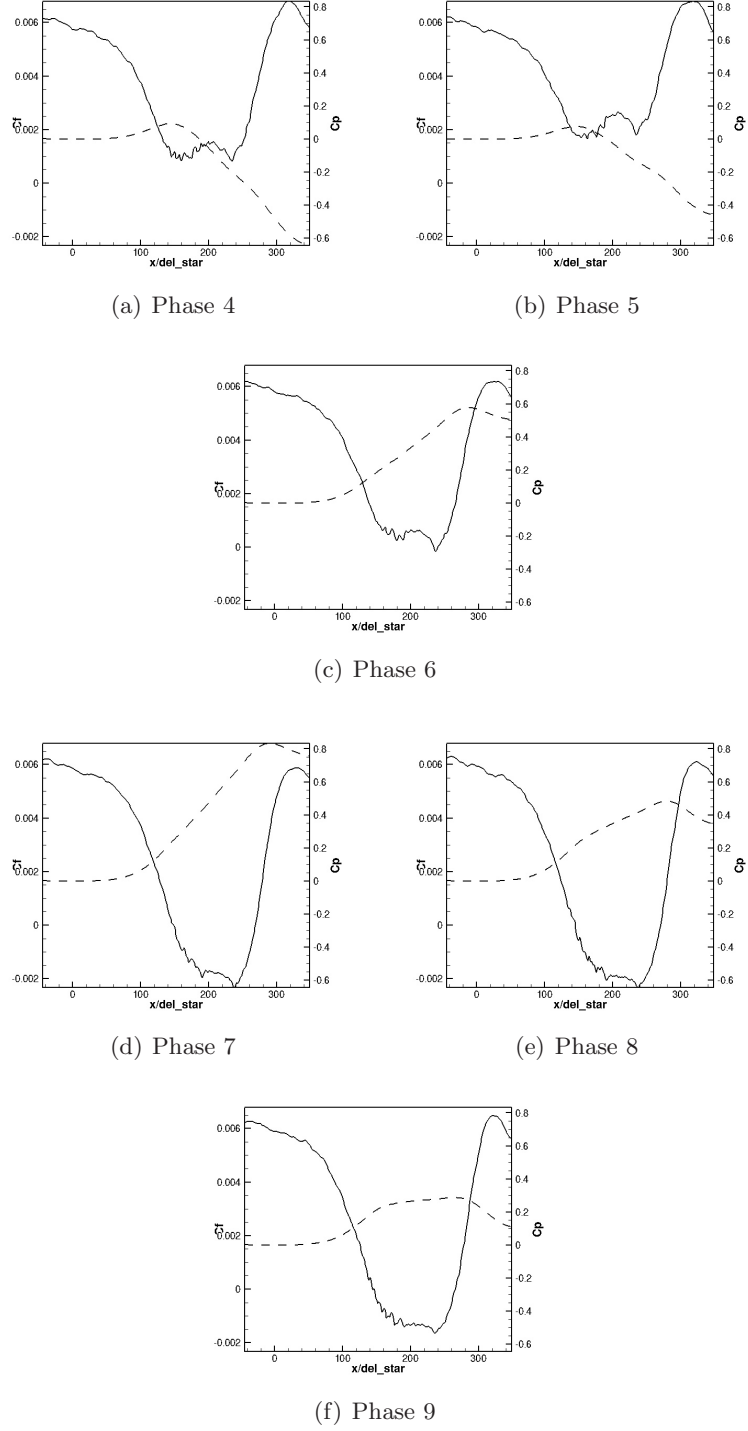
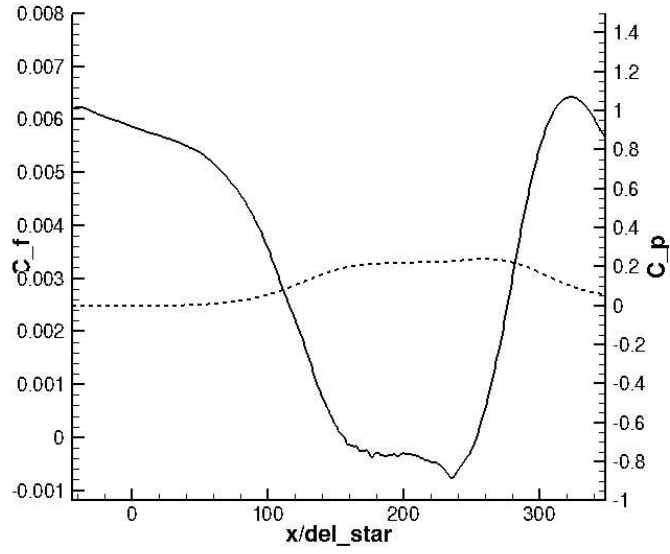
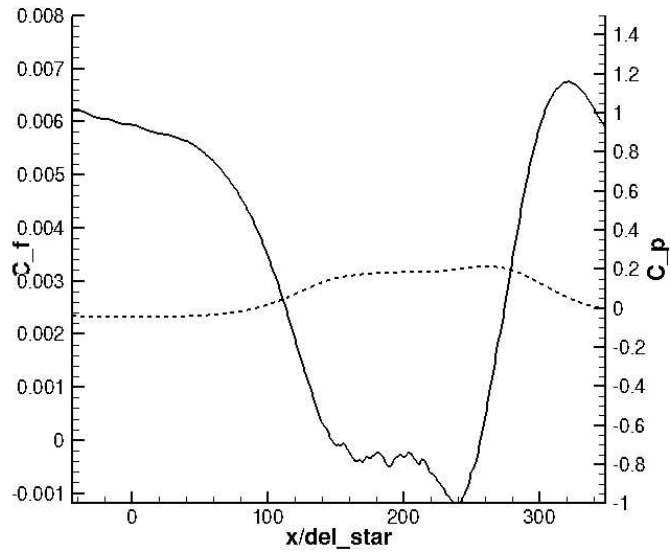


FIGURE 5.12. Streamwise distributions of phase averaged skin-friction and pressure coefficients.



(a) USBL



(b) SBL

FIGURE 5.13. Streamwise distributions of total averaged skin-friction and pressure coefficients.

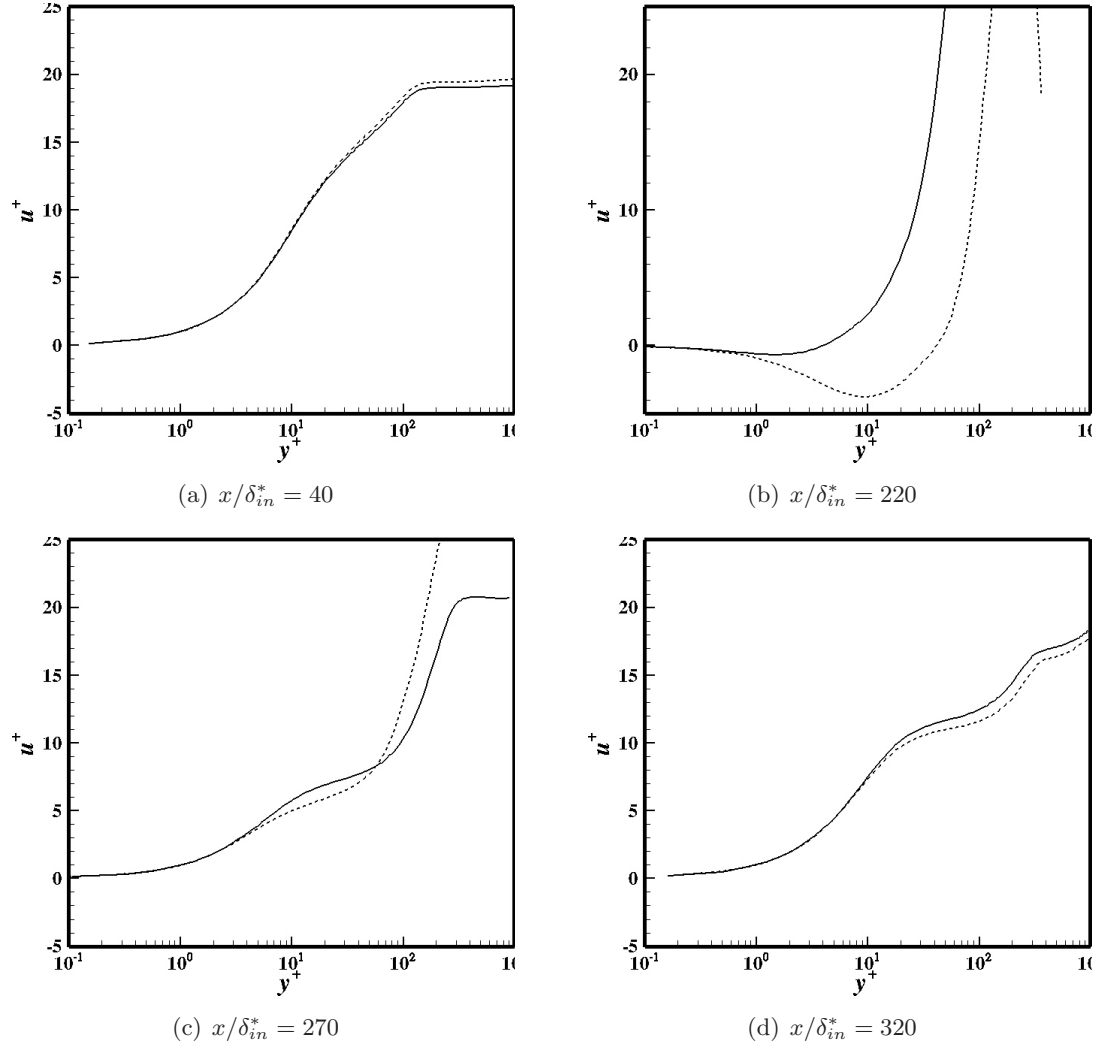


FIGURE 5.14. Streamwise velocity profiles in wall units. — USBL; -- SBL.

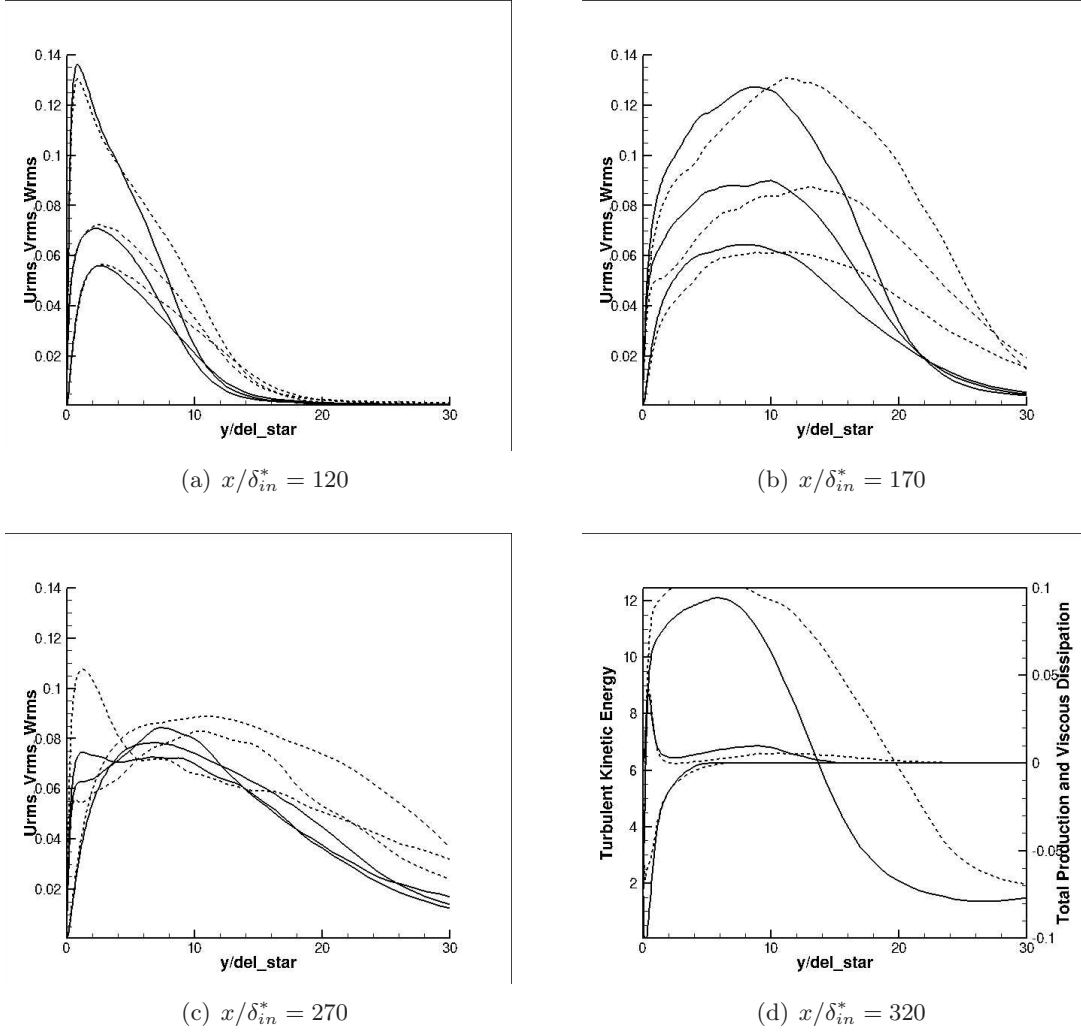


FIGURE 5.15. Turbulence intensity profiles normalized with U_∞^2 . — USBL; -- SBL.

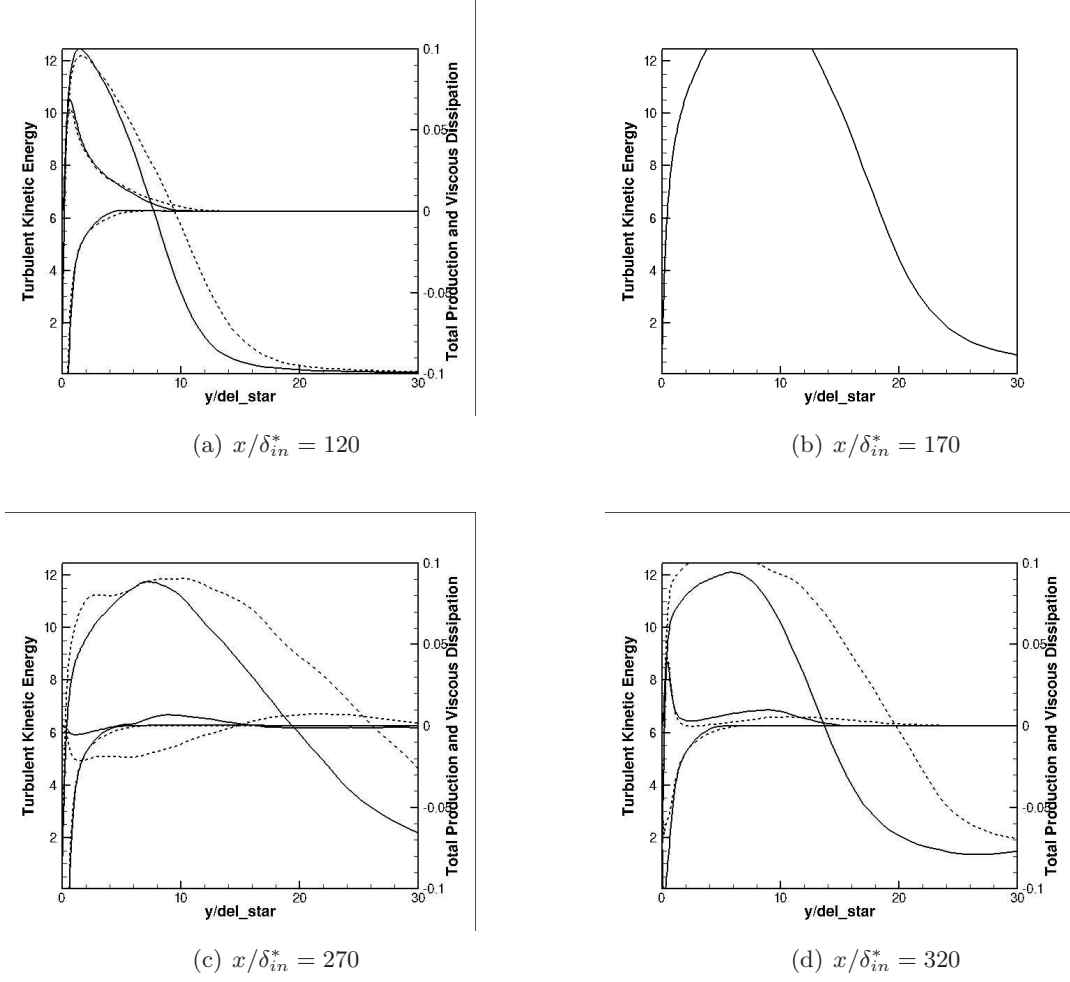


FIGURE 5.16. Comparisons of the turbulent kinetic energy and turbulent kinetic energy production and dissipation normalized with $\frac{U_\infty^3}{100\delta_{in}^*}$. — USBL; -- SBL.

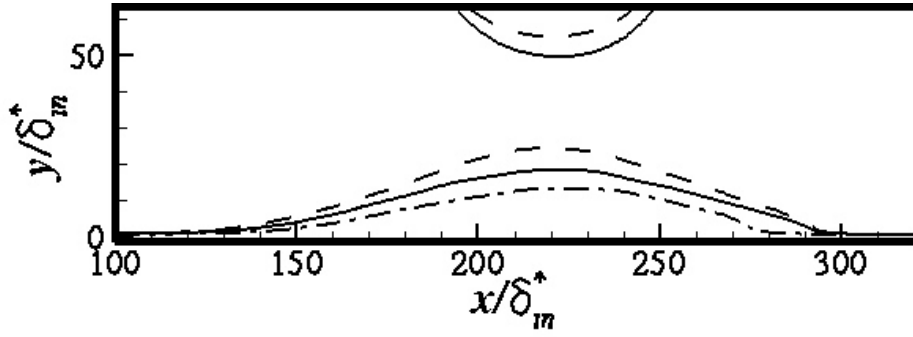


FIGURE 5.17. Contours of $\bar{u}/U_\infty = 0.4$; -- SBL; — Phase 1; -.- Phase 6.

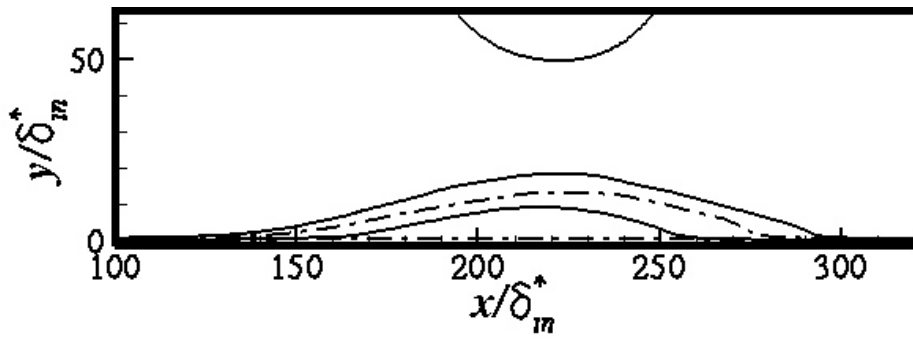
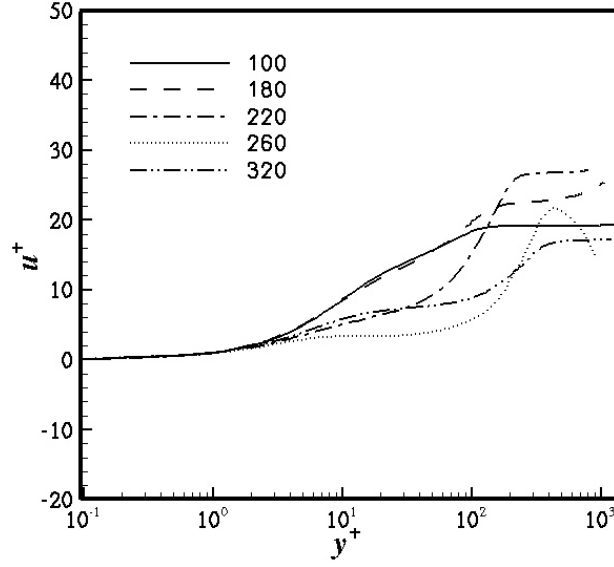
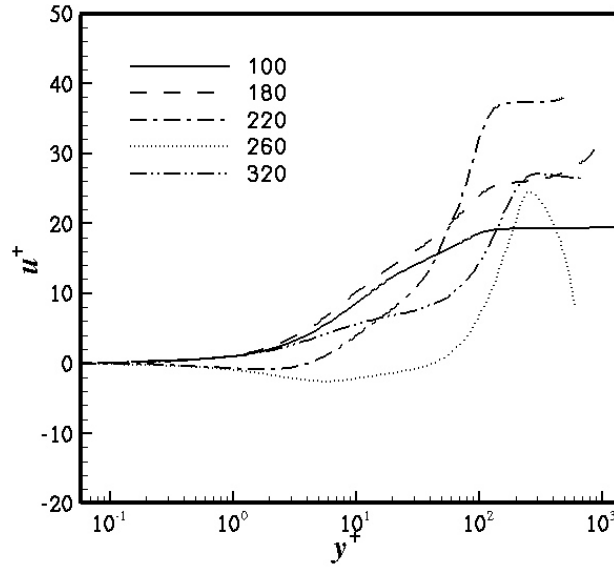


FIGURE 5.18. Contours of $\bar{u}/U_\infty = 0.4$ and $\bar{u}/U_\infty = 0.0$; — Phase 1; -.- Phase 6.

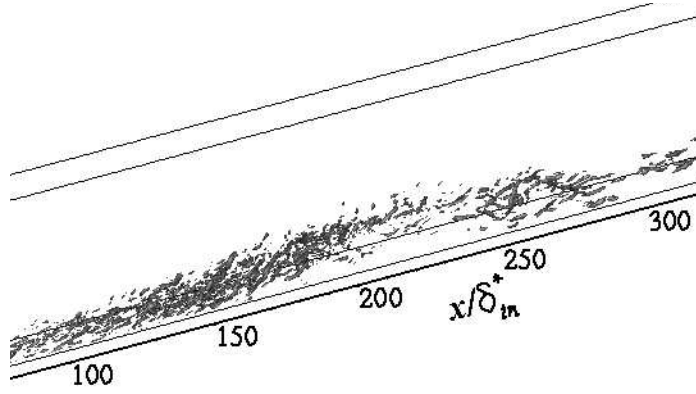


(a) Phase 5

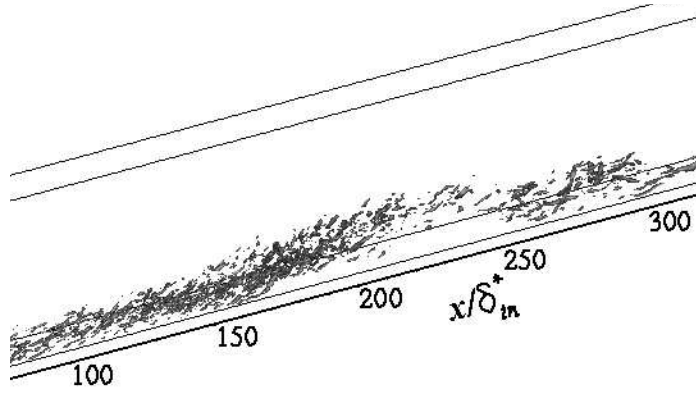


(b) Phase 9

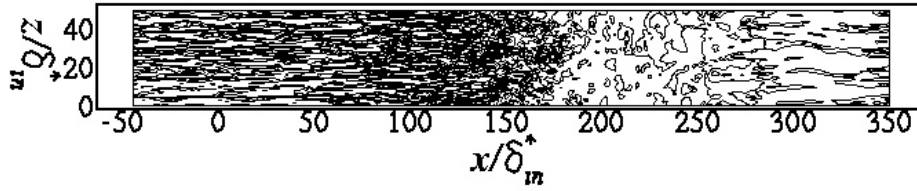
FIGURE 5.19. Mean streamwise velocity normalized with δ_{in}^* .



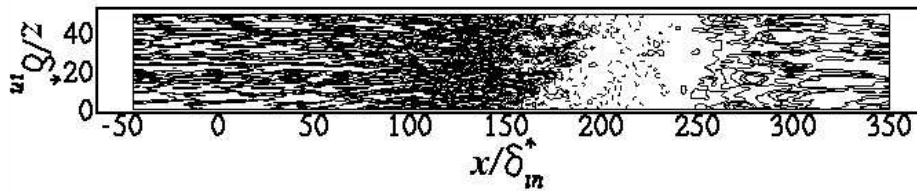
(a) Vortex field during full reattachment



(b) Vortex field during bubble development



(c) Contours of τ_{wall} during full reattachment



(d) Contours of τ_{wall} during bubble development

FIGURE 5.20. Instantaneous vortex fields defined by $\lambda_2 = -0.1$, and corresponding wall shear stress distributions.

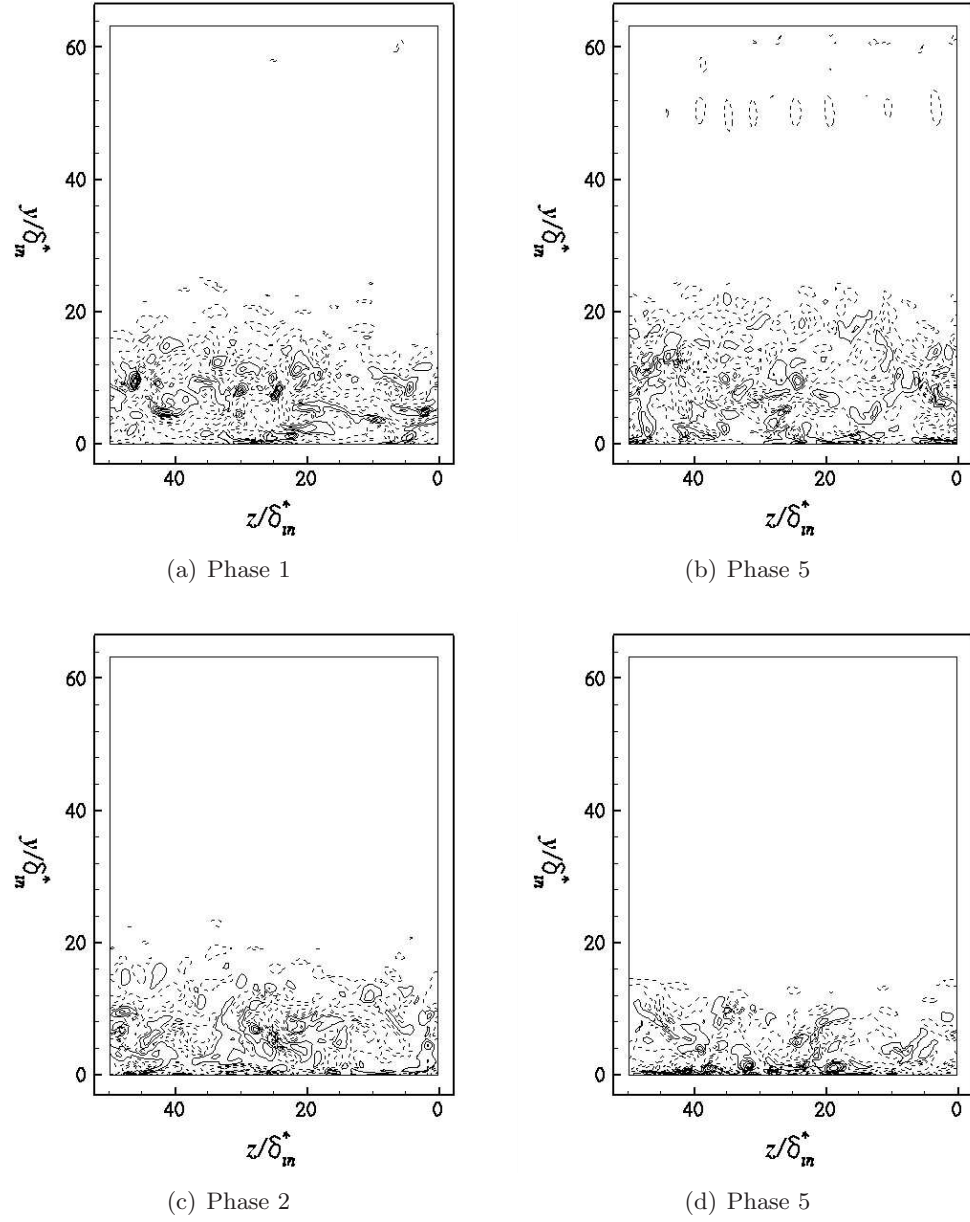
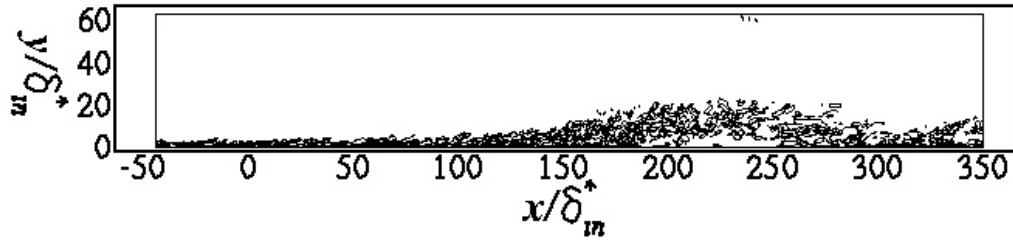
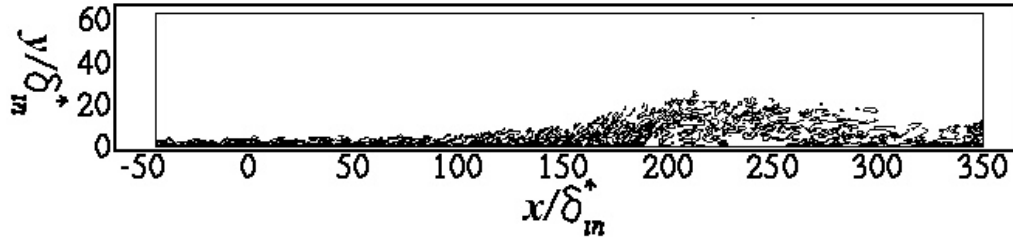


FIGURE 5.21. Instantaneous vorticity contours at $x/\delta_{in}^* = 260$ ((a) and (b)), and $x/\delta_{in}^* = 320$ ((c) and (d)).



(a) Phase 5



(b) Phase 6

FIGURE 5.22. Instantaneous vorticity distributions.

Appendix A

A fully conservative finite volume method for incompressible Navier-Stokes equations on locally refined nested Cartesian grids

A.1 Motivation and objectives

A significant portion of research in the field of computational fluid dynamics has been focused on improving solution accuracies and reducing computational costs. Despite the massive increase to our computational capacity over the last decade, the scale at which we require highly accurate large-scale simulations has grown at a significantly faster rate. Large-scale simulations today employ hundreds of billions of cells, impose significant computational costs, and require massive amounts of memory, oftentimes exceeding the capability of many mainframe computers.

One of the most common ways to lower computational costs is to lower the total number of grid points being employed throughout the domain. The unfortunate tradeoff to this approach is a significant loss in simulation fidelity. To combat this, some have employed higher-order numerical methods to improve solution accuracy while still lowering the number of computational cells (Peng *et al.*, 2003; Shiau *et al.*, 1999; Sau *et al.*, 2004). This approach has been shown to be effective when compared to low-order schemes primarily due to the cost savings associated with fewer computational cells. However, higher-order methods are oftentimes very difficult to implement on the complex grids required for practical applications. Furthermore, higher-order methods tend to have wider discretization stencils making them particularly ill-suited for simulations of physical phenomena with sharp local gradients. In such cases, the higher-order schemes effectively serve to smooth out the solution, yielding a solution that no longer accurately represents the intended physical phenomena.

A more practical alternative to higher-order methods involves effective mesh utilization.

APPENDIX A

Localizing cells in areas of interest, namely regions where high wave numbers are present, can reduce the total number of computational cells required. This approach is especially important in flow configurations with walls and obstacles, as the resolution must be significantly high near these objects to fully capture the boundary layer physics. In simple configurations, stretched grids generally allow for effective cell utilization. However, as flow configurations become more complicated, stretched grids become less effective and more time and effort is required to generate grids for specific computational configurations.

A particularly attractive local refinement methodology is the nested Cartesian grid approach (Berger & Oliger, 1984). In this case, local refinement is achieved by embedding fine Cartesian grids within coarse Cartesian grids. The attractive properties of such a scheme are that Cartesian grids are simple to create and manipulate while allowing for simple, efficient, structured algorithms to be implemented. Significant prior work has been done to develop nested Cartesian grid methodologies (Berger & Oliger, 1984; Khokhlov, 1998; Durbin & Iaccarino, 2002; Pember *et al.*, 1995; Gerritsen & Olsson, 1998). Unfortunately, one drawback to using nested Cartesian grids is that simulations are generally limited to Cartesian geometries. Significant work has been done over the last three decades to create numerical algorithms, such as immersed boundary methods, that can handle complex geometries while utilizing Cartesian meshes (Peskin, 1972; Kim *et al.*, 2001; Tseng & Ferziger, 2003). These algorithms have been combined with nested Cartesian grids to allow for simulations of complex geometries (Roma *et al.*, 1999; Ye *et al.*, 1999; Peng *et al.*, 2010; McCorquodale *et al.*, 2001).

Even though locally refined grids offer many computational benefits, numerical errors introduced at mesh refinement interfaces are still a significant concern. Over the last two decades, significant resources have been invested into developing methods to improve the solution accuracy at refinement boundaries (Almgren *et al.*, 1998; Minion, 1996; Martin & Colella, 2000; Martin *et al.*, 2008; McCorquodale *et al.*, 2001). Interpolation-based methods have become the most popular answers to this problem because they can be tuned to control the order of accuracy at mesh interfaces and they have the added benefit of allowing for efficient, fully-structured algorithms to be implemented for each individual nested block. Despite this, one of the major drawbacks regarding interpolated schemes is that they are numerically non-conservative with regards to kinetic energy.

Non-interpolated algorithms, on the other hand, allow for energy-conservative numerics to be implemented at mesh interfaces. This is done by ensuring that face-centered variables

are defined as the simple arithmetic mean between two neighboring cells' values (Mahesh *et al.*, 2004). Unfortunately, non-interpolated algorithms on nested Cartesian grids suffer from inherent mesh skewness that can adversely affect the solution accuracy. Prior work on reducing the adverse effects of mesh skewness has focused on correcting the numerical schemes themselves by introducing some sort of skewness correction factor (Mahesh *et al.*, 2004; You *et al.*, 2008b; Zwart, 2000). However, this correction factor often employs some kind of weighted interpolation that can ultimately destroys a scheme's ability to conserve energy.

This paper will introduce a new hanging node scheme designed to be fully conservative and improve on prior methods. The focus of this method is to geometrically reduce the inherent mesh skewness found in nested Cartesian grids by virtually slanting cell faces at refinement interfaces to align cell faces with the normal vector connecting neighboring cell-centers. This implementation will allow for numerics that conserve mass, momentum, and energy while retaining the benefits of an overall structured implementation.

A.2 Computational method

A.2.1 Fractional step method

The incompressible momentum and continuity equations in Cartesian coordinates are

$$\frac{\partial u_i}{\partial t} + \frac{\partial u_i u_j}{\partial x_j} = -\frac{\partial p}{\partial x_i} + \nu \frac{\partial}{\partial x_j} \frac{\partial u_i}{\partial x_j} \quad (\text{A.1})$$

and

$$\frac{\partial u_i}{\partial x_i} = 0, \quad (\text{A.2})$$

where u_i , p , and ν are the velocity, pressure, and kinematic viscosity. For incompressible flows, the density is considered constant and is absorbed into the pressure term. The primitive variables, velocity and pressure, are stored in a collocated, cell-centered arrangement, with an independent face normal velocity, $u_n = \vec{u} \cdot \vec{n}$ stored at cell faces.

Time integration of equations (A.1) and (A.2) is performed using the fractional-step

APPENDIX A

method of Kim & Moin (1985). The semi-discretized fraction-step algorithm is as follows:

$$\frac{\hat{u}_i - u_i^n}{\Delta t} = -\frac{\partial p^n}{\partial x_i} - \frac{\partial u_i u_j}{\partial x_j} + \nu \frac{\partial^2 u_i}{\partial x_j^2}, \quad (\text{A.3})$$

$$u_i^* - \hat{u}_i = \Delta t \frac{\partial p^n}{\partial x_i}, \quad (\text{A.4})$$

$$\frac{\partial^2 p^{n+1}}{\partial x_i^2} = \frac{1}{\Delta x} \frac{u_i^*}{\partial x_i}, \quad (\text{A.5})$$

$$\frac{u_i^{n+1} - u_i^*}{\Delta t} = -\frac{\partial p^{n+1}}{\partial x_i}, \quad (\text{A.6})$$

where \hat{u}_i and u_i^* are intermediate cell-center velocities and the convective and diffusive fluxes are integrated using the third-order accurate Runge-Kutta and second-order accurate Crank-Nicolson schemes, respectively. All spatial discretizations are performed using non-weighted, second-order accurate central difference scheme.

Integrating equation (A.3) over a computational cell volume, ΔV , and applying the divergence theorem yields

$$\frac{\hat{u}_i - u_i^n}{\Delta t} \Delta V = - \sum_{CS} p^n \Delta S - \sum_{CS} u_{i,face} u_n \Delta S + \sum_{CS} \frac{\Delta u_i}{\Delta x_n} \Delta S, \quad (\text{A.7})$$

where CS , ΔS , and $u_{i,face}$ denote the control surface, the surface area of a single cell face, and the interpolated velocity at the face.

A.2.2 Conservation principles

Conservation of mass, momentum, and energy is of significant importance in ensuring that numerical computations capture the physical phenomena more accurately. For compressible flows, discrete energy conservation requires that the convective and pressure terms are expressible in divergence form. The following derivation is available in the literature (Mehesh *et al.*, 2004) and is repeated here for clarity as to the implementation in the current methodology.

In a non-staggered formulation, this is complicated by the fact that the face-normal velocities stored at the face-centers are treated as independent variables in relation to the Cartesian velocities components stored at the cell centers. We can see this by looking at

the convective term for a passive scalar equation,

$$\frac{\partial \phi}{\partial t} + \frac{\partial}{\partial x_i \phi u_i} = 0. \quad (\text{A.8})$$

Integrating equation A.8 over a cell and applying the divergence theorem yields

$$V_{cv} \frac{d\phi_{cv}}{dt} + \sum_{\text{faces of } cv} \phi_{face} v_n A_f = 0, \quad (\text{A.9})$$

where ϕ_{cv} is the value of the scalar, V_{cv} is the cell volume, and A_f and v_n denote the face area and the face-normal velocity, respectively. In this case, since the incompressibility condition requires that $\frac{\partial u_i}{\partial x_i} = 0$, ϕ is conserved regardless of how ϕ_{face} is computed. However, conservation of ϕ does not imply conservation of ϕ^2 . In fact, ϕ^2 is only conserved if ϕ_{face} is computed as the simple arithmetic mean of the adjacent cell-center values,

$$\sum_{\text{volumes}} V_{cv} \frac{d\phi_{cv}^2}{dt} + \sum_{\text{boundary faces}} \phi_{face} = \frac{1}{2} (\phi_c + \phi_{nbr}). \quad (\text{A.10})$$

Multiplying equation (A.9) and substituting equation (A.10) yields the discrete equation for ϕ^2 ,

$$V_{cv} \phi_{cv} \frac{d\phi_{cv}}{dt} + \frac{\phi_{cv}}{2} \sum_{\text{faces of } cv} (\phi_{cv} + \phi_{neigh}) v_n A_f = 0, \quad (\text{A.11})$$

which can be rewritten and simplified as

$$\frac{V_{cv}}{2} \frac{d\phi_{cv}^2}{dt} + \frac{\phi_{cv}}{2} \underbrace{\sum_{\text{faces of } cv} v_n A_f}_{=0} + \frac{1}{2} \sum_{\text{faces of } cv} \phi_{cv} \phi_{neigh} v_n A_f = 0. \quad (\text{A.12})$$

Summation over all cells in the domain yields

$$\sum_{\text{volumes}} V_{cv} \frac{d\phi_{cv}^2}{dt} + \sum_{\text{volumes}} \sum_{\text{faces of } cv} \phi_{cv} \phi_{neigh} v_n A_f = 0, \quad (\text{A.13})$$

in which the contribution of all interior faces cancel out and result in

$$\sum_{\text{volumes}} V_{cv} \frac{d\phi_{cv}^2}{dt} + \sum_{\text{boundary faces}} \phi_{cv} \phi_{neigh} v_n A_f = 0. \quad (\text{A.14})$$

APPENDIX A

As long as ϕ_{neigh} is also defined according to equation (A.10), this implies that both ϕ and ϕ^2 are only influenced by the boundary conditions and are, in face, discretely conserved. In this work, discrete energy conservation is achieved by defining the interpolation for any face variable, ϕ_{face} , such that it is the simple arithmetic mean of the current cell and its neighboring cell, as expressed in equation (A.10).

A.2.3 Virtual-slanting nested Cartesian grid scheme

Local grid refinement is implemented by introducing logically nested Cartesian blocks. The benefit of this approach is that it allows for simple, computationally efficient, structured discretization schemes to be applied with a lower memory requirement compared to unstructured algorithms. Furthermore, by localizing grid refinement, computational cells can be localized in areas of interest and necessity, ultimately lowering the number of computational nodes necessary. However, these nested Cartesian grids carry with them an inherent skewness which can adversely affect the numerical accuracy of the discretization schemes that are employed. The following sections will describe a method by which cells located at refinement interfaces are virtually slanted to reduce this inherent skewness and improve both the numerical accuracy and the conservation principles of a numerical scheme. Figure A.1 shows three types of grids: a regular Cartesian grid, a non-slanted hanging node grid, and a slanted hanging node grid. These grids will be used to illustrate the differences between numerical discretizations on each grid and how a simple geometric relationships can be used to transform grid (figure A.1(b) into figure A.1(c)).

For the sake of simplicity, only two dimensions will be considered and the grid spacings in the x- and y-directions will be assumed to be the same, namely $\Delta x = \Delta y$. The grid resolution of uniform cells will be referred to as Δx , while the grid resolutions of fine and coarse cells will be referred to as Δx_f and Δx_c , respectively. Furthermore, the coarse and fine grid resolutions are assumed to differ only by a factor of two, such that $\Delta x_f = \frac{1}{2}\Delta x_c$.

Regular Cartesian grids

On two-dimensional regular Cartesian grids, as shown in figure A.1(a), the discrete volume of any given cell is easily defined as

$$\Delta V_{Cart} = \Delta x \Delta y = \Delta x^2. \quad (\text{A.15})$$

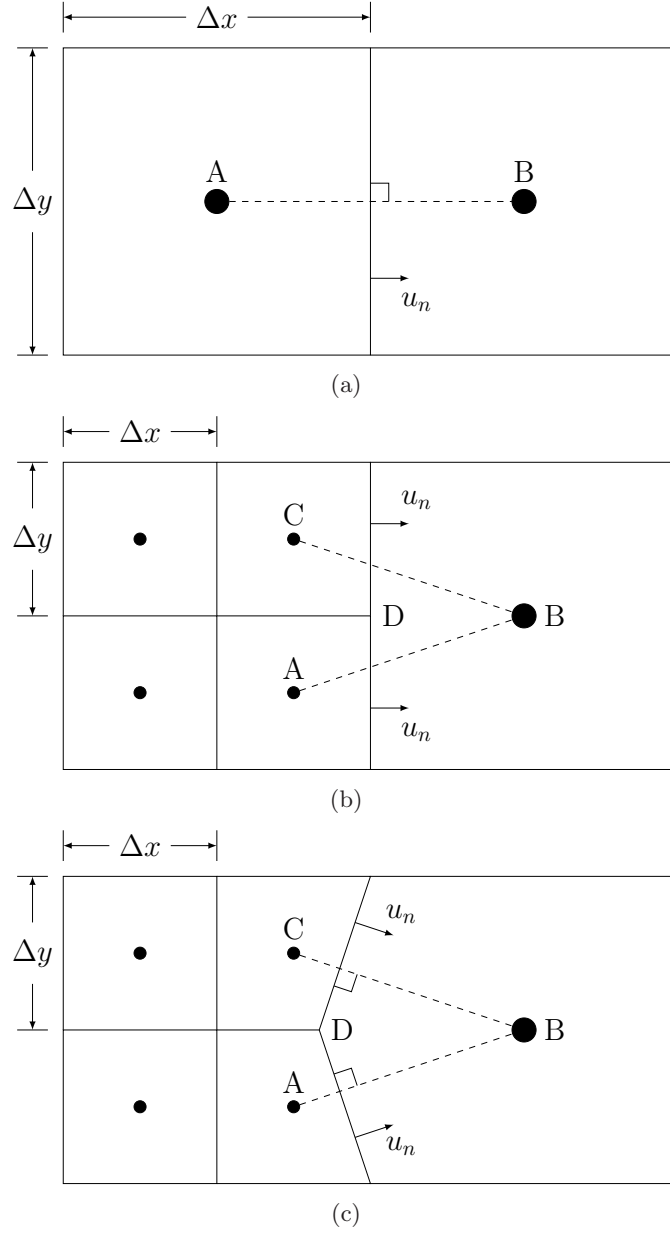


FIGURE A.1. Three example grids: (a) a regular Cartesian grid, (b) a non-slanted nested Cartesian grid, and (c) a virtually-slanted nested Cartesian grid. It can be seen that virtually-slanting mesh (b) aligns the face-normal velocities, u_n , with the vectors connecting the coarse and fine cell-centers, thus reducing the inherent skewness in the hanging-node mesh.

APPENDIX A

Furthermore, the surface area connecting any two cells, ΔS , is defined simply as

$$\Delta S_{Cart} = \Delta y = \Delta x \quad (\text{A.16})$$

and the distance between the cell-centers projected along the face-normal vector, Δx_n , is equal to the grid spacing,

$$\Delta x_{n, Cart} = \Delta x. \quad (\text{A.17})$$

Non-slanted nested Cartesian grids

For the nested Cartesian grids, we will focus only on the cells adjacent to a refinement interface, as all other cells are covered under the regular Cartesian grid discretizations. Furthermore, the non-slanted methodology described here does not employ interpolation to fill the hanging node values. Instead, cells at mesh interfaces are evaluated directly, much like they would be in unstructured implementations. This means that one extra face must be evaluated for coarse cells, while the number of operations for all other cells.

On non-slanted nested Cartesian grids, figure A.1(b), we can see that the coarse and fine cell volumes are easily computed as

$$\Delta V_{f, NS} = \Delta x_f \Delta y_f = \Delta x_f^2 \quad (\text{A.18})$$

and

$$\Delta V_{c, NS} = \Delta x_c \Delta y_c = \Delta x_c^2, \quad (\text{A.19})$$

just as they are on the regular Cartesian grids. However, the surface area connecting any two cells across a refinement interface is now defined by the fine resolution,

$$\Delta S_{NS} = \Delta y_f = \Delta x_f = \frac{1}{2} \Delta x_c. \quad (\text{A.20})$$

Furthermore, since the cell-centers are now farther apart, the face-normal distance between the cells becomes

$$\Delta x_{n, NS} = \frac{3}{2} \Delta x_f = \frac{3}{4} \Delta x_c. \quad (\text{A.21})$$

We can easily observe that this length is not computed along the vector connecting the two cell-centers, introducing a skewness in the mesh that can adversely affect the numerical accuracy of the discretization schemes.

Virtually-slanted nested Cartesian grids

To reduce the inherent skewness at refinement interfaces, the faces can be virtually-slanted to align their normal vector to the vector connecting the fine and coarse cell-centers, as shown in figure A.1(c). The amount a surface needs to be slanted is simply a function of the cell's geometry. In the case where $\Delta x = \Delta y$, the appropriate virtual-slanting requires that node D be shifted $\frac{1}{3}\Delta x_f$ away from the coarse cell-center. The new fine and coarse cell volumes become

$$\Delta V_{f,SL} = \Delta x_f \Delta y_f - \frac{1}{6} \Delta x_f \Delta y_f = \frac{5}{6} \Delta x_f^2 \quad (\text{A.22})$$

and

$$\Delta V_{c,SL} = \frac{7}{6} \Delta x_c \Delta y_c = \frac{7}{6} \Delta x_c^2, \quad (\text{A.23})$$

respectively. Furthermore, both the surface area and face-normal distance between cells change such that

$$\Delta S_{SL} = \sqrt{\left(\frac{1}{3} \Delta x_f\right)^2 + (\Delta y_f)^2} = \frac{\sqrt{10}}{3} \Delta x_f = \frac{\sqrt{10}}{6} \Delta x_c, \quad (\text{A.24})$$

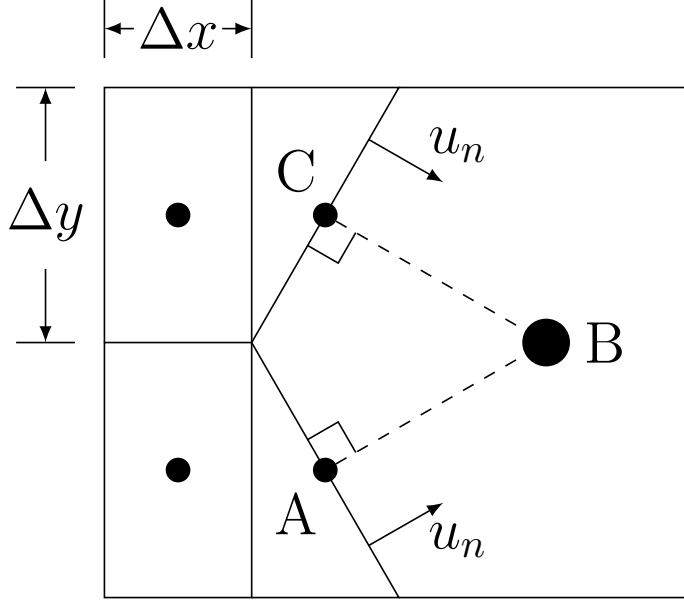
and

$$\Delta x_{n,SL} = \sqrt{\left(\frac{3}{2} \Delta x_f\right)^2 + \left(\frac{1}{2} \Delta y_f\right)^2} = \frac{\sqrt{10}}{2} \Delta x_f = \frac{\sqrt{10}}{4} \Delta x_c. \quad (\text{A.25})$$

Aside from modifying the geometry of faces along a refinement interface, it can be seen in figure A.1(c) that the virtually-slanting scheme also modifies the surface shared by cells A and C. The regular Cartesian surface area of Δx_f between cells A and C now becomes

$$\Delta S_{AC} = \Delta x_f - \Delta x_{shift} = \Delta x - \frac{1}{3} \Delta x = \frac{2}{3} \Delta x. \quad (\text{A.26})$$

Again, this is a simple change in the geometric coefficients for these cells. Coarse cells are

FIGURE A.2. Virtual-slanting in the case where $\Delta y/\Delta x = \sqrt{3}$.

not affected by this as the shift only occurs within the fine cell block.

Comparing equations (A.18) - (A.24), we see that the only difference between the non-slanted and virtually-slanted scheme is a simple modification of the geometric coefficients. Furthermore, the virtual-slanting scheme does not introduce any additional neighbor connectivity. Therefore, the same matrix solvers used for the non-slanted approach can be used for the slanted scheme without increasing the computational cost.

A.2.4 Virtual slanting limitation

The amount of virtual slanting necessary to align a face to the normal vector connecting the cell-centers varies according to the cell geometry. Cells with a high aspect ratio will require more slanting. However, if the aspect ratio is too high, it will not be possible to slant a face appropriately without propagating mesh skewness into the nested Cartesian blocks or without creating additional cell connectivity. Figure A.2 shows a case in which a face is slanted to the point of creating triangular fine cells. It can be seen that slanting the faces any further will affect the fine cells located on the interior of a nested Cartesian block.

One can avoid creating such complicated geometries by limiting the extent to which faces are virtually slanted. Assuming the coarse and fine resolutions differ by a factor of

two, this geometric limitation is defined by

$$\frac{\Delta x_j}{\Delta x_i} \leq \sqrt{3} \quad (\text{A.27})$$

for any given direction i . The slant angle could be fixed such that for all directions i where $\Delta x_j/\Delta x_i > \sqrt{3}$, the face may only slant to the point where $\Delta x_j/\Delta x_i = \sqrt{3}$. While this avoids the creation of complicated geometries, the slanted face would no longer be aligned to the normal vector connecting the coarse and fine cell-centers and the overall effectiveness of this scheme will be lessened. However, even partial virtual-slanting should serve to reduce the skewness inherent in nested Cartesian and improve the mesh quality.

A.2.5 Extension to three-dimensional configurations

In the case of three dimensions, slanting the fine cell faces such that they are aligned to the normal vector connecting the cell-centers generates new cell connectivity. Figure A.3(a) shows a diagram of the mesh topology resulting from three-dimensional mesh slanting. The shaded regions in figures A.3(a) and A.3(c) highlight the new faces generated in the case of three-dimensional slanting. This additional connectivity increases matrix sparseness and increasing the overall computational cost of the simulation. Moreover, these new faces would also require their own slanting in order to align them with the normal vector connecting diagonal cell-centers, increasing the implementation complexity even further.

In order to avoid these complications, an approximated slanting is introduced in the case of three dimensions. Rather than virtually slanting each face to perfectly align it to the normal vector connecting the cell-centers, only the node at which the four fine cells meet is shifted. This creates two sub-faces on each fine cell, each of which is perfectly aligned to one of the two components of the normal vector connecting the two cell-centers. The dashed lines in figure A.3(b) illustrate where the two sub-faces meet on each fine cell. It is interesting to note that the creation of these sub-faces does not add to the computational cost of the algorithm as each sub face does not need to be evaluated separately for every time step. The reason for this is because each discretized evaluation calls only for the projection of the face area onto the normal direction under consideration. Since no two sub-faces overlap, the projected face area for each face is simply the summation of the projected areas of each sub-face onto the normal direction being considered.

APPENDIX A

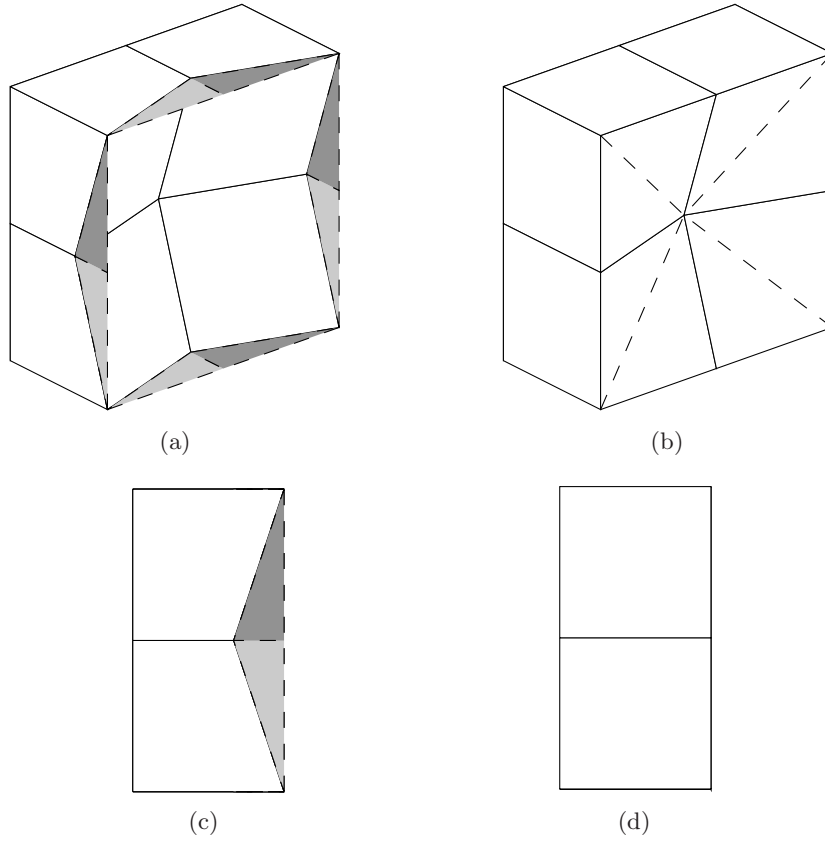


FIGURE A.3. Isometric views of the fine cells at a refinement interface are shown above for the (a) fully-slanted and (b) approximated slanting configurations. A side view of each each method is also shown in (c) and (d), respectfully, for clarity. The alternating shaded regions in (a) and (c) are used to show the new faces generated between edge cells when the fully-slanted approach is employed. These new faces expose the coarse cell to diagonal cells, requiring additional connectivity information and increasing the computational cost of the simulation. (c) and (d) clearly illustrate that no new faces are introduced in the approximated slanting approach.

A.3 Verification and validation

A.3.1 Unsteady convection-diffusion of a Gaussian pulse

Unsteady convection-diffusion of a Gaussian pulse is evaluated to verify the accuracy of the present virtual-slanting scheme. The computational domain is defined on $[0, 2]^2$ with the analytical solution to the problem being

$$\phi(x, y, t) = \frac{1}{4t + 1} \exp \left(-\frac{(x - ut - 0.5)^2}{\nu(4t + 1)} - \frac{(y - vt - 0.5)^2}{\nu(4t + 1)} \right). \quad (\text{A.28})$$

The analytical solution is used to both initialize the field at $t = 0$ and apply Dirichlet boundary conditions at the edges of the domain. Cell Reynolds numbers of 2 and 200 are considered by imposing a fixed viscosity of $\nu = 0.01$ and setting convection velocities of $u = v = 0.8$ and $u = v = 80$, respectively.

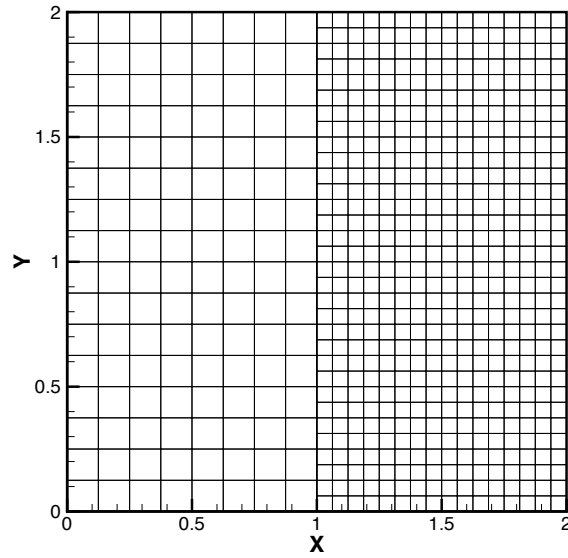
The computational mesh is composed of two different refinement levels, as shown in figure A.4(a). The left half of the mesh is the coarse grid with a resolution of Δx_c , while the right half of the mesh is the fine grid with a resolution of $\Delta x_f = \frac{1}{2}\Delta x_c$. Only the resolution in the x-direction will be discussed, as $\Delta x = \Delta y$ is assumed for all results in this paper.

Figure A.4(b) shows that the Gaussian pulse passes through the mesh refinement interface without numerical artifacts. Figure A.5 shows L_2 -norm errors with respect to the exact solution for the present method at $Re = 2$ and $Re = 200$ and various levels of grid refinement. Grid convergence tests were performed with a fixed time-step size of $\Delta t = 2.5 \times 10^{-4}$ for $Re = 2$ and $\Delta t = 2.5 \times 10^{-5}$ for $Re = 200$. The present method is found to be globally second-order accurate in both cases.

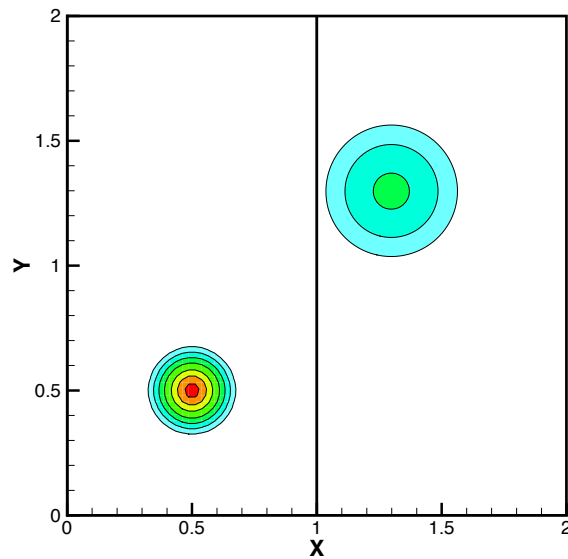
A.3.2 2D Taylor-Green vortex

Two-dimensional Taylor-Green vortices are simulated to both identify the present method's accuracy when solving the incompressible Navier-Stokes equations and verify its energy conserving properties. The computations are performed on a $[-1, 1]^2$ computational domain

APPENDIX A

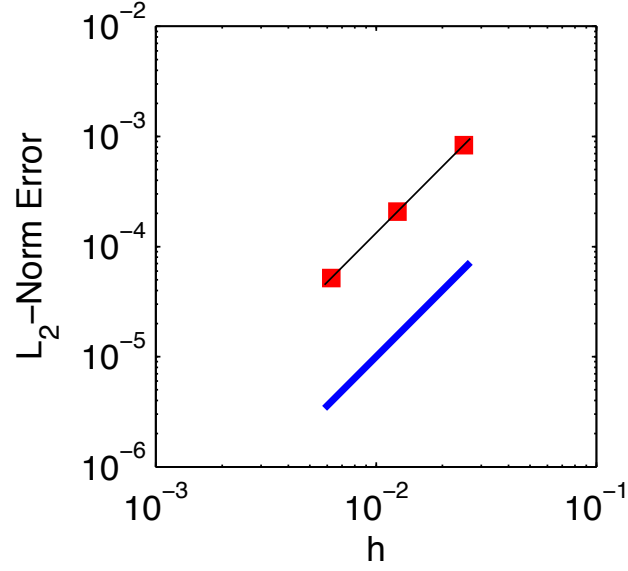


(a)

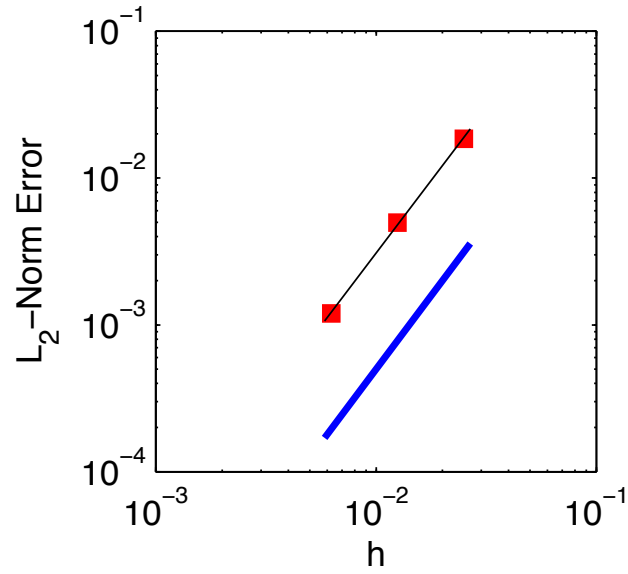


(b)

FIGURE A.4. Diagrams of (a) the computational mesh layout employing two levels of refinement and (b) the contours of the convected Gaussian pulse from left to right (at $t = 0$ and $t = 1.0$, respectively) for $Re = 2$. The thick black line along the centerline of (b) denotes the refinement interface.



(a)



(b)

FIGURE A.5. The above plot shows the L_2 -norm errors as a function of grid spacing for (a) $Re = 2$ and (b) $Re = 200$. Both plots show that the virtually-slanting scheme is globally second-order accurate.

APPENDIX A

with the following analytical solutions for velocity and pressure:

$$u = -\cos(\pi x) \sin(\pi y) e^{-2\pi^2 t/Re}, \quad (\text{A.29})$$

$$v = \sin(\pi x) \cos(\pi y) e^{-2\pi^2 t/Re}, \quad (\text{A.30})$$

$$p = -\frac{1}{4}[\cos(2\pi x) + \cos(2\pi y)] e^{-4\pi^2 t/Re}. \quad (\text{A.31})$$

The field is initialized using the analytical solutions at $t = 0$ with periodic boundary conditions imposed in all directions.

The computation mesh is composed of quadrants of alternating levels of refinement, as shown in figure A.6(a). This arrangement ensures that each quadrant is surrounded by a refinement interface, even across periodic boundaries.

Grid convergence tests are performed at $Re = 100$, where the Reynolds number is defined as $Re = U_m L / \nu$ with U_m being the initial maximum velocity and L being the vortex length. A fixed time step of $\Delta t = 0.001$ is used to ensure that $CFL < 1$ for all cases.

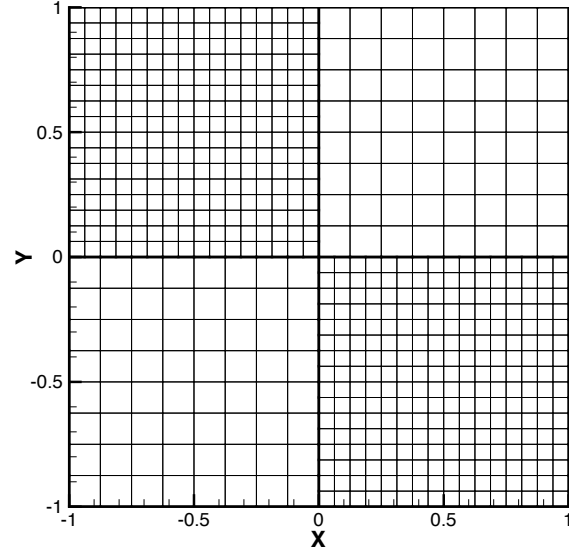
Figure A.7 shows L^2 -norm errors for various levels of grid refinement. Again, the present method is found to be globally second-order accurate for both velocity and pressure.

Figure A.8 shows the time history of kinetic energy for the non-slanted and virtually-slanted schemes. The kinetic energy is evaluated to serve as an indication of a method's ability to conserve energy. It can easily be seen that the virtually-slanted scheme shows improved kinetic energy conservation properties compared to the non-slanted scheme.

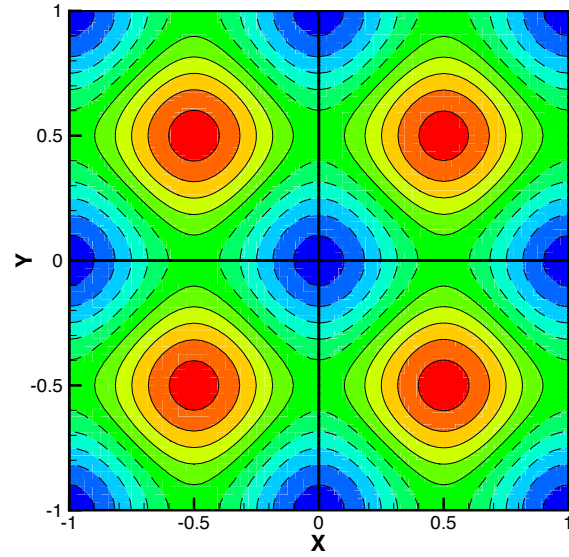
A.3.3 Flow in a lid-driven cavity

Flow in a lid-driven cavity is used to evaluate the virtually-slanted scheme's ability to predict steady-state solutions. The computational flow configuration is shown in figure A.9(a). Coarse grid spacing of $\Delta x_c = \Delta y_c = 0.0125$ is used in the center of the domain with local refinement embedded near the walls using $\Delta x_f = \Delta y_f = \frac{1}{2}\Delta x_c = 6.25 \times 10^{-3}$.

The computations were carried out at a Reynolds number of $Re = 1000$, where the Reynolds number is defined as $Re = U_{lid} L / \nu$, where U_{lid} is the speed of the top lid and L is the length of each side of the square cavity. Contours for the steady-state solution for the lid-driven cavity are shown in figure A.9(b) and centerline velocity profiles of u and v are shown in figure A.10. The centerline velocity profiles show good agreement with the results obtained using a uniform mesh with resolution $\Delta x = \Delta x_f = 6.25 \times 10^{-3}$. These results demonstrate that the present method is able to achieve comparable results to uniform



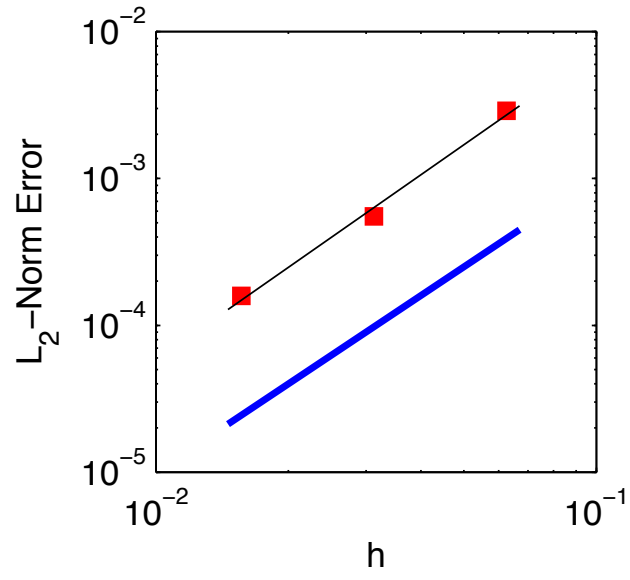
(a)



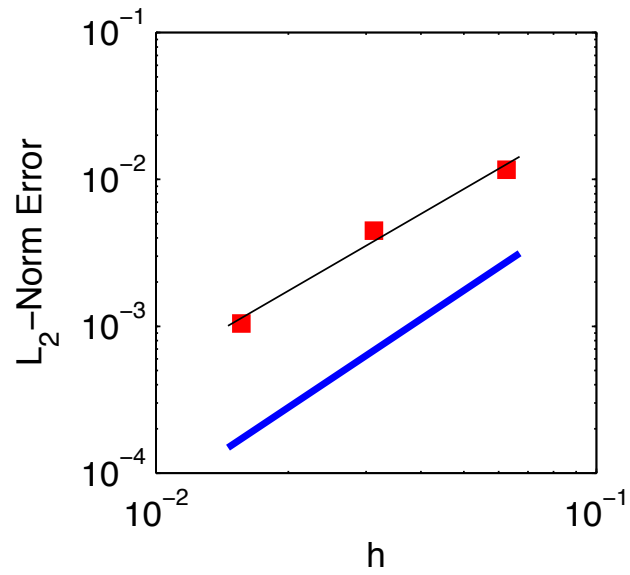
(b)

FIGURE A.6. Diagrams of (a) the computation mesh layout used to simulate two-dimensional Taylor-Green vortices and (b) the pressure contours of the initial field. The thick black lines in (b) illustrate the refinement interfaces.

APPENDIX A



(a)



(b)

FIGURE A.7. The above plots show that the virtually-slanted scheme is globally second-order accurate for both (a) velocity and (b) pressure at $Re = 100$.

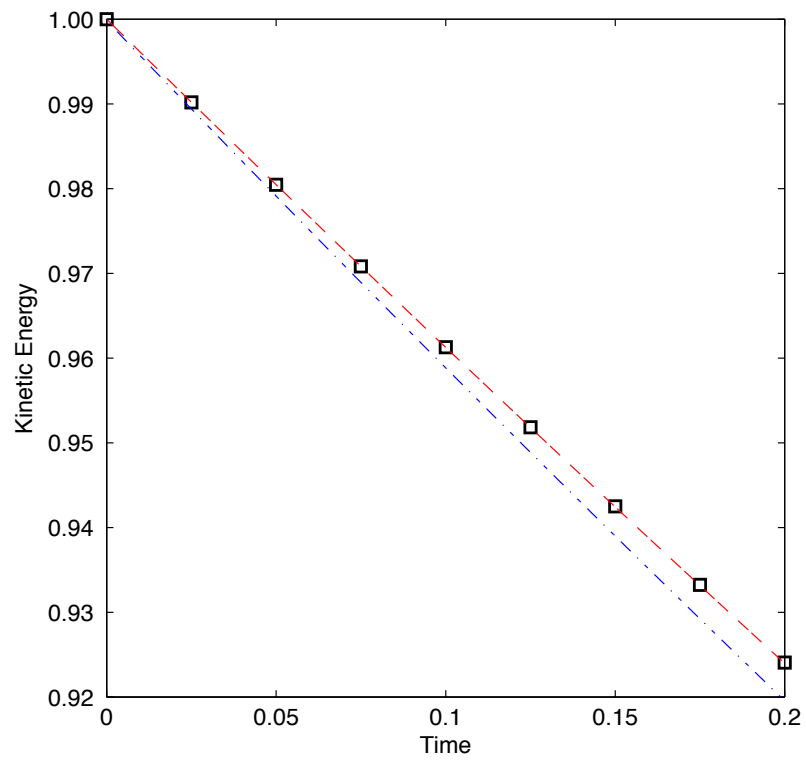
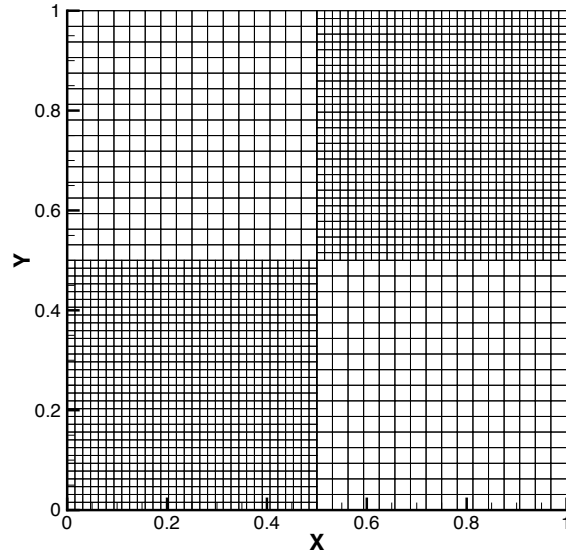
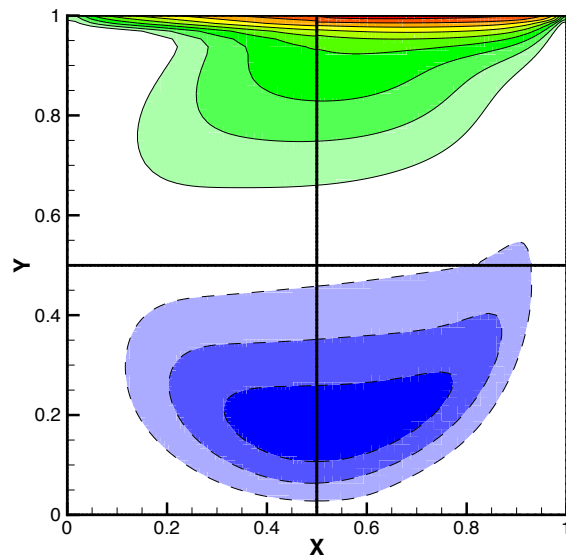


FIGURE A.8. The kinetic energy time-history shows that the virtually-slanting scheme conserves energy better than the standard non-slanted hanging node scheme.

APPENDIX A



(a)



(b)

FIGURE A.9. The above plots illustrate the (a) computational grid employed and (b) the u -velocity contours for the steady-state solution at $Re = 1000$.

meshes while utilizing fewer computational cells.

A.3.4 Flow over a square cylinder

Flow over a square-cylinder is used to validate the present scheme’s ability to predict unsteady flow phenomena. The computational domain is defined on $[0, 51D]^2$, where D is the square-cylinder diameter, and is shown in figure A.11. The cylinder is located in the center of the computational domain, ensuring that there is adequate distance from both the inlet and the far-field boundaries. A Dirichlet boundary condition of $u = U$ and $v = 0$ is imposed at the inlet, where U is the free stream velocity. Free-slip boundary conditions are imposed at the far-field boundaries and a Neumann boundary condition is set at the outflow boundary.

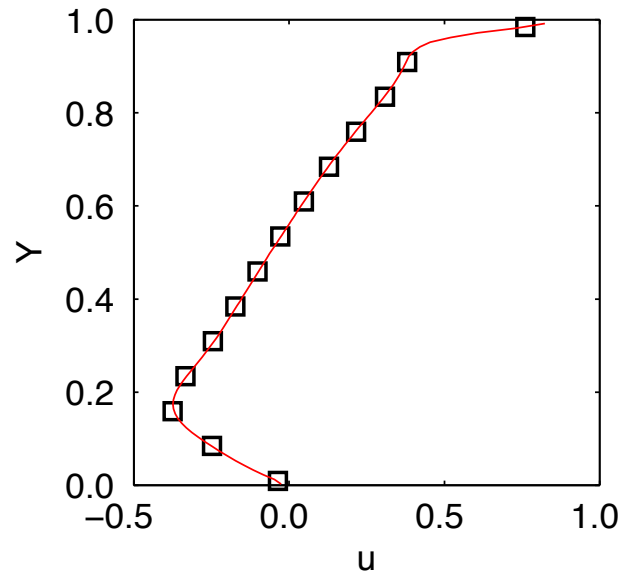
Five distinct levels of local refinement were implemented, as shown in figure A.11. Again, each level of refinement is a factor of two different from it’s neighboring level, with the smallest grid size being $\Delta x_f = 7.8125 \times 10^{-3}$ near the wall.

The computations were carried out at $Re = 100$ using a time-step size determined by the $CFL = 1$ criterion. Figure A.12 shows contours of the instantaneous vorticity, while figure A.13 shows the variation of the lift force as a function of time. Table A.1 shows the resulting mean drag, RMS lift, and Strouhal number (St) for the present scheme, as well as from a variety of literature results. The present method shows good agreement with data from the literature for the Strouhal number and RMS lift. The mean drag appears to be under predicted, but further studies are being performed to determine whether this is an issue of grid resolution or a limitation of the virtually-slanted scheme.

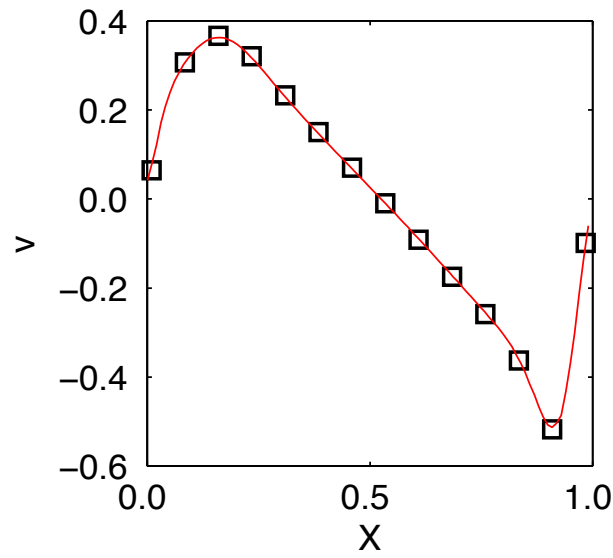
	St	Mean Drag	RMS Lift
Virtual-Slanting Scheme	0.144	1.36	0.16
Chung & S.-H.Kang (2000)	0.141	1.46	0.20
Franke <i>et al.</i> (1990)	0.154	1.61	0.27
Sohankar <i>et al.</i> (1997)	0.146	1.48	0.16
Robichaux <i>et al.</i> (1999)	0.154	1.53	—
Okajima (1965)	0.14	1.45	—
Sohankar <i>et al.</i> (1997)	0.143	—	—

Table A.1. Computational results for the Strouhal number (St), mean drag, and RMS lift at $Re = 100$ for the virtually-slanting scheme, as well as several results from the literature.

APPENDIX A

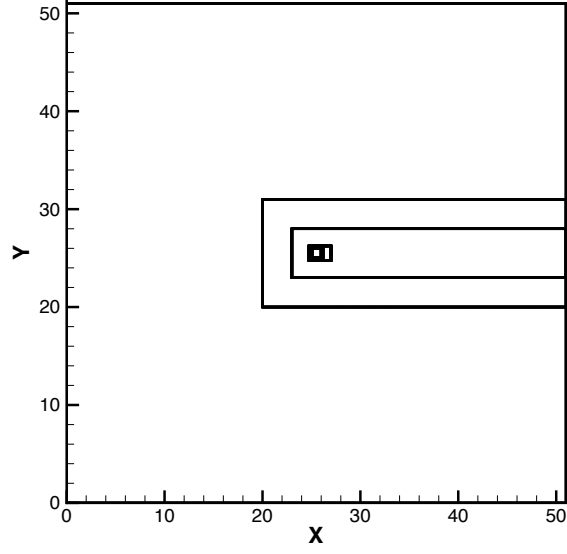


(a)

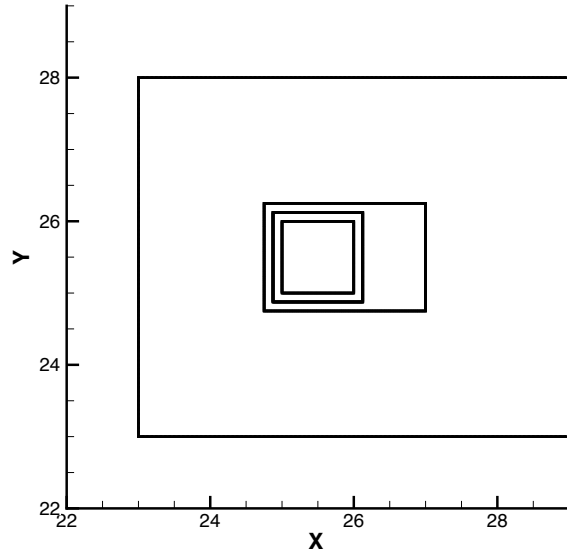


(b)

FIGURE A.10. Good agreement can be seen between the virtually-slanting scheme and the uniform mesh results for the centerline velocities of both (a) u and (b) v . The uniform mesh resolution was set according to the finest resolution in the locally refined case, $\Delta x = \Delta x_f = 6.25 \times 10^{-3}$.



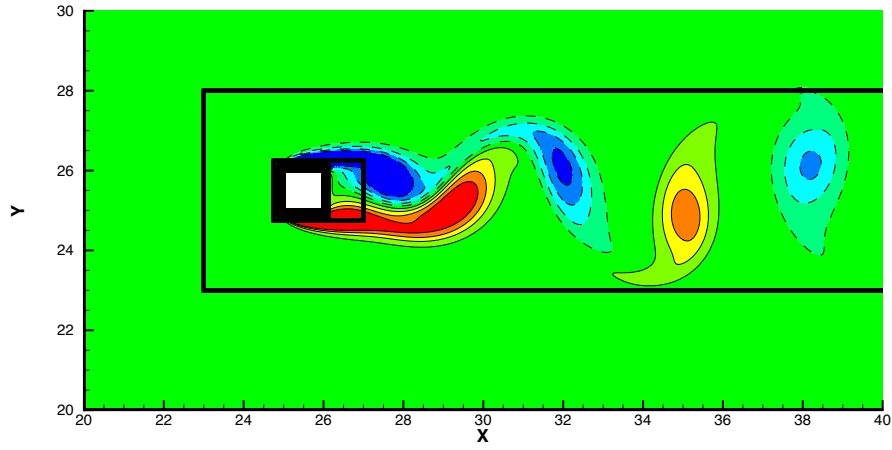
(a)



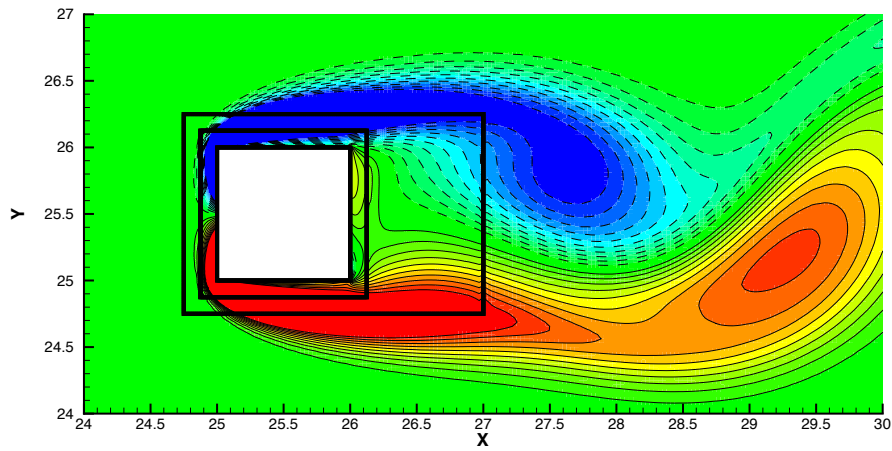
(b)

FIGURE A.11. The overall computational configuration is shown above in (a), with a closer look at the refinement interfaces around the square-cylinder shown in (b). Five distinct levels of refinement are shown, with the highest resolution of $\Delta x_f = 7.8125 \times 10^{-3}$ located at the cylinder wall.

APPENDIX A



(a)



(b)

FIGURE A.12. Contours for the instantaneous z -vorticity are shown in (a), with a closer look at the contours around the square-cylinder presented in (b).

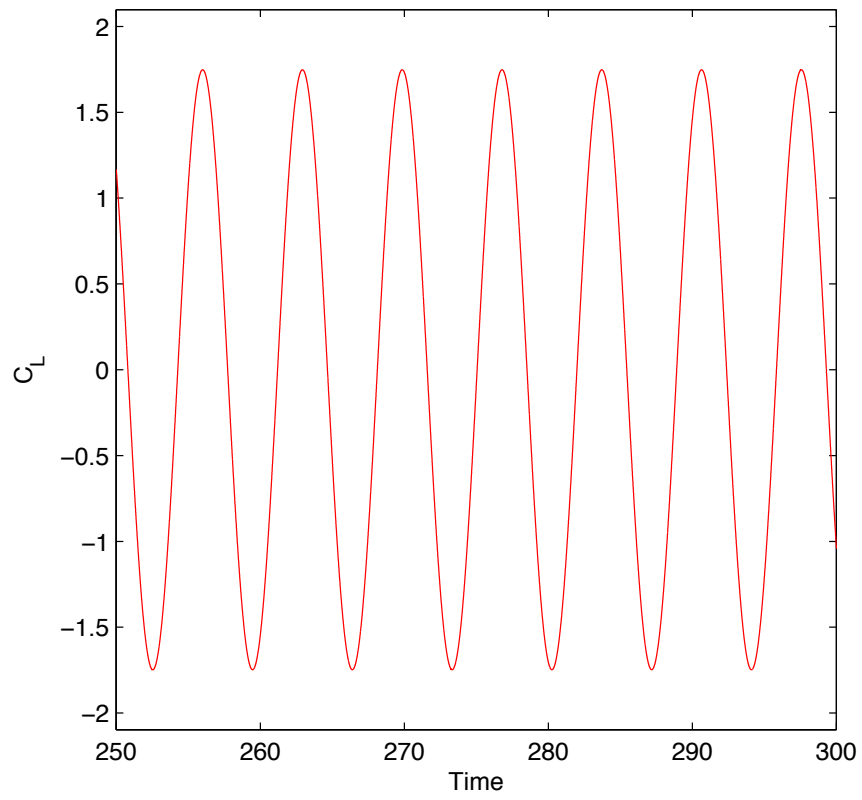


FIGURE A.13. The above plot shows the smooth variation in the coefficient of lift (C_L) as a function of time.

A.3.5 3D Taylor-Green vortex

The virtually-slanting scheme was further tested using the three-dimensional Taylor-Green vortex case shown by Shu *et al.* (2005). This computational configuration is known to undergo a kinetic energy cascade, whereby the kinetic energy in the system drops very rapidly. The length of time required for this kinetic energy cascade to take place is a strong indicator of the amount of numerical and viscous dissipation in a discretization scheme, where a longer time-delay indicates a lower level of dissipation.

Much like its two-dimensional counterpart, the computational mesh for the three-dimensional Taylor-Green vortex case is composed of octants of alternating levels of refinement and is shown in figure A.14(a). Again, this arrangement ensures that each octant is surrounded by a refinement interface, even across periodic boundaries.

The computational domain is defined on $[0, 2\pi]^3$ with periodic boundary conditions imposed in all directions. The flow field is initialized at time $t = 0$ using

$$u(x, y, z) = \sin(kx) \cos(ky) \cos(kz), \quad (\text{A.32})$$

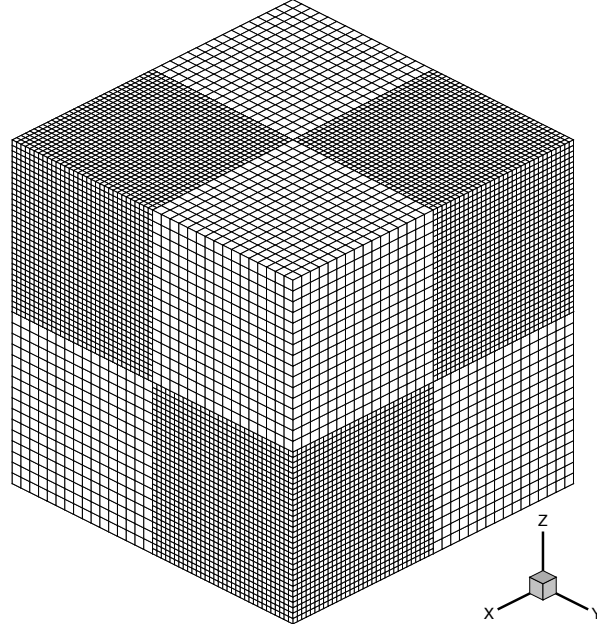
$$v(x, y, z) = -\cos(kx) \sin(ky) \cos(kz), \quad (\text{A.33})$$

$$w(x, y, z) = 0, \quad (\text{A.34})$$

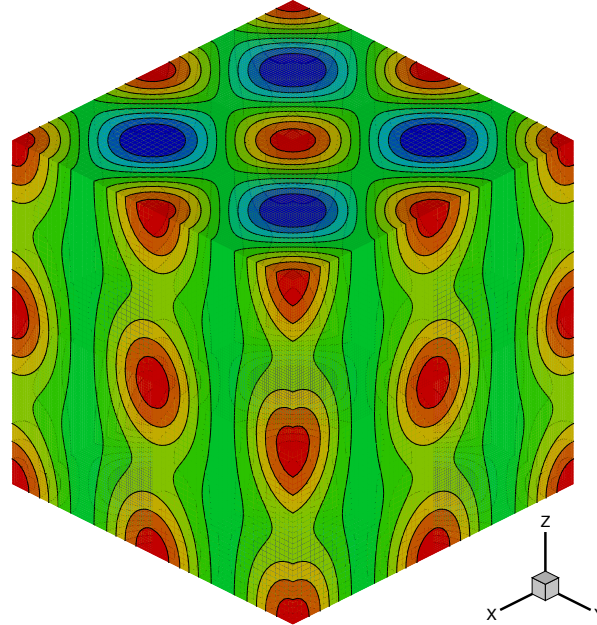
$$p(x, y, z) = \frac{1}{16} [(\cos(2z) + 2)(\cos(2x) + \cos(2y)) - 2], \quad (\text{A.35})$$

where the wavenumber $k = 2\pi/\lambda = 1$. Even though the initial conditions impose a two-dimensional flow field, the existence of a pressure gradient in the z -direction (shown in figure A.14(b)) forces the creation of three-dimensional flow for time $t > 0$.

The energy cascade described previously is purely a numerical phenomena, therefore a uniform mesh case is being used as a standard for comparison. Figure A.15 shows the the time-history of kinetic energy for a uniform mesh case, the virtually-slanted scheme, and an interpolated scheme. The virtually-slanted scheme shows good agreement with the results from the uniform mesh case, both of which appear to initiate a kinetic energy cascade at very similar points in time. Conversely, the interpolated scheme begins rapidly losing energy much sooner than either of the previous cases, indicating that it suffers more strongly from numerical and viscous dissipation. These results strongly suggest that the virtually-slanted scheme is able to be applied to three-dimensional flows, conserve energy quite well, and produce results comparable to those found on uniformly refined meshes.



(a)



(b)

FIGURE A.14. The above diagrams depict (a) the computation mesh used to simulate three-dimensional Taylor-Green vortices and (b) contours of the initial pressure field.

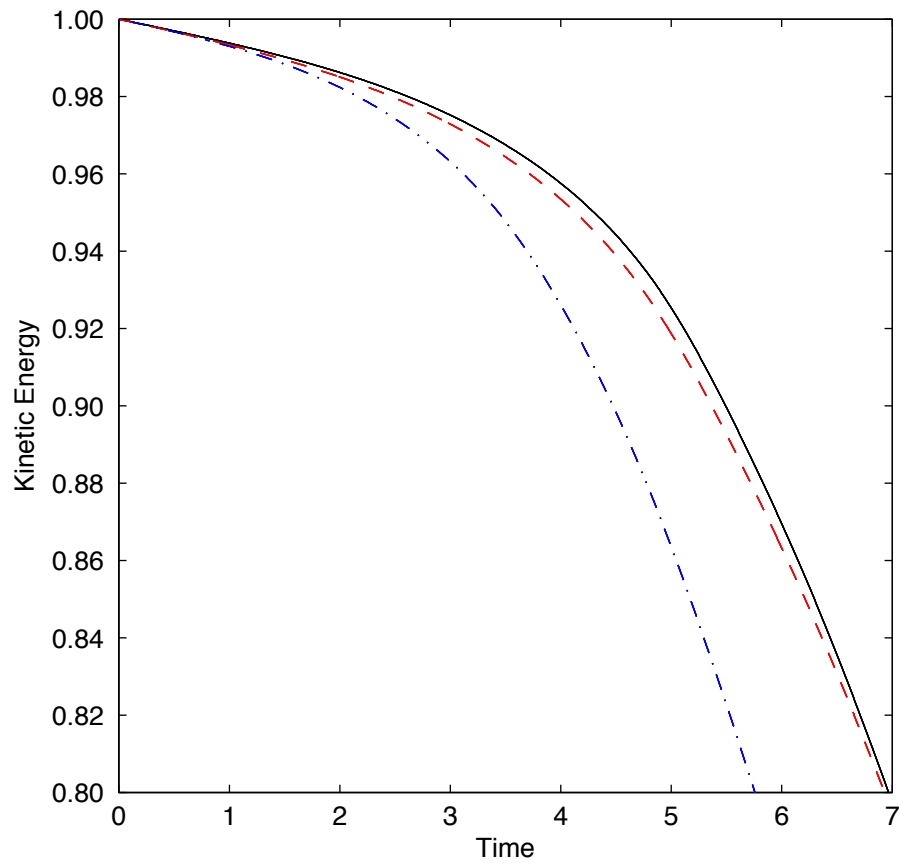


FIGURE A.15. The above plot shows the time-history of the kinetic energy for three-dimensional Taylor-Green vortices. The virtually-slanted (--- red line) scheme shows good agreement with the uniform results (— black line), while the kinetic energy cascade begins much sooner for the interpolated scheme (-·- blue line).

A.4 Summary

A second-order-accurate finite-volume method for kinetic energy conserving simulations of incompressible flows on hanging node meshes has been developed. The order of accuracy was verified to be globally second order on both the unsteady convection-diffusion equations and the incompressible Navier-Stokes equations. The present scheme showed good prediction of both steady and unsteady flow phenomena using lid-driven cavity and flow over a square cylinder, respectively. Improved energy conservation was demonstrated using decaying Taylor-Green vortices in both two and three dimensions. The virtually-slanted method showed good agreement with uniform mesh results in the case of a lid-driven cavity, and good agreement with literature data in the case of flow over a square cylinder.

References

- AGARWAL, N. K. & SIMPSON, R. L. 1990 Backflow structure of steady and unsteady separating turbulent boundary layers. *AIAA Journal* **28** (10), 1764–1771.
- ALMGREN, A., BELL, J., COLELLA, P., HOWELL, L. & WELCOME, M. 1998 A conservative adaptive projection method for the variable density incompressible navierstokes equations. *Journal of Computational Physics* **142**, 1–46.
- BERGER, M. & OLIGER, J. 1984 Adaptive mesh refinement for hyperbolic partial differential equations. *Journal of Computational Physics* **53**, 484–512.
- CARR, L. W., CHANDRASEKHARA, M. S. & BROCK, N. J. 1991 A quantitative study of unsteady compressible flow on an oscillating airfoil. *AIAA Paper 1991-1683*.
- CARR, L. W. & MCCROSKEY, W. J. 1992 A review of recent advances in computational and experimental analysis of dynamic stall. In *International Union of Theoretical and Applied Mechanics Symposium on Fluid Dynamics of High Angle of Attack*. Tokyo, Japan.
- CHANDRASHEKHARA, M. & CARR, L. W. 1989 Flow visualization of the Mach number effects on the dynamic stall of an oscillating airfoil. *AIAA Paper 89-0023*.
- CHOUDHURI, P. G., KNIGHT, D. D. & VISBAL, M. R. 1994 Two-dimensional unsteady leading-edge separation on a pitching airfoil. *AIAA Journal* **32** (4), 673–681.
- CHUNG, Y. & S.-H.KANG 2000 Laminar vortex shedding from a trapezoidal cylinder with different heigh ratios. *Physics of Fluids* **12**, 1251–1254.
- COLEMAN, G. N. & SPALART, P. R. 1993 Direct numerical simulation of a small separation bubble. In *Near-Wall Turbulence Flows* (ed. C. G. Speziale & B. E. Launder), pp. 277–286. Elsevier.
- CURRIER, J. M. & FUNG, K.-Y. 1992 Analysis of the onset of dynamic stall. *AIAA Journal* **30** (10), 2469–2477.
- DURBIN, P. & IACCARINO, G. 2002 An approach to local refinement of structured grids. *Journal of Computational Physics* **181**, 639–653.

- EKATERINARIS, J. A. & PLATZER, M. F. 1997 Computational predictions of airfoil dynamic stall. *Progress in Aerospace Sciences* **33**, 759–846.
- FANG, Y. & MENON, S. 2006 Kinetic-eddy simulation of static and dynamic stall. *AIAA Paper 2006-3847*.
- FRANKE, R., RODI, W. & SCHONUNG, B. 1990 Numerical calculation of laminar vortex shedding flow past cylinders. *Journal of Wind Engineering & Industrial Aerodynamics* **35**, 237.
- GERMANO, M., PIOMELLI, U., MOIN, P. & CABOT, W. H. 1991 A dynamic subgrid-scale eddy-viscosity model. *Physics of Fluids (A)* **3** (7), 1760–1765.
- GERRITSEN, M. & OLSSON, P. 1998 Design and efficient solution strategy for fluid flows ii. stable high-order central finite difference schemes on composite adaptive grids with sharp shock resolution. *Journal of Computational Physics* **147**, 293–317.
- GHIAS, R., MITTAL, R., DONG, H. & LUND, T. S. 2004 Large-eddy simulation of the tip flow of a rotor in hover. *AIAA Paper 2004-2432*.
- GHIAS, R., MITTAL, R., DONG, H. & LUND, T. S. 2005 Study of tip-vortex formation using large-eddy simulation. *AIAA Paper 2005-1280*.
- GILARRANZ, J. L., TRAUB, L. W. & REDINIOTIS, O. K. 2005 A new class of synthetic jet actuators - part II: application to flow separation control. *Journal of Fluids Engineering* **127**, 377–387.
- JEONG, J. & HUSSAIN, F. 1995 On the identification of a vortex. *Journal of Fluid Mechanics* **285**, 69–94.
- JUMPER, E. J., SCHRECK, S. J. & DIMMICK, R. L. 1987 Lift-curve characteristics for an airfoil pitching at constant rate. *Journal of Aircraft* **24** (10), 680–687.
- KHOKHLOV, A. 1998 Fully threaded tree algorithms for adaptive refinement fluid dynamics simulations. *Journal of Computational Physics* **143**, 519–543.
- KIM, J., KIM, D. & CHOI, H. 2001 An immersed-boundary finite-volume method for simulations of flow in complex geometries. *Journal of Computational Physics* **171**, 132–150.

REFERENCES

- KIM, J. & MOIN, P. 1985 Application of a fractional-step method to incompressible navier-stokes equations. *Journal of Computational Physics* **59**, 308–323.
- LE, H. & MOIN, P. 1991 An improvement of fractional step methods for the incompressible Navier–Stokes equations. *Journal of Computational Physics* **92**, 369–374.
- LORBER, P. F. & CARTA, F. O. 1987 Unsteady stall penetration experiments at high reynolds number. AFOSR TR 87-1202.
- LORBER, P. F. & CARTA, F. O. 1994 Incipient torsional stall flutter aerodynamic experiments on three-dimensional wings. *Journal of Propulsion and Power* **10** (2), 217–224.
- LUND, T. S., WU, X. & SQUIRES, K. D. 1998 Generation of turbulent inflow data for spatially-developing boundary layer simulations. *Journal of Computational Physics* **140** (2), 233–258.
- MAHESH, K., CONSTANTINESCU, G. & MOIN, P. 2004 A numerical method for large-eddy simulation in complex geometries. *Journal of Computational Physics* **197**, 215–240.
- MARTIN, D. & COLELLA, P. 2000 A cell-centered adoptive projection method for the incompressible euler equation. *Journal of Computational Physics* **163**, 217–312.
- MARTIN, D., COLELLA, P. & GRAVES, D. 2008 A cell-centered adaptive projection method for the incompressible navierstokes equations in three dimensions. *Journal of Computational Physics* **227**, 1863–1886.
- MCCORQUODALE, P., COLELLA, P. & JOHANSEN, H. 2001 A cartesian grid embedded boundary method for the heat equation on irregular domains. *Journal of Computational Physics* **173**, 620–635.
- MCCROSKEY, W. J. 1982 Unsteady airfoils. *Annual Review of Fluid Mechanics* **14**, 285–311.
- MCCROSKEY, W. J., CARR, L. W. & MCALISTER, K. W. 1976 Dynamic stall experiments on oscillating airfoils. *AIAA Journal* **14** (1), 57–63.
- MCCROSKEY, W. J., MCALISTER, K. W., CARR, L. W. & PUCCI, S. L. 1982 Experimental study of dynamic stall on advanced airfoil sections. NASA TM-84245.

- MINION, M. 1996 A projection method for locally refined grids. *Journal of Computational Physics* **127**, 158–178.
- MOIN, P., SQUIRES, K., CABOT, W. & LEE, S. 1991 A dynamic subgrid-scale model for compressible turbulence and scalar transport. *Physics of Fluids (A)* **3**, 2746.
- NA, Y. & MOIN, P. 1998 Direct numerical simulation of a separated turbulent boundary layer. *Journal of Fluid Mechanics* **374**, 379–405.
- NAGARAJAN, S., FERZIGER, J. H. & LELE, S. K. 2004 Leading edge effects in bypass transition. TF Report-90. Stanford University, Stanford, California.
- NAGARAJAN, S., HAHN, S. & LELE, S. K. 2006 Prediction of sound generated by a pitching airfoil: A comparison of rans and les. *AIAA Paper 2006-2516*.
- OKAJIMA, A. 1965 Numerical analysis of the flow around an oscillating cylinder. In *Proceedings of the 6th International Conference on Flow-Induced Vibration*, edited by P. W. Bearman, p. 159.
- PEMBER, R., BELL, J., COLELLA, P., CURTCHFIELD, W. & WELCOME, M. 1995 An adaptive cartesian grid method for unsteady compressible flow in irregular regions. *Journal of Computational Physics* **120**, 278–304.
- PENG, Y., SHIAU, Y. & HWANG, R. 2003 Transition in a 2-d lid-driven cavity flow. *Computational Fluids* **32**, 337–352.
- PENG, Y.-F., MITTAL, R., SAU, A. & HWANG, R. 2010 Nested cartesian grid method in incompressible viscous fluid flow. *Journal of Computational Physics* **229**, 7072–7101.
- PESKIN, C. 1972 Flow patterns around heart valves: a numerical method. *Journal of Computational Physics* **10**, 252–271.
- ROBICHAUX, J., BALACHANDAR, S. & VANKA, S. P. 1999 Three-dimensional floquet instability of the wake of square cylinder. *Physics of Fluids* **11**, 560.
- ROMA, A., PESKIN, C. & BERGER, M. 1999 An adaptive version of the immersed boundary method. *Journal of Computational Physics* **153**, 509–534.
- SAHOO, D., SRINIVASAN, R. & BOWERSOX, R. 2009 Examination of the leading edge flow structure of a dynamically pitching NACA 0012 airfoil. *AIAA Paper 2009-788*.

REFERENCES

- SAU, A., SHEU, T., TSAI, S., HWANG, R. & CHIANG, T. 2004 Structural development of vertical flows around a square jet in cross-flow. *Proceedings of the Royal Society London Series A* **460**, 339–3368.
- SHIAU, Y., PENG, Y., HWANG, R. & HU, C. 1999 Multistability and symmetry breaking in the 2-d flow around a square cylinder. *Physical Review E* **60**, 6188–6191.
- SHOEYBI, M., HAM, F., SVARD, M. & MOIN, P. 2007 A stable hybrid implicit/explicit scheme for large-eddy simulation of compressible flows in complex geometries. In *60th Annual Meeting of the Division of Fluid Dynamics*. American Physical Society, Salt Lake City, Utah.
- SHU, C.-W., DON, W.-S., GOTTLIEB, D., SCHILLING, O. & JAMESON, L. 2005 Numerical convergence study of nearly incompressible, inviscid Taylor-Green vortex flow. *Journal of Scientific Computing* **24**, 1–27.
- SIMPSON, R. L. 1989 Turbulent boundary layer separation. *Annual Review of Fluid Mechanics* **21**, 205–234.
- SKOTE, M. & HENNINGSON, D. S. 2002 Direct numerical simulation of a separated turbulent boundary layer. *Journal of Fluid Mechanics* **471**, 107–136.
- SMITH, F. T. 1988 Finite-time break-up can occur in any unsteady interacting boundary layer. *Mathematika* **35** (70), 256–273.
- SOHANKAR, A., NORBERG, C. & DAVIDSON, L. 1997 Numerical simulation of unsteady flow around a rectangular two-dimensional cylinder at incidence. *Journal of Wind Engineering & Industrial Aerodynamics* **69**, 189.
- SPALART, P., JOU, W. H., STRELETS, M. & ALLMARAS, S. R. 1997 Comments on the feasibility of LES for wings and on a hybrid RANS/LES approach. In *1st AFOSR International Conference on DNS/LES*, pp. 137–147.
- SPENTZOS, A., BARAKOS, G., BADCOCK, K., RICHARDS, B., WERNERT, P., SCHRECK, S. & RAFFEL, M. 2005 Investigation of three-dimensional dynamic stall using computational fluid dynamics. *AIAA Journal* **43** (5), 1023–1033.
- STRAND, B. 1994 Summation by parts for finite difference approximations for d/dx . *Journal of Computational Physics* **110**, 47–67.

- TAYLOR, G. I. 1938 The spectrum of turbulence. *Proceedings of the Royal Society of London. Series A* **164**, 476–490.
- TSENG, Y. & FERZIGER, J. 2003 A ghost-cell immersed boundary method for flow in complex geometry. *Journal of Computational Physics* **192**, 593–623.
- VISBAL, M. R. 1988 Effect of compressibility on dynamic stall of a pitching airfoil. *AIAA Paper 1988-0132*.
- VISBAL, M. R. 1990 Dynamic stall of a constant rate pitching airfoil. *Journal of Aircraft* **27** (5), 400–407.
- VISBAL, M. R. 1991 On the formation and control of the dynamic stall vortex on a pitching airfoil. *AIAA Paper 91-0006*.
- WALKER, J. M., HELIN, H. E. & STRICKLAND, J. H. 1985 An experimental investigation of an airfoil undergoing large-amplitude pitching motions. *AIAA Journal* **23** (8), 1141–1142.
- YE, T., MITTAL, R., UDAYKUMAR, H. & SHYY, W. 1999 An accurate cartesian grid method for viscous incompressible flows with complex immersed boundaries. *Journal of Computational Physics* **156**, 209–240.
- YOU, D., HAM, F. & MOIN, P. 2008a Discrete conservation principles in large-eddy simulation with application to separation control over an airfoil. *Physics of Fluids* **20**, 101515.
- YOU, D., HAM, F. & MOIN, P. 2008b Discrete conservation principles in large-eddy simulation with application to separation control over an airfoil. *Physics of Fluids* **20**, 101515.
- YOU, D. & MOIN, P. 2007 A dynamic global-coefficient subgrid-scale eddy-viscosity model for large-eddy simulation in complex geometries. *Physics of Fluids* **19** (6), 065110.
- YOU, D., WANG, M. & MITTAL, R. 2007 A methodology for high performance computation of fully inhomogeneous turbulent flows. *International Journal for Numerical Methods in Fluids* **53**, 947–968.
- ZWART, P. 2000 The integrated space-time finite volume method. PhD thesis, University of Waterloo.